Quantum Chromodynamics with Eight and Twelve Degenerate Quark Flavors on the Lattice

Xiao-Yong Jin

Submitted in partial fulfillment of the
requirements for the degree
of Doctor of Philosophy
in the Graduate School of Arts and Sciences

COLUMBIA UNIVERSITY

2011

ABSTRACT

Quantum Chromodynamics with Eight and Twelve Degenerate Quark Flavors on the Lattice

Xiao-Yong Jin

This thesis is concerned with the behavior of non-abelian gauge theories with many flavors of fermions. In perturbation theory, an infrared fixed point is predicted to exist, and theories become conformal in the low energy limit, in non-abelian gauge theories with the number of fermions just below the threshold of losing asymptotic freedom. With the number of fermion flavors even smaller than the number required for conformal behavior, the coupling constant is expected to run slowly or "walk". However, the exact number of fermion flavors that is required for the conformal behavior is unknown. This thesis probes for non-perturbative evidence for such behavior by simulating $\mathrm{SU}(3)$ gauge theories on the lattice with eight and twelve degenerate fermions in the fundamental representation.

The naive staggered fermion action with the DBW2 gauge action is used in the simulations. The exact RHMC algorithm with the Omelyan integrator is used for simulating all eight-flavor gauge configurations and twelve-flavor gauge configurations with large masses, $m_q \geq 0.01$. For the other twelve-flavor simulations with smaller masses, $m_q < 0.01$, the exact HMC algorithm with multiple mass preconditioning and the force gradient integrator is used. Comparisons are also done with previous simulations, which

used the Wilson plaquette gauge action and the inexact R algorithm.

Both zero temperature ($N_t = 32$) and finite temperature physics are studied in this thesis. For system with eight flavors, the focus of the zero temperature simulations is on three values of input couplings $\beta = 0.54$, 0.56 and 0.58, with two or three quark masses for each coupling value. The zero-temperature, lattice artifact bulk transition found with the Wilson plaquette action in other work becomes a rapid cross-over with the DBW2 gauge action. At finite temperatures, a first order phase transition is observed at the strongest coupling, $\beta = 0.54$. For systems with twelve flavors, a large amount of simulation is done at values of input couplings from $\beta = 0.45$ to 0.50. A zero-temperature bulk transition is found with quark masses $m_q = 0.006$ and 0.008, and it ends in a second order critical point at masses slightly larger than 0.008. The system shows a mass-dependent rapid cross-over with quark masses $m_q \geq 0.01$ around the lattice couplings from $\beta = 0.46$ to $\beta = 0.48$. A finite temperature study at $\beta = 0.49$ shows a drastic change of behavior in the screening masses and other observables, which suggests the existence of a finite temperature transition.

All the evidences gathered in this thesis support the argument that theories of both eight and twelve flavors of fermion in the fundamental representation of SU(3) gauge group are consistent with the behavior one would expected from a theory with spontaneously broken chiral symmetry. The strongest supporting evidence is the linearity of $m_\pi^2 \propto m_q$ at zero temperatures and the existence of a chiral symmetry restoring transition at finite temperatures. We note that other lattice simulations, also exploring the hadronic observables, arrive at a similar conclusion, while simulations of the running of the coupling have claimed that the 12 flavor theory is conformal.

Table of Contents

List of Figures

List of Tables

Acknowledgments

First, I would like to thank my advisor, Bob Mawhinney, for his inspiration and guidance throughout my Ph.D. years. He has given me much freedom in research, yet enough control to help me stay on the right path. I have learnt a lot from him, which is definitely a life time benefit.

I also thank Norman Christ for all the insightful discussions we had. It was him who brought me into this fascinating field, when he told me how exciting QCDSP had been.

In addition, I want to thank all the people in the RBC-UKQCD collaboration, both former and current members. Although this thesis topic is not a major research direction of the collaboration, I have received much support from this impressive group of people. I mention here a few specifically, but there are many more, to whom I feel grateful. Talking with Amarjit Soni has always been interesting and illuminating. Chulwoo Jung has always been helpful with the CPS code. Some code I have been using were directly from Michael Cheng, Min Li and Hantao Yin.

Finally, I owe thanks to my family. My parents made me who I am, and they have always been very supportive. I wish I could have spent more time with my parents. I want to express my love and appreciation for my wife Qi Guo, who has always been standing by my side, encouraging me, bringing all the joys to me.

To 婷儿

Part I

Introduction

Chapter 1

QCD and Running Couplings

1.1 Quantum Chromodynamics

Quantum Chromodynamics (QCD) is a theory describing the strong interactions between quarks and gluons, and the formation of hadrons is a non-perturbative result of this strong interaction. It is a Yang-Mills theory [4] with fermions in the fundamental representation of the SU(3) gauge group.

Quarks Quarks live in the fundamental representation **3** of the SU(3) gauge group, so they have color charges and interact with the gluons. The left-handed ones are also doublets in the electroweak gauge symmetry in the standard model and participate in the electroweak interaction, which will not be discussed in this thesis. There are six different types of quarks currently discovered in nature and described by the standard model. They are named as "down" d, "up" u, "strange" s, "charm" c, "bottom" b and "top" t. Their masses ranges from several MeV to several hundred GeV. Given that the exact mechanism of electroweak symmetry breaking is

unknown, quark masses are currently part of the input parameters of the standard model.

Gluon Gluons are the quanta of the gauge field and live in the adjoint representation **8** of the SU(3) gauge group, so they have color charges and interact with themselves in addition to interacting with the quarks. Gluons are singlets in the electroweak gauge group SU(2)×U(1), and thus are not involved in the electroweak interaction.

QCD is an important part of the current standard model of particle theory. The standard model describes all the particles known to date with astonishingly high precision. The fundamental particles in the standard model live in a gauge group of SU(3)×SU(2)× U(1). The SU(2) × U(1) is the electroweak gauge symmetry, which is broken down to U(1) Quantum Electrodynamics (QED) with one exactly massless photon field, leaving 3 massive fields $W^{\pm}$ and Z for the force carriers of the weak interactions. The SU(3) part of the full standard model gauge group is the QCD gauge group.

The Lagrangian for QCD can be written as

$$\begin{aligned} \mathcal{L}_{\mathrm{QCD}} &= \bar{\psi}_{fi\alpha}\left(i\gamma^{\mu}_{ij}D_{\mu\alpha\beta}\delta_{fg} - m_{fg}\delta_{ij}\delta_{\alpha\beta}\right)\psi_{gj\beta} - \frac{1}{4}G_{a\mu\nu}G_{a}^{\mu\nu}\,, \\ G^{a}_{\mu\nu} &= \partial_{\mu}A^{a}_{\nu} - \partial_{\nu}A^{a}_{\mu} + gf^{abc}A^{b}_{\mu}A^{c}_{\nu}\,, \\ D_{\mu\alpha\beta} &= \partial_{\mu}\delta_{\alpha\beta} - igA^{a}_{\mu}t^{a}_{\alpha\beta}\,. \end{aligned} \tag{1.1}$$

In the QCD Lagrangian, G, the gauge field, and ψ, the quark field, are functions of space-time points. They describe the behavior of quarks and gluons. Indices are shown explicitly in this equation, but will be omitted later for clarity. Here, the summations over repeated indices are understood. Flavor indices f, g run through 1 to 6 representing each flavor. Color indices α, β run through 1 to 3 for the fundamental representation

of SU(3), while a, b and c run through 1 to 8 for the adjoint representation. The rest of the indices are Dirac indices i, j, and the space-time indices μ, ν. The mass matrix m is usually diagonalized to make each quark field its own mass eigen-state. The mass term explicitly breaks the flavor symmetry, which is not natural in the standard model. It is hypothesized to originate from the Yukawa couplings with the Higgs field, which is related to the electroweak symmetry breaking from the full gauge group of the standard model, $\mathrm{SU}(2) \times \mathrm{U}(1)$, to U(1) QED.

QCD is the basic building block of the everyday world. In spite of the fact that the quark masses (or all the masses in the standard model) are given by the hypothetical Higgs particle via inducing electroweak symmetry breaking, 99% of the mass of objects human beings see and interact with everyday are from the QCD interaction. A proton or neutron is roughly a hundred times more massive than its constituents—three light quarks (mainly u and d)—were they to be separated.

1.1.1 Color Confinement, String Tension

In nature, in the low energy world, only color singlet particles exist freely. This is an amazing property of QCD, color confinement—no colored particles (such as free quarks) can be observed in the long distance and low energy world. Most of the daily life on the earth relies on electromagnetism[1], the low energy classical theory coming from QED, and most objects can be electrically charged, because of free electrons. However, QCD is very different. Unlike the U(1) gauge theory, QED, where the interaction between two electrons weakens with inverse square distance, when two quarks are separated, the force between them remains nearly constant, and the potential between the quarks rises

[1]There is of course gravity, which will not be discussed here.

linearly with the separation, until sufficient energy is put into the system to pair-create quark/anti-quark pairs.

Intuitively, instead of non-self-interacting photons in QED, the gluons in QCD interact with each other and form strong bonds between these two separated quarks. This bond is usually called the QCD *string* between two quarks. Because the potential between the two separated quarks rises quickly, with the addition of quantum fluctuation, this potential can easily produce a quark and anti-quark pair. Thus the string breaks, two mesons have been produced, and no free quarks survive at long distances.

One of the most popular potential models for the force between the quarks is the Cornell potential,

$$V(r) = -\frac{\alpha}{r} + \sigma r. \tag{1.2}$$

It is a combination of a QED like potential that is proportional to the inverse of the distance and a linear rising piece of the potential that is unique to QCD. In the equation (1.2), σ is a measure of the force in the string, and is usually called the QCD *string tension*.

1.1.2 Chiral Symmetry and its Breaking

In a massless theory with N_f quark flavors, the Lagrangian $\bar{\psi} I \not{\partial} \psi$ has a symmetry of $\mathrm{U}(N_f)_L \times \mathrm{U}(N_f)_R \sim \mathrm{SU}(N_f)_L \times \mathrm{SU}(N_f)_R \times \mathrm{U}(1)_V \times \mathrm{U}(1)_A$. To see this, define left and right handed projectors, which act on the Dirac indices,

$$P_L = \frac{1}{2}(1 - \gamma_5)\,, \quad P_R = \frac{1}{2}(1 + \gamma_5)\,, \tag{1.3}$$

and the corresponding fields

$$\psi_L = P_L\psi\,, \quad \psi_R = P_R\psi\,. \tag{1.4}$$

Because γ_5 is hermitian and anticommutes with γ_μ,

$$\bar{\psi}\not{\partial}\psi = \bar{\psi}_L\not{\partial}\psi_L + \bar{\psi}_R\not{\partial}\psi_R\,. \tag{1.5}$$

The left and right handed spinors ψ_L, ψ_R decouple and transform separately, which leads to a $\mathrm{SU}(N_f)_L \times \mathrm{SU}(N_f)_R$ global symmetry with N_f flavors of quarks. Classically there also would be $\mathrm{U}(1)_V \times \mathrm{U}(1)_A$ symmetry corresponding to the vector and axial vector current. However, the axial current $\mathrm{U}(1)_A$ is not conserved by the quantum fluctuations due to the Adler–Bell–Jackiw anomaly[5, 6].

The *chiral symmetry*, $\mathrm{SU}(N_f)_L \times \mathrm{SU}(N_f)_R$, is spontaneously broken down to $\mathrm{SU}(N_f)$ by the QCD vacuum with the formation of a quark condensate,

$$\langle\bar{\psi}\psi\rangle = \langle\bar{\psi}_L\psi_R + \bar{\psi}_R\psi_L\rangle \neq 0 \tag{1.6}$$

Thus, this quark condensate in the QCD vacuum is usually called *chiral condensate*.

In this process of spontaneous symmetry breaking, $N_f^2 - 1$ (one for each of the generators of $\mathrm{SU}(N_f)$) bosons become massless according to the Goldstone theorem, and are named Goldstone bosons. In the case of QCD, the broken axial currents j_μ^{5a} have direct couplings to the Goldstone bosons $\pi^a(x)$,

$$\langle 0 \left| j_\mu^{5a}(x) \right| \pi^b(p)\rangle = ip_\mu f_\pi \delta^{ab} e^{-ipx}\,, \tag{1.7}$$

where f_π is the pion decay constant usually measured in pion leptonic decays, and the convention here uses $f_\pi \simeq 93\,\text{MeV}$. Taking the divergence and choosing $x = 0$ gives

$$\langle 0 \left| \partial^\mu j_\mu^{5a}(0) \right| \pi^b(p) \rangle = \delta^{ab} f_\pi m_\pi^2 \,. \tag{1.8}$$

If chiral symmetry is not explicitly broken by the quark mass term, making the axial-vector current conserved, $\partial^\mu j_\mu^{5a} = 0$, the above equation leads to $m_\pi^2 = 0$, which is predicted by the Goldstone theorem. However, if the quark mass term exists and the symmetry is explicitly broken, equation (1.8) can be rewritten to be

$$\langle 0 \left| \partial^\mu j_\mu^{5a}(0) \right| \pi^b(p) \rangle = f_\pi m_\pi^2 \langle 0 \left| \varphi^a(0) \right| \pi^b(p) \rangle \,, \tag{1.9}$$

where φ^a is the pion field operator. This is known as the *partially conserved axial-vector current* (PCAC) hypothesis, and is expected to hold at operator level

$$\partial^\mu j_\mu^{5a} = f_\pi m_\pi^2 \varphi^a \,. \tag{1.10}$$

In the real world, quark masses are indeed non-zero. The additional mass terms in the QCD Lagrangian explicitly break the exact chiral symmetry. Considering the lightest two quarks, u and d, whose masses are a few MeV, the three copies of would-be-Goldstone bosons are the pions, $\pi^\pm$ and π^0, which are much lighter than other meson states. The pions are almost Goldstone bosons, because the masses of the u and d quarks are small. With some current algebra and the PCAC relation, one finds the Gell-Mann–Oakes–Renner (GMOR) relation[7],

$$f_\pi^2 m_\pi^2 = (m_u + m_d) \langle 0 \left| \frac{\bar{u}u + \bar{d}d}{2} \right| 0 \rangle \,. \tag{1.11}$$

The fact that the QCD vacuum forms a condensate that breaks chiral symmetry and the physical states are pions instead of free quarks, suggests that QCD at the lowest energies can be described with the Goldstone bosons alone. At low energies, the physics (or the Greens functions) are dominated by the poles due to the exchange of the Goldstone bosons, as they are the lightest states in the theory. One uses the SU(2) triplet pion fields (or SU(3) meson octet) to construct the low energy effective theory for the underlying theory with d and u quarks (or d, u and s quarks) [8, 9, 10]. This low energy effective theory is encapsulated in the chiral Lagrangian, which can be systematically expanded in chiral perturbation theory. Through matching the low energy constant and the full QCD theory, one readily finds the GMOR relation as the leading order expansion of the chiral perturbation theory. The next-to-leading-order continuum SU(N_f) chiral perturbation expansion can be found [11] as

$$\begin{aligned} M_\pi &= M\left(1+\frac{M^2}{N_f F^2 16\pi^2}\log\frac{M}{\Lambda_1}+\mathcal{O}(M^4)\right), \\ F_\pi &= F\left(1-\frac{N_f M^2}{F^2 16\pi^2}\log\frac{M}{\Lambda_2}+\mathcal{O}(M^4)\right), \\ \langle\bar\psi\psi\rangle &= -F^2 B\left(1-\frac{N_f^2-1}{N_f}\frac{M^2}{F^2 8\pi^2}\left(\log\frac{M}{\Lambda_3}+\frac{1}{4}\right)+\mathcal{O}(M^4)\right), \end{aligned} \tag{1.12}$$

where $M = (2m_q B)^{1/2}$ with the degenerate quark mass being m_q and B a parameter with the dimension of mass, F corresponds to the chiral limit value of f_π defined in equation (1.7), and $\langle\bar\psi\psi\rangle$ is the chiral condensate per flavor, and is usually denoted as $\langle\bar uu\rangle$ or $\frac{1}{2}\langle\bar uu+\bar dd\rangle$ in the literature. While there is explicit dependence on N_f, the number of light quark flavors, there is also implicit dependence on N_f in the parameters M, F and B. Here Λ is the scale where chiral perturbation theory is renormalized and for physical QCD, this is usually taken as $\sim 1\,\mathrm{GeV}$.

1.1.3 Asymptotic Freedom

Another astounding feature of QCD happens at short distances and high energy. When the momentum exchange in a scattering process becomes higher, the renormalized coupling becomes much weaker. In the limit of very high energy and really short distances, the quarks are essentially free and without any interactions. Such behavior is called asymptotic freedom [12, 13, 14, 15]. The Nobel Prize in Physics 2004 was awarded jointly to David J. Gross, H. David Politzer and Frank Wilczek "for the discovery of asymptotic freedom in the theory of the strong interaction". It can be proven that all non-abelian gauge theories without fermions are asymptotically free in the high energy and short distance limit. The renormalization group beta function of a such theory is negative in the high energy limit. As a result, the coupling constant becomes weaker and flows towards the origin as the energy scale increases. In the case of an $\mathrm{SU}(3)$ gauge theory with fundamental fermions, such as QCD, the two loop renormalization-group beta function can be calculated explicitly using perturbation theory [16],

$$\begin{aligned} \beta(g) = \mu\frac{dg}{d\mu} &= -\beta_1 g^3 - \beta_2 g^5 - \mathcal{O}(g^7)\,, \\ \beta_1 &= \frac{1}{16\pi^2}\left(\frac{11}{3}N_c - \frac{2}{3}N_f\right)\,, \\ \beta_2 &= \frac{1}{(16\pi)^2}\left(\frac{34}{3}N_c^2 - \frac{10}{3}N_cN_f - \frac{(N_c^2-1)N_f}{N_c}\right)\,, \end{aligned} \tag{1.13}$$

where μ is the momentum scale, and the subscript of β indicates the number of loops for the calculation. It can be proven that β_1 and β_2 here are universal and do not depend on the particular renormalization scheme. As shown in equation (1.13), when $N_f < 11N_c/2 = 16.5$, the beta function is negative near the origin. Therefore, from the definition of the beta function, g decreases as μ increases.

1.2 Non-trivial Fixed Point and Conformal Behavior

Upon closer inspection of the perturbative renormalization-group beta function, (1.13), one can see that β_2 changes sign even when N_f is smaller than 16. Thus, one might expect that, at a certain $N_f < 16.5$, the beta function starts out negative when g is small and develops a non-trivial zero point when g becomes large. In fact, it is proven perturbatively [17] that there are non-trivial fixed points of the beta function other than the Gaussian fixed point at the origin, if N_f is in the vicinity of 16.5. The existence of an infrared fixed point makes the theory conformal at long distances, while asymptotic freedom is not lost. The chiral symmetry is generally believed not to be spontaneously broken, if the theory is infrared conformal.

Chapter 2

Technicolor and Infrared Fixed Points

The common conjecture for the source of the electroweak symmetry breaking ($SU(2) \times U(1) \rightarrow U(1)$) in the standard model is by one or several scalar particles called *Higgs Bosons* (see Ref. [18] for a history lesson). However, several higgsless theories exists. *Technicolor* [19, 20, 21] (TC) is one of those theories of dynamical electroweak symmetry breaking without a fundamental Higgs particle. This chapter tries to build a strong motivation for this thesis work by introducing the basic concepts of technicolor. It is not, however, meant to be a complete introduction. Please refer to Refs. [22, 23] for recent reviews on technicolor.

2.1 Technicolor

Technicolor starts from the idea that it is possible to break electroweak symmetry in a way similar to chiral symmetry breaking in QCD. Consider a toy model with $SU(3)_C \times$

$\mathrm{SU}(2)_L \times U(1)_Y$ and only one generation of fermions,

$$q_L = \begin{pmatrix} u \\ d \end{pmatrix}_L \qquad l_L = \begin{pmatrix} \nu \\ e \end{pmatrix}_L . \tag{2.1}$$

The Lagrangian can be written as

$$\mathcal{L} = -\frac{1}{4} G^{\alpha\mu\nu} G^{\alpha}_{\mu\nu} - \frac{1}{4} A^{i\mu\nu} A^{i}_{\mu\nu} - \frac{1}{4} B^{\mu\nu} B_{\mu\nu} + i(\bar{q} \not{D} q + \bar{l} \not{D} l) . \tag{2.2}$$

There are no explicit mass terms for any of the fields.

Without the electroweak interaction, the chiral symmetry is spontaneously broken for this toy model similar to the case of QCD, and there are three exactly massless Goldstone bosons, $\pi^{\pm}$ and π^0. The effective scalar and pseudoscalar fields σ and π corresponding to the quark bilinear can be defined as

$$\sigma \sim \bar{q} q \quad \text{and} \quad \pi \sim \bar{q} \gamma_5 \tau q , \tag{2.3}$$

where τ is the $\mathrm{SU}(2)$ generator. As the symmetry is spontaneously broken, one chooses the σ field to acquire the *vacuum expectation value* (VEV), which is equivalent to f_π,

$$\langle \sigma \rangle = v \simeq f_\pi . \tag{2.4}$$

With the electroweak interaction, the quark bilinears would transform similarly to a

Higgs doublet in a standard Higgs model,

$$\varphi_{\text{eff}} = \begin{pmatrix} \pi_1 + i\pi_2 \\ \sigma + i\pi_3 \end{pmatrix} . \tag{2.5}$$

Thus, the VEV breaks the $\mathrm{SU}(2)_L \times \mathrm{U}(1)$ symmetry down to the electromagnetic $\mathrm{U}(1)$. Here, the exact massless π fields are eaten by the three gauge bosons. Consider the propagator of the gauge boson,

$$\frac{g_{\mu\nu} - k_\mu k_\nu / k^2}{k^2} . \tag{2.6}$$

Summing over all quark loop insertions to the propagator, one finds a multiplicative renormalization coefficient of the above propagator,

$$\sum_l \left(\frac{g^2}{4} \frac{f_\pi^2}{k^2} \right)^l = \frac{1}{1 - \frac{g^2}{4} \frac{f_\pi^2}{k^2}} , \tag{2.7}$$

where the pion propagator is used in place of the quark loops. Then the propagator (2.6) is modified to become

$$\frac{g_{\mu\nu} - k_\mu k_\nu / k^2}{k^2 - \frac{g^2}{4} f_\pi^2} . \tag{2.8}$$

It has a pole at

$$k^2 = \frac{g^2}{4} f_\pi^2 . \tag{2.9}$$

One identifies the mass of the $W^\pm$ bosons to be

$$M_W = \frac{1}{2} g f_\pi . \tag{2.10}$$

Similarly, the mass of the Z boson can be obtained by diagonalizing the mass matrix,

which leaves the photon massless in the process.

To obtain the physical mass of 80 GeV for the W boson, f_π in this toy model needs to be in the order of 250 GeV. Compared to the QCD $f_\pi \simeq 93\,\text{MeV}$, this is a much larger scale.

The idea of technicolor is the existence of a non-abelian gauge (G_{TC}) field that produces a condensate at an energy three orders of magnitude larger than QCD, but very similar to QCD in other ways. The familiar quarks and leptons are TC singlets, but the technicolor quarks (or techniquarks) also interact with each other through standard model interactions. Therefore, one expects a rich spectrum of particles at the TeV scale.

2.2 Extended Technicolor

In Higgs models, quarks and leptons obtain their masses through the Yukawa couplings of the elementary Higgs scalar to fermions. In the case of TC discussed in the previous section, fermions remain massless. To give fermion masses, one can employ an *extended technicolor* (ETC) gauge group (G_{ETC}) [24, 25], which couples to both the technifermions and ordinary fermions. Both the technifermions and the ordinary fermions are in a single irreducible representation of G_{ETC}.

One expects ETC break down to TC at some energy scale μ higher than TC scale, and the vector gauge boson being in ETC but not TC acquires mass $M_{\text{ETC}} \simeq g_{\text{ETC}}\mu$, which also couples to the currents of the form $\bar{f}_{\text{ETC}}\gamma_\mu f$. Thus the effective four-fermion interactions have the form

$$\frac{1}{2}\left(\frac{g_{\text{ETC}}}{M_{\text{ETC}}}\right)^2 (\bar{f}^L_{\text{ETC}}\gamma_\mu f^L)(\bar{f}^R\gamma_\mu f^R_{\text{ETC}})\,, \tag{2.11}$$

which, after a Fierz transformation, leads to

$$-\frac{1}{2\mu^2}\left((\bar{f}_{\mathrm{ETC}}f_{\mathrm{ETC}})(\bar{f}f)-(\bar{f}_{\mathrm{ETC}}\gamma_5 f_{\mathrm{ETC}})(\bar{f}\gamma_5 f)+\cdots\right). \tag{2.12}$$

The nonzero condensation of technifermions $\langle\bar{f}_{\mathrm{ETC}}f_{\mathrm{ETC}}\rangle_{\mathrm{ETC}}$ evaluated at the ETC scale ($\sim M_{\mathrm{ETC}}$) then produces a mass for the ordinary fermions

$$m_f=\frac{1}{2\mu^2}\langle\bar{f}_{\mathrm{ETC}}f_{\mathrm{ETC}}\rangle_{\mathrm{ETC}}\,. \tag{2.13}$$

In order to generate all the standard model fermion masses, there needs to be several sequential break-downs of the gauge symmetry from G_{ETC} to G_{TC}. A simple toy model would be a sequential break-down pattern, $\mathrm{SU}(N_{\mathrm{TC}}+3)\to\mathrm{SU}(N_{\mathrm{TC}}+2)\to\mathrm{SU}(N_{\mathrm{TC}}+1)\to\mathrm{SU}(N_{\mathrm{TC}})$. In this process, three families of fermions can acquire masses as in equation (2.13), where the energy scale μ is replaced by the energy scale where the break down happens, and the condensate is also renormalized at the corresponding energy scale. Note that one needs one technifermion for each standard model fermion in this model.

2.3 The need for walking or conformal behavior

There are many problems related to the technicolor model discussed so far. One of them is related to the constraints from *flavor-changing neutral currents* (FCNC). The ETC gauge bosons couple to the currents $\bar{f}_{\mathrm{ETC}}\gamma_\mu f$ and $\bar{f}'\gamma_\mu f_{\mathrm{ETC}}$ and must also have a contribution to $\bar{f}'\gamma_\mu f$. After the ordinary quark mass matrix is diagonalized, the FCNC currents $\bar{f}'\gamma_\mu f$ will couple to an ETC gauge boson. This gauge boson will have a similar mass as the ETC

gauge boson, which gives mass to the ordinary fermion. This unavoidably leads to some FCNC interactions. No mechanism similar to GIM has been found yet to alleviate these unwanted interactions.

The most stringent constraint probably comes from $|\Delta S| = 2$ interactions that give the mass difference between K_L and K_S. The generic form of the interaction is

$$\mathcal{L}_{|\Delta S|=2} = \frac{g_{\mathrm{ETC}}^2 \theta_{sd}^2}{M_{\mathrm{ETC}}^2} \bar{s}\Gamma^\mu d \bar{s}\Gamma'_\mu d + \text{h.c.}\,, \tag{2.14}$$

where θ_{sd} is the mixing angle, which would be comparable to the Cabibbo angle. The matrices Γ^μ and Γ'_μ are of left or right chirality. The contribution to the mass difference of K_L and K_S can be estimated as in the standard model,

$$\Delta M_K = 2\mathrm{Re}\left(\langle \bar{K} \left| \mathcal{L}_{|\Delta S|=2} \right| K \rangle\right)\,. \tag{2.15}$$

With the *vacuum saturation* approximation, this leads to

$$\begin{aligned} 2M_K^0 (\Delta M_K)_{\mathrm{ETC}} &= \frac{g_{\mathrm{ETC}}^2 \theta_{sd}^2}{M_{\mathrm{ETC}}^2} \langle \bar{K}^0 \left| \bar{s}\Gamma^\mu d \bar{s}\Gamma'_\mu d \right| K^0 \rangle + \text{c.c.} \\ &\simeq \frac{g_{\mathrm{ETC}}^2 \mathrm{Re}(\theta_{sd}^2)}{2M_{\mathrm{ETC}}^2} f_K^2 M_K^2\,, \end{aligned} \tag{2.16}$$

where $\Gamma_\mu = \gamma_\mu(1-\gamma_5)/2$ and f_K enters similar to equation (1.7), and $2M_K^0$ arises from the normalization of the state. With the experimental values of $\Delta M_K = 3.5 \times 10^{-12}$ MeV, one arrives at the limit

$$\frac{M_{\mathrm{ETC}}}{g_{\mathrm{ETC}} \sqrt{\mathrm{Re}(\theta_{sd}^2)}} > 600\,\mathrm{TeV}\,, \tag{2.17}$$

or roughly

$$\mu > |\theta_{sd}|\, 600\,\mathrm{TeV}\,. \tag{2.18}$$

Now the problem arises when this constraint is forced upon the generated masses for standard model fermions (2.13),

$$m_f < \frac{\langle \bar{f}_{\mathrm{ETC}} f_{\mathrm{ETC}} \rangle_{\mathrm{ETC}}}{2\theta_{sd}^2 (600\,\mathrm{TeV})^2} \,. \tag{2.19}$$

To see it, consider the renormalization of the chiral condensate

$$\langle \bar{f}f \rangle_{\mathrm{ETC}} = \langle \bar{f}f \rangle_{\mathrm{TC}} \exp\left(\int_{\mu_{\mathrm{TC}}}^{M_{\mathrm{ETC}}} \frac{d\mu}{\mu} \gamma_m(\mu) \right) . \tag{2.20}$$

Here, the anomalous dimension of the scalar density $\gamma_m(\mu)$ differs from the usual mass anomalous dimension by an overall sign,

$$\mu \frac{d}{d\mu} m(\mu) = -\gamma_m(\mu) m(\mu) \,. \tag{2.21}$$

It can be computed in perturbation theory, and takes the usual form of

$$\gamma_m(\mu) = \frac{3C_2(R)}{2\pi} \alpha_{\mathrm{TC}}(\mu) + \mathcal{O}(\alpha_{\mathrm{TC}}^2) \,, \tag{2.22}$$

where $C_2(R)$ is the quadratic Casimir of the technifermion gauge group representation R. If one assumes that technicolor is like QCD with a small anomalous dimension $\gamma_m(\mu)$ for scales $\mu_{\mathrm{TC}} < \mu < M_{\mathrm{ETC}}$, the chiral condensate barely changes from the TC scale to ETC scale, and

$$\langle \bar{f}f \rangle_{\mathrm{ETC}} = \langle \bar{f}f \rangle_{\mathrm{TC}} = 4\pi f_\pi^3 \,, \tag{2.23}$$

where the QCD analog of f_π for TC takes the value of around 250 GeV as discussed in section 2.1.

Assuming θ_{sd} is similar to the Cabibbo angle and takes the value $0.1 < \theta_{sd} < 1$, it is very difficult to generate the *s* quark mass, let alone other larger standard model fermion masses.

To solve this dilemma, one can break the QCD resemblance of equation (2.23). It is possible as discussed in section 1.2. A schematic drawing of a possible theory is shown in figure 2.1. If the theory develops an infrared fixed point and becomes conformal with $N_f > N_f^{\mathrm{C}}$ flavors of fermions, there might exist a region of $N_f < N_f^{\mathrm{C}}$ but close to N_f^{C}, where the renormalization group beta function is small above the chiral symmetry breaking scale μ_{TC}, due to being near the infrared fixed point. In such theories, α_{TC} can remain large for scales $\mu_{\mathrm{TC}} < \mu < M_{\mathrm{ETC}}$. Thus, the technicolor coupling is *walking*, instead of running. This in turn makes the anomalous dimension $\gamma_m(\mu)$ large in the same range of momenta. Then, due to the equation (2.20), the size of the condensate renormalized at the ETC scale, $\langle \bar{f}f \rangle_{\mathrm{ETC}}$, can be greatly enhanced, thus producing larger fermion masses becomes possible [26, 27]. There are also theories of technicolor with infrared conformal behavior that have been proposed [28].

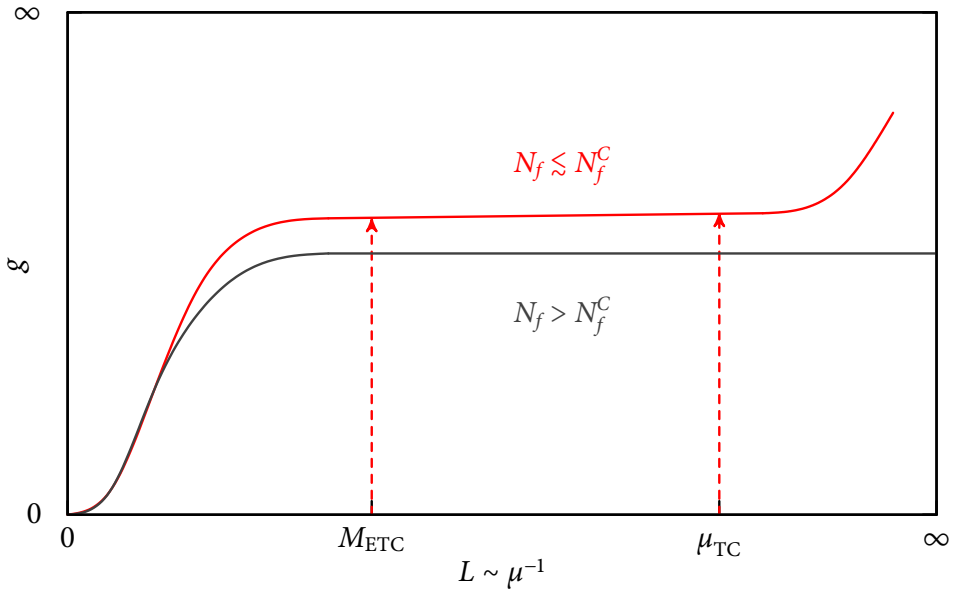

Figure 2.1: Technicolor theory with walking coupling constant. The horizontal axis is the length scale, or inverse energy scale.

One needs to understand how large $\gamma_m(\mu)$ could be in order to make realistic models. Although various estimates exist, no rigorous proof could be given. It would be very interesting to observe such behavior in lattice simulations.

2.4 Purpose of This Thesis Work

It is very difficult to formulate a concrete proposal based on technicolor, mostly due to the fact that the nonperturbative dynamics makes analytical calculations hard if not impossible. To build phenomenologically acceptable models and make predictions, one needs much deeper understanding of the nonperturbative dynamics of the non-abelian gauge theories. Lattice calculations serve as a great method to treat such theories. Nowadays, lattice QCD techniques have been developed and have reached a level of agreement

with the experiments within a few percent.

The purpose of this thesis work is to better understand non-abelian gauge theories with many flavors of fermions. Technicolor phenomenology provides strong motivation to study such strongly coupled theories. While technicolor by itself is very interesting, it is the urge to fully comprehend the low energy behavior of non-abelian gauge theories that have been truly pushing this work forward. This thesis work, thus, is not confined only in the phenomenology of technicolor theories, but mainly concentrates on studying the low energy behavior of the QCD system with eight and twelve degenerate fermions from lattice simulations.

Chapter 3

Lattice Regularization

Regularizing a field theory by using a space-time lattice is excellent for treating QCD non-perturbatively. This chapter serves as a simple introduction to QCD on the lattice, focusing on the staggered fermion action. Various lattice quantities studied in this thesis work are also introduced here. It is not intended to reproduce text books. Please refer to Refs. [29, 30, 31, 32] for a complete introduction, as the author of this thesis finds these easily accessible.

3.1 Introduction to the Lattice

Start from path integral prescription of quantum field theory in the euclidean functional formalism, where time is imaginary $t \to -it$.

$$\begin{aligned} \langle \mathcal{O} \rangle &= Z^{-1} \int [\mathcal{D}\bar{\psi}][\mathcal{D}\psi][\mathcal{D}A]\, \mathcal{O} \exp(-S) \\ Z &= \int [\mathcal{D}\bar{\psi}][\mathcal{D}\psi][\mathcal{D}A] \exp(-S)\,. \end{aligned} \tag{3.1}$$

Here the functional weight[1], $\exp(-S)$, is real instead of complex, $\exp(iS)$, as it is in the Minkowski space-time metric. Therefore, it can be calculated with importance sampling as a Boltzmann weight similar to statistical mechanics.

Recall the fields $\bar{\psi}$, ψ and A are all functions of space-time, and it is natural to put these on a discrete space-time lattice and the formal expression (3.1) can be defined much more rigorously. However, to actually obtain physical results, care must be exercised in the process of discretization.

3.1.1 Fermions on the Lattice

Without a gauge field, it is natural to put fermion fields on a hypercubic lattice, and the discretized free fermion action can be written as

$$\begin{aligned} S_{\text{naive}} &= \sum_x \left(\sum_\mu \bar{\psi}_x \gamma_\mu \frac{1}{2a_\mu} (\psi_{x+a_\mu\hat{\mu}} - \psi_{x-a_\mu\hat{\mu}}) + m\bar{\psi}_x\psi_x \right) \\ &= \sum_x \left(\sum_\mu \frac{1}{2a_\mu} \left(\bar{\psi}_x \gamma_\mu \psi_{x+a_\mu\hat{\mu}} - \bar{\psi}_{x+a_\mu\hat{\mu}} \gamma_\mu \psi_x \right) + m\bar{\psi}_x\psi_x \right) . \end{aligned} \tag{3.2}$$

In the above equation, a_μ is the lattice spacing in the μ direction. The summation over $x_\mu = a_\mu\hat{x}$, $\sum_x = \prod_\mu a_\mu \sum_{\hat{x}}$ includes all the space-time points on the lattice and replaces the integration in the continuum. In the second line, a change of variable makes the kernel of the summation only relates ψ at space-time points x and $x + a_\mu\hat{\mu}$ in order to simplify the notation. The summation over μ is the same as in the continuum. In equation (3.2), flavor, spin and color indices are suppressed. This naive discretization uses central difference to replace the continuum one to minimize the discretization error associated with

[1] An additional gauge fixing term in the Lagrangian is needed for the path integral with $[\mathcal{D}A]$ to make sense. It is, however, not important with the lattice formalism, where the integral over the group space is compact, so it is omitted, here.

it. In this thesis work, isotropic lattices are used, thus the lattice spacing can be simply represented as a. All the variables can be made dimensionless by scaling with the lattice spacing, and the action can be written as

$$S_{\text{naive}} = \sum_{\hat{x}} \left(\sum_{\mu} \frac{1}{2} \left(\hat{\bar{\psi}}_x \gamma_\mu \hat{\psi}_{\hat{x}+\hat{\mu}} - \hat{\bar{\psi}}_{\hat{x}+\hat{\mu}} \gamma_\mu \psi_{\hat{x}} \right) + \hat{m} \hat{\bar{\psi}}_x \hat{\psi}_x \right) . \tag{3.3}$$

In the following discussion and throughout this thesis, the lattice spacing a will be omitted and all the quantities will be in lattice unit, unless explicit dimensionality or the continuum needs to be addressed. We will abuse the notation and remove the hat on the dimensionless variables.

Following the path integral prescription, writing the partition function as

$$\begin{aligned} Z(\eta, \bar{\eta}) &= \int [\mathcal{D}\bar{\psi}][\mathcal{D}\psi] \exp(-\bar{\psi} M \psi + \bar{\psi}\eta + \bar{\eta}\psi) \\ &= \det[M] \exp(\bar{\eta} M^{-1} \eta) , \end{aligned} \tag{3.4}$$

where two fermion sources η and $\bar{\eta}$ are used, and the fermion matrix M is defined as in equation (3.2),

$$M_{xy} = \frac{1}{2} \sum_{\mu} \gamma_\mu (\delta_{x+\mu,y} - \delta_{x,y+\mu}) + m\delta_{x,y} . \tag{3.5}$$

The usual fermion propagator can be obtained by differentiating with respect to the sources

$$\begin{aligned} G(x,y) = \langle \psi_y \bar{\psi}_x \rangle &= Z^{-1} \frac{\partial}{\partial \bar{\eta}_x} \frac{\partial}{\partial \eta_y} Z(\eta, \bar{\eta}) \Big|_{\eta=0, \bar{\eta}=0} \\ &= \left[M^{-1} \right]_{xy} . \end{aligned} \tag{3.6}$$

The inverse of the fermion matrix M can be easily carried out in momentum space

after a discrete Fourier transformation, assuming an infinite space-time lattice,

$$G(k) = \frac{1}{m + i\gamma_\mu \sin k_\mu} = \frac{m - i\gamma_\mu \sin k_\mu}{m^2 + \sin^2 k_\mu} . \tag{3.7}$$

Using non-lattice units, the propagator becomes

$$G(k) = \frac{m - i\gamma_\mu \sin(ak_\mu)/a}{m^2 + \sin^2(ak_\mu)/a^2} , \tag{3.8}$$

which, in the limit $a \to 0$, approaches the usual continuum result asymptotically, and has a pole at $k_4 = i\omega = i\sqrt{\vec{k}^2 + m^2}$.

3.1.1.1 Fermion Doubling Phenomenon

However, this is only one part of the story. Considering the periodicity of the sine function, $\sin^2(ak_\mu) = \sin^2(\pi - ak_\mu)$, the pole of the propagator $G(k)$ in equation (3.8) not only appears near the center of the Brillouin zone, $k = (0, 0, 0, 0)$, but also near the corners of the Brillouin zone, $k_\mu = \pi/a$ for some or all of μ's. Therefore, instead of one pole, there are actually 2 poles for each dimension, and totally $2^4 = 16$ poles for a four dimensional theory. These additional fermion degrees of freedom do not go away with the limit of $a \to 0$. This is called fermion doubling phenomenon on the lattice.

3.1.1.2 Staggered (Kogut–Susskind) Fermion

One clever way of reducing the extra fermion doublers is the staggered fermion [33, 34]. One can first remove the gamma matrices in the naive fermion action by the process of

spin diagonalization. Observing that

$$[\tilde{\Gamma}_x^\dagger \gamma_\mu \tilde{\Gamma}_{x+\mu}]_{ij} = \eta_{\mu x}\delta_{ij}\,, \tag{3.9}$$

$$\tilde{\Gamma}_x \equiv \gamma_1^{x_1}\gamma_2^{x_2}\gamma_3^{x_3}\gamma_4^{x_4}\,, \tag{3.10}$$

where

$$\eta_{\mu x} = (-1)^{\sum_{\nu<\mu} x_\nu}\,. \tag{3.11}$$

After an unitary transformation on ψ and $\bar{\psi}$

$$\psi_x = \tilde{\Gamma}_x \chi_x\,, \quad \bar{\psi}_x = \bar{\chi}_x \tilde{\Gamma}_x^\dagger\,, \tag{3.12}$$

the naive fermion action acquires the form

$$S_{\text{naive}} = \sum_{i=1}^{4}\sum_x \left(\sum_\mu \eta_{\mu x}\frac{1}{2}(\bar{\chi}_x^i \chi_{x+\mu}^i - \bar{\chi}_{x+\mu}^i \chi_x^i) + m\bar{\chi}_x^i \chi_x^i\right)\,. \tag{3.13}$$

The four identical terms produced by the summation of the Dirac spinor index i can be reduced to only one, by simply removing the extra duplication.

$$\begin{aligned} S_{\text{Staggered}} &= \sum_x \left(\sum_\mu \eta_{\mu x}\frac{1}{2}(\bar{\chi}_x \chi_{x+\mu} - \bar{\chi}_{x+\mu}\chi_x) + m\bar{\chi}_x\chi_x\right) \\ &= \bar{\chi}_x M_{xy}\chi_y\,, \\ M_{xy} &= \sum_\mu \eta_{\mu x}\frac{1}{2}(\delta_{x+\mu,y} - \delta_{x,y+\mu}) + m\delta_{x,y}\,, \end{aligned} \tag{3.14}$$

where field χ at each lattice site x has only color indices, which are implicit here. Thus the fermion degrees of freedom can be seen as effectively reduced by a factor of four.

The action without the mass term is invariant under a modified U(1) chiral transfor-

mation,

$$\chi \to \exp(i\tilde{\gamma}_5\alpha)\chi\,, \quad \bar{\chi} \to \bar{\chi}\exp(i\tilde{\gamma}_5\alpha)\,, \tag{3.15}$$

where $\tilde{\gamma}_5$ is $(-1)^{\sum_\mu x_\mu}$. With the mass term, the action satisfies the modified gamma-five hermiticity

$$M^\dagger = \tilde{\gamma}_5 M \tilde{\gamma}_5\,. \tag{3.16}$$

Remember that the $\tilde{\gamma}_5$ acts on each site, to which M connects, this relation can be simply written explicitly as

$$M^\dagger \equiv m + D^\dagger = m - D\,, \tag{3.17}$$

where $D = \sum_\mu \eta_{\mu x}\frac{1}{2}(\delta_{x+\mu,y} - \delta_{x,y+\mu})$ is the Dirac operator without the quark mass term.

To reconstruct a theory of four species of fermion from the action (3.14), define a field variable from a linear combination of the χ fields on a hypercube [35],

$$\Psi_{x,a\alpha} = \frac{1}{8}\sum_\eta \tilde{\Gamma}_{\eta,a\alpha}\chi_{2x+\eta}\,, \tag{3.18}$$

where $2x$ is the origin of the hypercube, and η points to the 16 corners of the hypercube. The indices a and α of the usual gamma matrices are explicitly shown here for a reason which will be clear shortly.

After some careful algebra, the original staggered action (3.14) can be written as

$$\begin{aligned} S_{\text{Staggered}} = b^4 \sum_x \bar{\Psi}_{x,a\alpha}\left(\sum_\mu (\gamma_{\mu,ab}\otimes I_{\alpha\beta})\Delta_\mu + m(I_{ab}\otimes I_{\alpha\beta})\right)\Psi_{x,b\beta} \\ + \frac{1}{2}b^5\sum_{x,\mu}\bar{\Psi}_{x,a\alpha}(\gamma_{5,ab}\otimes\gamma^*_{\mu,\alpha\gamma}\gamma_{5,\gamma\beta})\,\Box_\mu\,\Psi_{x,b\beta}\,, \end{aligned} \tag{3.19}$$

where dimensionful quantities are used explicitly to show the lattice spacing dependency,

and $b = 2a$ is the new lattice spacing after blocking of each hypercube. The block derivatives are defined as usual

$$\Delta_\mu \Psi_x = \frac{1}{2b}\left(\Psi_{x+b\mu} - \Psi_{x-b\mu}\right) , \tag{3.20}$$

$$\Box_\mu \Psi_x = \frac{1}{b^2}\left(\Psi_{x+b\mu} + \Psi_{x-b\mu} - 2\Psi_x\right) . \tag{3.21}$$

The tensor product explicitly separates two sets of 4×4 matrices acting on the two different index spaces of Ψ. Without the second line, the action (3.19) reduces to a theory with four independent Dirac spinors. It is essentially four copies of the naive discretized fermion action (3.2), considering the two $I_{\alpha\beta}$ function as a sum over the second index. As a result, one can identify the first index of Ψ as the usual Dirac spinor index, and the second as flavor index. Thus, the field Ψ represents four flavors of four-component Dirac spinors. However, the second line of the action (3.19) mixes the four flavors on a lattice with finite spacing. This mixing term is irrelevant in the continuum limit, but cannot be neglected in lattice simulations. This term produces flavor splittings (taste splittings in modern language) for the four four-component Dirac spinors. Three of these remaining four spinors were originally doublers (twelve doublers have already been removed by spin diagonalization).

The extra flavor degrees of freedom in the staggered fermion formulation is sometimes called *taste*, when one wants to differentiate between the physical flavor degrees of freedom and the staggered built-in ones. The relabeled field Ψ, which is a linear combination of the field χ in a hypercube, is usually called the spin-taste basis of the staggered fermions.

The remnant U(1) symmetry (3.15) of the original staggered fermion action (3.14) now manifests itself in a new form where $\tilde{\gamma}_5$ is replaced by $\gamma_5 \otimes \gamma_5$. Note that the mixing

term in the second line of the action (3.19) is indeed invariant under this U(1) symmetry.

3.1.1.3 Wilson Fermion

To remove the additional doublers without dealing with mixing tastes, one can add higher dimension terms, which are irrelevant in the continuum limit to the naive action. One possibility suggested by Wilson [36] is adding a second derivative term,

$$\frac{a}{2}\sum_{x,\mu}\bar{\psi}\,\Box_\mu\,\psi\,, \tag{3.22}$$

where the second derivative $\Box_\mu$ is the same as in equation (3.21). Clearly, one can see the relation between this term and the taste mixing term in the staggered action (3.19). This dimension-five term can be transformed into momentum space,

$$\frac{1}{a}\sum_{\mu}(1-\cos k_\mu a)\,, \tag{3.23}$$

which provides a contribution of $2/a$ to the mass of all the doublers that have $k_\mu \simeq \pi/a$, except the one with all $k_\mu \simeq 0$.

However, the simplicity comes with the cost that this term is no longer invariant under chiral symmetry.

3.1.1.4 Domain Wall and Overlap Fermion

An excellent way to cure the explicitly broken chiral symmetry of Wilson fermions is a lattice discretization called Domain Wall fermions [37]. The common practice [38] developed later is to add an auxiliary fifth dimension while keeping the gauge links in four dimensions, and separating the left handed and right handed fermions to two domain

walls at the end of the fifth dimension. As a result, the chiral symmetry breaking term in the middle of the fifth dimension can be exponentially suppressed with an exponent proportional to the length of the fifth dimension, usually named L_s.

The action of domain wall fermions is very similar to Wilson fermion and it is purely local and only connects sites with their nearest neighbors. It has the advantage that one can choose to control the explicit breaking of chiral symmetry precisely by tuning the length of the fifth dimension L_s. However, to achieve small breaking of chiral symmetry, usually L_s needs to be of order ten or more. Thus it is more expensive than Wilson or staggered formulations.

Mathematically, one can extend the fifth dimension to infinity and replace a hyperbolic tangent function of L_s in the transformed Dirac operator to a sign function. This process [39] leads to another chiral fermion formulation called overlap fermion. Compared to domain wall formulation, overlap fermion is four dimensional. However, the Dirac operator of overlap fermion is highly non-local and not smooth, which poses a big problem in numerical simulations. With these difficulties, simulating overlap fermions is generally more expensive computationally than domain wall fermions.

3.1.2 Gauge Theory on the Lattice

We now put the gauge fields onto the lattice and impose gauge invariance on the lattice action. Because of differentiating the fermion fields on the lattice, one usually ends up with a term connecting the nearest neighbor sites,

$$\bar{\psi}_x \psi_{x+\mu} \,. \tag{3.24}$$

A natural way is to assign a gauge variable to the link connecting lattice sites x and $x+\mu$, and to make the term,

$$\bar{\psi}_x U_{x,\mu} \psi_{x+\mu} \,. \tag{3.25}$$

gauge invariant. A choice used in almost all the lattice simulations is

$$U_{x,\mu} = \exp\left(igaA^c_{x,\mu} t^c\right), \tag{3.26}$$

where t^c are the generators of the gauge group and c is the color index. It can be shown that the form (3.25) is indeed gauge invariant.

To construct the gauge action, one writes the simplest gauge invariant expression with only gauge links,

$$W_p = \mathrm{Tr}\left(U_{x,\mu} U_{x+\mu,\nu} U^\dagger_{x+\nu,\mu} U^\dagger_{x,\nu}\right), \tag{3.27}$$

which is a loop on the lattice connected by four links, and usually named the plaquette. One readily finds that

$$\frac{2}{g^2}\sum_p \mathrm{Re} W_p = C - \frac{a^4}{2}\sum_x \mathrm{Tr}\, G^2_{x,\mu\nu} + \mathcal{O}(a^2) \xrightarrow{a\to 0} C - \frac{1}{2}\int d^4x\, \mathrm{Tr}\, G^2_{\mu\nu}(x) \tag{3.28}$$

gives the usual Yang-Mills action (1.1) after dropping the constant, C, and evaluating the trace. It is usually called the Wilson gauge action [40]. The summation of p in the action is over all the unique plaquettes. Usually in the lattice community, one uses lattice coupling $\beta = 6/g^2$ instead of g in the action.

3.1.2.1 Improved Gauge Actions

As a matter of fact, any arbitrary closed loop can be used to construct the Yang-Mills action as previously shown with the plaquette (3.28). One can add the terms with six-link, the 1×2 plaquette or rectangle, and use it as a part of renormalization-group improved gauge action,

$$S_G = -\frac{\beta}{3}\mathrm{Re}\left((1-8c)\sum_p W_p + c\sum_r W_r\right), \tag{3.29}$$

where W_p is the usual plaquette, W_r is the rectangle term with six-links 1×2 plaquette. One particular choice of $c = -1.4069$ is adopted in this thesis work. The action defined this way is usually called DBW2 (Double Blocked Wilson 2) [41, 42] gauge action.

The DBW2 gauge action produces smoother gauge fields at the lattice scale, for a given low energy physical scale, than other gauge actions. A detailed discussion is given in Ref. [43]. This smoothing of the gauge field might be expected to decrease the lattice artifacts, which will be addressed shortly. Additionally, using the DBW2 gauge action should help to compensate for the coarsening of the gauge fields that comes from adding more fermions.

3.1.3 Path Integral and Finite Temperature Interpretation

Now that the fermionic action and gauge action have been discussed, the path integral (3.1) can be written as

$$\begin{aligned}
\langle \mathcal{O}(\bar{\psi}, \psi, U) \rangle &= Z^{-1} \int [\mathcal{D}\bar{\psi}][\mathcal{D}\psi][\mathcal{D}U] \mathcal{O}(\bar{\psi}, \psi, U) \exp(-S_G - \bar{\psi} M \psi) \\
&= Z^{-1} \int [\mathcal{D}\bar{\psi}][\mathcal{D}\psi][\mathcal{D}U] \\
&\qquad \mathcal{O}(\frac{\partial}{\partial \eta}, \frac{\partial}{\partial \bar{\eta}}, U) \exp(-S_G - \bar{\psi} M \psi + \bar{\psi}\eta + \bar{\eta}\psi) \Big|_{\bar{\eta}=0,\, \eta=0} \\
&= Z^{-1} \int [\mathcal{D}U] \exp(-S_G) \\
&\qquad \mathcal{O}(\frac{\partial}{\partial \eta}, \frac{\partial}{\partial \bar{\eta}}, U) \det[M] \exp(\bar{\eta} M^{-1} \eta) \Big|_{\bar{\eta}=0,\, \eta=0} \\
&= Z^{-1} \int [\mathcal{D}U] \exp(-S_G) \det[M] \mathcal{O}(M^{-1}, U) \,,
\end{aligned} \tag{3.30}$$

where the gauge action S_G is (3.29), and M is the fermion matrix, which, in this thesis work, is defined as (3.14) with gauge links U inserted. Although this integration over the gauge fields is well defined and has finite number of degrees of freedom as it is formulated on a finite lattice volume, it is prohibitively expensive to calculate the integral directly. In this thesis and usually in the literature, the size of the lattice is denoted as $N_s^3 \times N_\tau$, where N_s is the length of the three directions in the three-dimensional spatial volume, while N_τ is the length of the time direction.

In this Euclidean path integral formulation, the time direction is compactified. In this temporal direction, the canonical choice for the boundary conditions, which is also used for this thesis work, is using periodic boundary condition for gauge links U and anti-periodic for fermions. The path integral partition function Z can be interpreted as a partition function for thermal dynamics and the length of the temporal direction is the

inverse temperature, or

$$T = \frac{1}{aN_\tau} \,. \tag{3.31}$$

For simulations with lattice size satisfying $N_\tau > N_s$, it follows from the Euclidean space-time symmetry of the path integral formulation that the physics should be insensitive to the boundary conditions in the temporal direction, if the finite spatial volume effects are small. Such a lattice ensemble is commonly regarded to be at "zero" temperature[2]. On the other hand, lattice ensembles with $N_\tau < N_s$ are commonly used for studying finite temperature phenomenon, and the inverse temperature of the system is directly given by N_τ. In a finite temperature system, the screening masses can be extracted from the propagators along the spatial direction.

3.2 Numerical Calculations

The typical volume of the lattice is of order $V \sim 32^3 \times 32 \simeq 10^6$, and the size of the fermion matrix M is $3V \times 3V \simeq 10^{13}$ as in the case of staggered fermion. In almost all of the lattice simulations, one uses importance sampling to estimate $\mathcal{O}$,

$$\langle \mathcal{O}(\bar{\psi}, \psi, U) \rangle \equiv \langle \mathcal{O}(M^{-1}, U) \rangle_U \simeq \frac{1}{N} \sum_{k=1}^{N} \mathcal{O}(U^{(k)}) \,, \tag{3.32}$$

where $U^{(k)}$ is a *Markov chain* [44] generated by Monte Carlo techniques and satisfies the probability distribution

$$P[U] \propto \det[M] \exp(-S_G) \,. \tag{3.33}$$

[2]Actually, a system on a lattice can never be at zero temperature with finite temporal extent.

3.2.1 Quenching, Partial Quenching and Mixed Action

Two pieces of M are explicitly shown in the last line of the path integral representation of the observable (3.30). As a matter of fact, since one of them enters the importance sampling of the gauge field and the other only appears in the construction of the operator, they can be different.

$$\langle \mathcal{O}(\bar{\psi}, \psi, U) \rangle = Z^{-1} \int [\mathcal{D}U] \exp(-S_G) \det[M_{\text{sea}}] \mathcal{O}(M^{-1}_{\text{valence}}, U) \,. \tag{3.34}$$

One speaks of *sea quark* contributions from M_{sea} and *valence quark* contributions from M_{valence}. They acquire their names due to their roles in the fermion diagrams. Since M_{valence} enters in the form of quark propagators explicitly in the observable $\mathcal{O}$, it is responsible for the explicit quark lines in the fermion diagrams, while M_{sea} is responsible for the virtual fermion loops.

In the old days, the *quenched approximation* was often used to reduce the simulation time by ignoring the fermion determinant $\det[M_{\text{sea}}]$ completely. Currently, most of the lattice theory groups still publish analyses where the masses of the fermion in M_{sea} and M_{valence} differ. This is a procedure usually called *partial quenching*. Since there are many fermion actions to choose from, some groups also uses *mixed fermion actions* in the analysis, where M_{sea} and M_{valence} differ completely.

In this thesis work, M_{sea} is of utmost importance, because all the virtual quarks (sea quarks) created in the vacuum of QCD make all the difference in the renormalization of the gauge couplings. In this work, both M_{sea} and M_{valence} are naive staggered fermion actions (equation (3.14) with gauge links inserted). An analysis done with different masses for sea and valence quark and its implications can be found in section 4.3.

3.2.2 Hybrid Monte Carlo

The tried and true method for generating the gauge configurations according to the distribution (3.33) is the *Hybrid Monte Carlo* (HMC) algorithm [45]. This algorithm combines many of the techniques used prior to its introduction.

3.2.2.1 Pseudofermions

To properly calculate the fermion determinant $\det[M]$, one uses boson fields φ (usually named *pseudofermion* fields) [46], such that the partition function can be rewritten as[3]

$$\begin{aligned} Z &= \int [\mathcal{D}U] \exp(-S_G) \det[M] \\ &= \int [\mathcal{D}U][\mathcal{D}\varphi^\dagger][\mathcal{D}\varphi] \exp(-S_G - \varphi^\dagger M^{-1}\varphi) \,. \end{aligned} \tag{3.35}$$

3.2.2.2 Molecular Dynamics

Inspired by the integration of the Hamiltonian in a classical system,

$$H = T(p) + V(q) \,, \tag{3.36}$$

one can try to evolve the gauge action with the fictitious momentum p, which is a conjugate of the gauge links U, as

$$H = \frac{1}{2}\mathrm{Tr}p_\mu^2 + S_G + S_F \,, \tag{3.37}$$

where S_G is the gauge action and S_F is the pseudofermion action introduced in (3.35). In the *molecular dynamics* (MD) algorithm [47], one evolves this Hamiltonian according

[3] This Gaussian path integral is not well defined unless all eigenvalues of the matrix M are positive definite. The actual way of doing it will be detailed in section 3.2.5.

to [48]

$$\dot{U}_{x,\mu} = iU_{x,\mu}p_{x,\mu}\,, \tag{3.38}$$

$$\dot{p}_{x,\mu} = -i\left[U_{x,\mu}\frac{\partial S}{\partial U_{x,\mu}}\right]_{\mathrm{TA}} \equiv -i\big[F_{x,\mu}\big]_{\mathrm{TA}}\,, \tag{3.39}$$

where $S = S_F[\varphi,\varphi^\dagger] + S_G[U]$ and TA represents the traceless anti-hermitian part of the matrix. Usually one generates conjugate momentum according to the distribution $P[p] \propto \exp(-p^2/2)$, and updates the gauge fields in n steps. One MD trajectory has the *trajectory length* $\tau \equiv n\delta\tau$, with $\delta\tau$ the MD *step size*. There is always an error associated with the step size $\delta\tau$.

3.2.2.3 The Procedure of HMC

Overall, the procedure of HMC can be described as the following.

1. Generate conjugate momentum according to the distribution $P[p] \propto \exp(-p^2/2)$;
2. Generate Gaussian noise η with $P[\eta] \propto \exp(-\eta^2/2)$, which corresponds to a pseudofermion field $\varphi = M^\dagger\eta$ (refer to section 3.2.5);
3. Do an MD evolution according to equation (3.38) and (3.39) (this is usually called one trajectory in the literature and throughout this thesis);
4. Accept the new configuration with the probability $\min\{1, \exp(-\Delta H)\}$.

The last step is usually called the Metropolis [49] accept/reject step, which removes any error from the numerical integration of the classical molecular dynamics.

3.2.3 Multiple-timescale Integration Method

The Sexton–Weingarten multiple-timescale integration method [50] separates the forces into different pieces and uses a different step size $\delta\tau$ for these different forces. Usually, the gauge force in the Hamiltonian (3.37) is larger than the forces generated by the fermions, but the gauge force is also cheaper to calculate since it does not involve the inversion of the fermion matrix. One can then integrate the gauge links with a smaller step size than that used to calculate the forces from the fermions, in order to reduce the error of the integration. However, this argument becomes less accurate when the number of fermions increases, which leads to a larger force from the fermions.

In this thesis work, gauge forces are calculated and gauge links are updated twice per fermion force calculation and pseudofermion updating in the MD integration.

3.2.4 Integration Scheme

The exact way of integrating one MD trajectory depends on the chosen integration scheme. At the beginning of this thesis work, the Omelyan integrator [51] was used. It is an integrator with an error of order $\delta\tau^2$, which can be further tuned by a parameter to minimize the error. A new scheme, the force gradient integrator [52], was proposed later and then developed and implemented by Hantao Yin [53]. The force gradient integrator (FGI) usually has an error of order $\delta\tau^4$, and does not need an extra parameter. However, the significantly reduced integration error only becomes a real benefit when the integration error $\Delta H \ll 1$. With the usual practice of $\Delta H \simeq 0.5$, the Omelyan integrator is not much worse than the FGI. Nevertheless, the FGI does not require tuning of an additional parameter, and combined with multiple-timescale integration methods 3.2.3 and multiple mass preconditioning 3.2.5.3, it encourages the use of loose stopping conditions for the

inversion of the fermion matrix. For these reasons, the FGI has been used in this work with the recent lattice simulations replacing the Omelyan integrator.

3.2.5 Inverting the Fermion Matrix in the Molecular Dynamics

In the evolution of the lattice gauge configurations and in most of the measurements, the majority of the computational time is spent on inverting the fermion matrix. Many tricks and techniques have been developed for dealing with the fermion matrix (3.35) in the MD evolution.

3.2.5.1 Even and Odd Sites

In fact, the equation (3.35) previously written down cannot be used in the simulation. For it to be inverted using iterative methods like the conjugate gradient[54], the sparse matrix has to be positive-definite. The fermion matrix M generally is not positive-definite. Instead, $M^\dagger M$ is usually used. For staggered fermions, $M = D + m$, where D only connects even and odd sites. Thus, $M^\dagger M$ only connects even sites to even sites, and odd to odd. One can rewrite the fermion determinant in equation (3.35) as

$$\begin{aligned}
\det[M] &= \left(\det[M^\dagger M]\right)^{\frac{1}{2}} \\
&= \int [\mathcal{D}\varphi^\dagger][\mathcal{D}\varphi] \exp\left(-\frac{1}{2}\varphi^\dagger (M^\dagger M)^{-1}\varphi\right) \\
&= \int [\mathcal{D}\varphi^\dagger][\mathcal{D}\varphi] \exp\left(-\frac{1}{2}\left(\varphi_e^\dagger (M^\dagger M)^{-1}_{ee}\varphi_e + \varphi_o^\dagger (M^\dagger M)^{-1}_{oo}\varphi_o\right)\right) \\
&= \int [\mathcal{D}\varphi_e^\dagger][\mathcal{D}\varphi_e] \exp\left(-\varphi_e^\dagger (M^\dagger M)^{-1}_{ee}\varphi_e\right) \\
&= \det\left[(M^\dagger M)_{ee}\right],
\end{aligned} \tag{3.40}$$

where the subscripts $_e$ and $_o$ are used to indicate values defined on even or odd sites ($\sum_k x_k$ being even or odd). Therefore, only the pseudofermion fields defined on even (odd) lattice sites are needed.

3.2.5.2 Rational Approximation

So far, the algorithm has been discussed with one copy of the fermion determinant. To simulate an arbitrary number of fermion flavors, one can use a rational approximation expressed in terms of a partial-fraction expansion for M raised to some power $-a$ with $0 < a < 1$,

$$M^{-a} \simeq r(M) = \alpha_0 + \sum_{k=1}^{d} \frac{\alpha_k}{M + \beta_d}\,, \tag{3.41}$$

to replace M^{-1} in the previous discussions. This leads to the *rational hybrid Monte Carlo* (RHMC) algorithm [55, 56, 57]. The rational approximation does not introduce much additional cost with the multiple inversions, because the term $(M + \beta_d)^{-1}\varphi$ can be calculated simultaneously for different β_d with the multi-shift solver [58].

The RHMC can be used to speed up simulations by introducing more stochastic averaging with multiple pseudofermion fields [59], where one takes the n^{th} root of the fermion matrix, and averages over n copies of pseudofermion fields. This gives better estimations of the inversion of the fermion matrix and reduces the error associated with force associated with fermions in the MD integration. This thus enables the use of a larger step size which decreases the simulation time effectively.

In this thesis work, the RHMC algorithm with Omelyan integrator [4] was used for all the simulations with eight flavors, and for simulations with twelve flavors of quark

[4] FGI was not available then.

masses $m_q \geq 0.01$. It is done by rewriting the fermion determinant with

$$\left(\det[M^\dagger M]\right)^2 = \left(\det[(M^\dagger M)^{\frac{2}{3}}]\right)^3 \qquad \text{for 8 flavors;} \tag{3.42}$$

$$\left(\det[M^\dagger M]\right)^3 = \left(\det[(M^\dagger M)^{\frac{3}{4}}]\right)^4 \qquad \text{for 12 flavors.} \tag{3.43}$$

The subscripts $_{ee}$ are omitted here. Note that M for staggered fermion already represents four flavors.

3.2.5.3 Mass Preconditioning

Another technique for dealing with the fermion determinant is the Hasenbusch mass preconditioning [60]. Basically, the fermion determinant can be written as

$$\det[M(m_q)] = \det\left[\frac{M(m_q)}{M(m_h)}\right]\det[M(m_h)]\,, \tag{3.44}$$

with $m_h > m_q$. There are several benefits from this technique. First, similar to the n^{th} root technique, it also introduces more copies of pseudofermion fields, and thus reduces the error in the force associated with fermion determinant, which in turn enables a larger MD step size. Second, the fermion matrix with a heavier mass reduces the condition number on the fermion matrices, and the numerical cost in the conjugate gradient can be drastically decreased [61]. Third, looser stopping conditions for conjugate gradient methods can be used for the fermion matrix with larger fermion masses, which also reduces the CG count dramatically.

This technique is more beneficial when fermion masses becomes smaller. However, much overhead was observed using RHMC with mass preconditioning. Therefore, a sequence of multiple intermediate masses for the preconditioning (four or five additional

masses) is introduced and used in this thesis work for simulations with twelve flavors of $m_q < 0.01$. It is used in combination with HMC without the rational approximation. FGI has been employed in these simulations.

3.3 Measurements with Staggered Fermion

3.3.1 Staggered Fermion Correlators

Constructing a fermionic correlator from staggered fermion is non-trivial, since the spin and flavor degrees of freedom scatter in the hypercube. One can use the symmetry of the lattice as a guide and relate the lattice symmetry groups to the continuum ones and identify the lattice states as the continuum ones [62].

An intuitive but less rigorous way [35] is by starting from the spin-taste basis. To construct a mesonic four-fermion operator, the desired bilinear for the interpolating operator can have the form of

$$\bar{\Psi}^{f}_{x,\,a\alpha}\left(\Gamma_S^{ab}\otimes\Gamma_T^{*\,\alpha\beta}\right)\Psi^{f'}_{x,\,b\beta}\,, \tag{3.45}$$

where flavor indices f and f' are shown explicitly, and not to be confused with the taste degree of freedom. The combination of gamma matrices, $\Gamma_S\otimes\Gamma_T$, pick the desired states, and they act on the spin and taste spaces, respectively.

Converting back to the normal staggered fermion basis, the operator can be written as

$$\mathcal{O}_{ff'ST} = \sum_{\eta\eta'}\bar{\chi}^{f}_{2x+\eta'}g_{ST}(\eta',\eta)\chi^{f'}_{2x+\eta}/16\,, \tag{3.46}$$

where

$$g_{ST}(\eta', \eta) = \frac{1}{4}\mathrm{Tr}\left(\tilde{\Gamma}^{\dagger}_{\eta'}\Gamma_S\tilde{\Gamma}_{\eta}\Gamma^{\dagger}_T\right) . \tag{3.47}$$

Using the Goldstone pion as a demonstration, one needs $\gamma_5 \otimes \gamma_5$, which simplifies the interpolating operator to

$$\mathcal{O}_{du55}(x) = \sum_{\eta}(-1)^{\eta}\bar{\chi}^{d}_{2x+\eta}\chi^{u}_{2x+\eta} . \tag{3.48}$$

As a result, the zero momentum meson correlator induced by this operator is

$$\begin{aligned} C_{\pi^+,5}(2t) &= \sum_{x}\langle\bar{\mathcal{O}}_{ud55}(x)\mathcal{O}_{du55}(0)\rangle \\ &= \sum_{x,\eta\eta'}\mathrm{Tr}\left(G(2x+\eta',\eta)G^{\dagger}(2x+\eta',\eta)\right) . \end{aligned} \tag{3.49}$$

Here, the summation over x is only on a particular time slice of the lattice. This formula is very unfortunate, because the operator involves two adjacent time slices. The summation of η and η' involves η_4, which in turn requires quark propagators to have the source and sink separations of $2t-1$, $2t$ and $2t+1$.

For a general $\Gamma_S \otimes \Gamma^*_T$, one can systematically remove these irregular propagators by adding or subtracting $\Gamma_S\gamma_4\gamma_5 \otimes (\Gamma_T\gamma_4\gamma_5)^*$. Recognizing $g_{ST}(\eta) = g_{S45\,T45}(\eta)(-1)^{\eta_4}$, this term can be used to cancel one of the time slice contributions. However, this also adds an additional spin, parity and taste content to the propagator, and in turn makes the correlator corresponds to two opposite parity states $\exp(-Et)$ and $(-1)^t\exp(-E't)$ with a single correlator at even or odd time t.

With the aforementioned process, one can write the Goldstone pion correlator as

$$C_{\pi^+,5}(t) = \sum_x \mathrm{Tr}\left(G(x,0)G^\dagger(x,0)\right) . \tag{3.50}$$

Specially for this Goldstone pion correlator, the added content $\gamma_4 \otimes \gamma_4$ is the density for a conserved charge and does not excite states from the vacuum. Therefore, this correlator (3.50) couples only to the Goldstone pion.

With the same procedure, one can write all the local operators with $\Gamma_S = \Gamma_T$, and the propagator can be written as

$$C(t) = \sum_x \sigma(x)\mathrm{Tr}\left(G(x,0)G^\dagger(x,0)\right) . \tag{3.51}$$

The sign factor σ projects out states with definite quantum number J^{PC} as listed in table 3.1. The meson masses of the lowest energy states at the large t limit can be extracted by fitting the propagator to the form

$$\begin{aligned} C(t) = {} & C_1\left(e^{-m_1 t} + e^{-m_1(N_\tau - t)}\right) \\ & + (-1)^t C_2\left(e^{-m_2 t} + e^{-m_2(N_\tau - t)}\right) , \end{aligned} \tag{3.52}$$

at large t.

channel	$\sigma(x)$	J^{PC}(state)	
PS	1	$0^{-+}(\pi)$	0^{+-}
SC	$(-1)^{x_1+x_2+x_3}$	$0^{-+}(\pi_2)$	$0^{++}(\sigma)$
VT	$(-1)^{x_1} + (-1)^{x_2} + (-1)^{x_3}$	$1^{--}(\rho)$	$1^{+-}(b_1)$
PV	$(-1)^{x_1+x_2} + (-1)^{x_2+x_3} + (-1)^{x_3+x_1}$	$1^{--}(\rho_2)$	$1^{+-}(a_1)$

Table 3.1: Meson states projected from staggered local propagator. Only the contribution from the connected diagram is included for the σ meson in this propagator.

The effect of flavor (taste) symmetry breaking in staggered fermions can be measured with $\gamma_5 \otimes \Gamma_T$ for different taste multiplets Γ_T.

3.3.2 Measuring f_π with staggered fermion

From the definition of f_π (1.7), one can write it explicitly with the flavor content in Euclidean space-time,

$$\sqrt{2} f_\pi m_\pi = \langle 0 \left| \bar{u} \gamma_4 \gamma_5 d \right| \pi^+(\vec{p}=0) \rangle \,, \tag{3.53}$$

where the factor of $\sqrt{2}$ is from the current normalization $\frac{1}{\sqrt{2}}(j_\mu^{51} + i j_\mu^{52})$. With the PCAC relation (1.9), one can use another definition for f_π,

$$\sqrt{2} f_\pi m_\pi^2 = (m_u + m_d) \langle 0 \left| \bar{u} \gamma_5 d \right| \pi^+(\vec{p}=0) \rangle \,. \tag{3.54}$$

This definition is favored and used in this thesis work, because the matrix element can be directly extracted from the point-point pion correlator (3.50), given by

$$C_{\pi^+,5}(t) = \sum_x \mathrm{Tr}\left(G(x,0) G^\dagger(x,0) \right) = 4 \sum_x \langle 0 \left| (\bar{u}\gamma_5 d)_x (\bar{d}\gamma_5 u)_0 \right| 0 \rangle \,, \tag{3.55}$$

where the factor of four comes from the fact that the staggered correlator implicitly has four species [63]. Inserting the Lorentz covariantly normalized pion states, one finds in the long time limit

$$C_{\pi^+,5}(t) \xrightarrow{t\to\infty} \frac{f_\pi^2 m_\pi^3}{m_q^2} e^{-m_\pi t} \,. \tag{3.56}$$

In the Columbia Physics System (CPS), which is used in this thesis work, the nor-

malization of the computed propagator has an additional factor of two,

$$G^{\mathrm{CPS}}(x,y) = \frac{1}{2}G(x,y)\,. \tag{3.57}$$

This is because CPS internally uses

$$M^{\mathrm{CPS}}_{xy} = \sum_{\mu}\eta_{\mu x}\left(U_{\mu x}\delta_{y\,x+\mu} - U^{\dagger}_{\mu\,x-\mu}\delta_{y\,x+\hat{\mu}}\right) + 2m\delta_{x,y}\,, \tag{3.58}$$

as the fermion matrix, which is as twice as the one in equation (3.14). Therefore, in the CPS convention, $C_{\pi^+,5}(t)$ receives an additional factor of four, and the value of f_π can be obtained via

$$C^{\mathrm{CPS}}_{\pi^+,5}(t) \xrightarrow{t\to\infty} \frac{f_\pi^2 m_\pi^3}{4m_q^2}e^{-m_\pi t}\,. \tag{3.59}$$

3.3.3 Extended Sources for Propagators

In the previous sections, the point to point propagator $G(x,0)$ is used. One can also use extended sources for quark propagators,

$$M^{\alpha\beta}G^{\beta\gamma}(x,\Omega) = \delta^{\alpha\gamma}\sum_{\vec{\omega}\in\Omega}\delta(\vec{x}-\vec{\omega})\,. \tag{3.60}$$

where α, β and γ are color indices. The time slice of the lattice where Ω is located is Coulomb gauge fixed. Choose

$$\Omega \equiv 2Z = \left\{\vec{x}\,\middle|\, x_k \text{ even}, k = 1, 2 \text{ and } 3\right\}\,, \tag{3.61}$$

such that the summation in equation (3.60) is over the origins of all the hypercubes. Therefore it does not change the desired states from the meson interpolation opera-

tor (3.45) at all. This is called WALL2Z source.

In this thesis work, the WALL2Z source with spatial size fixed at 16^3 has been used instead of the full spatial extend of the lattice. The meson results from this source are quoted as the final results, because it couples better with the meson states and produce better effective mass plots. However, the value of f_π is determined from the point propagator. Because with the summation in (3.60), the amplitude can no longer be interpreted as simply as (3.56).

3.3.4 Measuring the Chiral Condensate

The chiral condensate can be calculated as

$$\begin{aligned} \langle \bar{\psi}\psi \rangle &= \frac{1}{N}\langle \mathrm{Tr} M^{-1} \rangle \\ &= \frac{1}{N}\eta^* M^{-1}\eta \\ &= \frac{1}{N}\eta^* (M^\dagger M)^{-1} M^\dagger \eta \,, \end{aligned} \tag{3.62}$$

where η is a set of Gaussian random number, and N is the normalization constant. In this thesis work, the Columbia Physics System (CPS) is used, where the normalization for $\langle \bar{\psi}\psi \rangle$ is $N = 3V$ for staggered fermion action, where 3 is the number of colors and V is the volume of the lattice. The normalization is chosen such that

$$\lim_{m\to\infty} \longrightarrow \frac{1}{m} \,. \tag{3.63}$$

Note, it actually corresponds to four flavors in the case of the staggered fermion action.

3.3.5 Measuring the Quark Potential

To get measurements about the static quark potential, the Coulomb gauge fixing method, which is introduced in Ref. [64] and developed for CPS by Min Li [65], is used in this thesis. To use this method, one first uses Coulomb gauge fixing on the three spatial dimensional hyperplane, and then computes the Wilson loops as the trace of the product of pairs of temporal links whose ends are fixed in Coulomb gauge. In this method, most of the time is spent on gauge fixing. Since only the temporal links are used, the code is pretty easy to get parallelized. To get a better signal, the method is repeated for each of four directions on the lattice chosen as the temporal direction, and then the average of the Wilson loops are obtained.

After obtaining Wilson loops using this method, they are fitted along temporal separation to get the quark potential $V(r)$ according to the form,

$$W(r,t) = A(r)\exp(-V(r)t) + \cdots, \tag{3.64}$$

where the excited states go away in large t. Here, $V(r)$ is the static quark potential when t is asymptotically large, and $A(r)$ is a coefficient depending on r. Then the quark potential is fitted along the spatial separation to the form of the Cornell potential (1.2) with an additional constant term,

$$V(r) = V_0 - \frac{\alpha}{r} + \sigma r\,. \tag{3.65}$$

No other restriction for V_0, α and σ is imposed. From the fitting parameters, the commonly called Sommer scale [66] is obtained

$$r_0 = \sqrt{\frac{1.65-\alpha}{\sigma}}\,. \tag{3.66}$$

Another scale r_1, which is also commonly used, is defined as

$$r_1 = \sqrt{\frac{1-\alpha}{\sigma}}\,. \tag{3.67}$$

3.4 Choice of Gauge and Fermion Actions

For this thesis work, the naive staggered fermion action is chosen for its remnant chiral symmetry and its simulation speed. To help control the finite lattice spacing artifacts of staggered fermions, the DBW2 gauge action is used.

The RHMC algorithm is chosen for this thesis work at the beginning, because it is an exact algorithm and allows any number of flavors, although only eight and twelve flavors are studied, which do not require fractional powers. The software implementation in CPS includes many optimizations, and is extensively used for other 2 + 1 flavor simulations with domain wall and staggered fermions.

Algorithm	Φ	RHMC
Run Length	1000 ~ 4760	1290 ~ 3840
Acceptance Rate	0.87	0.60
Measurement Interval	5	10
Plaquette	0.560130(14)	0.560072(39)
$\langle\bar{\psi}\psi\rangle$	0.0404(1)	0.04105(35)
m_π	0.3210(40)	0.3114(22)
m_{π_2}	0.3543(35)	0.3509(46)
m_ρ	0.4763(59)	0.4558(40)
m_{ρ_2}	0.4777(84)	0.4554(42)

Table 3.2: A comparison between RHMC and Φ algorithm results using naive staggered fermions and the Wilson gauge action for $N_f = 4$, $m_q = 0.015$, $\beta = 5.4$. Meson masses are from WALL2Z sources. In the Φ algorithm, the fitting ranges for m_π, m_{π_2}, m_ρ and m_{ρ_2} are 10-16, 7-16, 6-16 and 6-16, respectively, while in RHMC algorithm, the fitting ranges are all set to 6-16.

To check it for the current task, results from a 4-flavor simulation done using the recent software, done as a 2 + 2-flavor RHMC simulation (which requires the square root of the staggered fermion determinant), are compared with previous results [67] using the Φ algorithm. In Table 3.2, the plaquette, $\langle\bar{\psi}\psi\rangle$, and masses of 4 meson channels are compared (values are in units of lattice spacing). The plaquette values agree within 1 standard deviation, while the masses differ by 2 to 3 standard deviations, making it likely that there are long autocorrelation times in the simulations which are not under good control.

Since the FGI became available in CPS, the algorithm for this thesis has changed to HMC using FGI with the multiple mass preconditioning technique. The integrator has an error of the order of $\delta\tau^4$, and the multiple mass preconditioning technique packs more averaging for the fermion determinant, which reduces error. This provides better performance for smaller quark masses $m_q < 0.01$ required in the twelve-flavor simulations.

3.5 History of This Project and Computational Cost

This thesis work spans roughly four years. From the beginning, in the fall of 2007, a 64-node partition of QCDOC located at Columbia University was used for testing and developing. Later, one or two 256-node partitions were used for the beginning of the eight-flavor simulations. In May of 2008, BlueGene/L (BGL) as part of the NYBlue project located in BNL became available. Since then, most of the eight-flavor simulations were done on BGL. The twelve-flavor simulations became a serious production work on BGL since the beginning of 2009. Nevertheless, the spectrum measurements were always performed on QCDOC because of an unknown bug in CPS. Since September of 2010, when BGL started tightening the allocation of node-hours, 450 K node-hours

have been used up each month, and one or two 1 K-node racks of QCDOC located in BNL have been continuously used. There are three conference proceedings previously reported [68, 69, 70] on the progress of this thesis work.

Presume BGL (two cores per node) has the same performance as QCDOC per core (which slightly overestimates the power of BGL) the total node-hour used in the last year can be estimated as 2 M per month or 24 M core-hours per year, assuming 1.5 racks of QCD in active use. If previous two years' usage (from 2008 to 2010) can be estimated as similar as the last year, that makes the total computational cost of this project to be more than 70 M core-hours.

Part II

Simulations and Analysis

Chapter 4

Simulation Results at Zero Temperature

4.1 Simulation Details and Ensemble Properties

In all measurements, the data were blocked in 80 trajectories, with the length of each trajectory one half MD unit. During the lattice generation, plaquette values, Wilson lines and various RHMC statistics were saved at each trajectory, lattice configurations were saved at every 10th trajectory, and the value of $\langle\bar{\psi}\psi\rangle$ was calculated 10 times for each saved configuration, to provide a better estimate of the chiral condensate. Both ordered and disordered starts were performed to search for the possible bulk transition. The disordered starts were stopped after they had merged with the ordered starts. And further measurements of various meson spectra, and static quark potentials were done on the saved lattice configurations from an ordered start, which results in a block size of 8 (80 trajectories / 10 trajectories per saved configuration) saved lattice configurations during the rest of the analysis. Except for the $\beta = 0.54$, $m_q = 0.02$, $16^3\times 32$ ensemble, indicated in table 4.1, the ordered starts were stopped and the disordered starts were used for observable measurements, because of certain arrangements of running jobs; also for one

β	m_q	Size	Trajectories	$e^{-\Delta H}$	acceptance
0.54	0.01	$16^3\times32$	1050-5520	1.0018(94)	0.7442(39)
		$24^3\times32$	1030-2860	0.987(19)	0.7021(72)
	0.02	$16^3\times32$	990-5300	1.007(12)	0.7292(42)
	0.03	$16^3\times32$	1030-6220	0.9934(71)	0.7850(34)
0.56	0.008	$16^3\times32$	990-2580	0.9988(77)	0.8797(29)
		$24^3\times32$	980-2970	1.020(14)	0.7710(73)
	0.016	$16^3\times32$	1020-3730	0.9760(94)	0.7635(50)
		$24^3\times32$	960-3190	0.967(19)	0.6732(93)
	0.024	$16^3\times32$	1010-4920	1.0045(77)	0.8156(37)
		$24^3\times32$	1030-3340	0.988(18)	0.6664(58)
0.58	0.015	$16^3\times32$	920-1950	0.992(13)	0.8048(60)
		$24^3\times32$	1020-2930	1.038(18)	0.7332(59)
		$32^3\times32$	1030-1900	1.108(43)	0.6707(99)
	0.025	$16^3\times32$	1330-2760	0.9932(86)	0.8542(37)
		$24^3\times32$	1000-3390	0.975(15)	0.7198(56)

Table 4.1: Parameters and ensemble properties of simulations for eight flavors. The provided number of "Trajectories" are those trajectories used for measurements and analysis. Ordered starts were used for measurements, except for the ensemble with $\beta = 0.54$ and $m_q = 0.02$, where the disordered start was used.

ensemble with twelve flavors, $\beta = 0.47$, $m_q = 0.01$, $24^3\times32$, indicated in table 4.3, due to a limited number of configurations generated because of a longer thermalization time in tuning the RHMC parameters, blocks of 30 trajectories were used for measurements. In this chapter and the rest of the thesis, all numeric values of dimensionful quantities are in units of the lattice spacing, unless the units are explicitly shown.

In this chapter, zero temperature results for selected ensembles for eight and twelve flavors are shown. The discussion for twelve-flavor results obtained at smaller quark masses $m_q < 0.01$ is delayed until section 6.2.

Simulation parameters of the major lattice ensembles for eight and twelve flavors are shown in Table 4.1 and 4.3, respectively. The meaning of the parameters were given in section 3.2.2, previously. In the tables, the column of "Trajectories" denotes the con-

β	m_q	Size	$\langle\bar{\psi}\psi\rangle$	plaquette
0.54	0.01	$16^3\times32$	0.14465(28)	0.521110(39)
		$24^3\times32$	0.14396(35)	0.521206(47)
	0.02	$16^3\times32$	0.19646(23)	0.514935(44)
	0.03	$16^3\times32$	0.23102(16)	0.509912(36)
0.56	0.008	$16^3\times32$	0.06158(36)	0.543294(23)
		$24^3\times32$	0.06147(15)	0.543322(13)
	0.016	$16^3\times32$	0.10148(22)	0.541264(25)
		$24^3\times32$	0.10212(11)	0.541166(14)
	0.024	$16^3\times32$	0.13645(16)	0.538576(24)
		$24^3\times32$	0.13669(12)	0.538529(19)
0.58	0.015	$16^3\times32$	0.06585(14)	0.557866(25)
		$24^3\times32$	0.06653(10)	0.557803(12)
		$32^3\times32$	0.066325(63)	0.5578214(78)
	0.025	$16^3\times32$	0.09973(27)	0.556335(28)
		$24^3\times32$	0.100416(86)	0.556250(14)

Table 4.2: The averaged plaquette value and $\langle\bar{\psi}\psi\rangle$ from simulations for eight flavors.

figurations in MD trajectory numbers that are used in the analysis, after discarding the configurations still in the process of thermalization; the value of $e^{-\Delta H}$ is the exponential of the change of the fictitious Hamiltonian, whose average should be 1 if the ensemble is thermalized; and the "acceptance" is the ensemble average of the probability $\min\{1, \exp(-\Delta H)\}$ used in the Metropolis step at the end of each MD trajectory. The values of chiral condensate[1] and plaquette are given in Table 4.2 and Table 4.4 for eight and twelve flavors, respectively. Jackknife re-sampling techniques, which are described in the appendix A.1, were used to analyze the statistical error. The quoted errors in these tables are only statistical errors from blocking and Jackknife. Systematic errors will be described on a per measurement basis later.

In the following sections, the uncorrelated χ^2 was used in all of the fits, because the

[1]The chiral condensate is normalized to be for four flavors and averaged per color, as described in section 3.3.4

β	m_f	Size	Trajectories	$e^{-\Delta H}$	acceptance
0.45	0.01	$16^3\times32$	860-2370	1.013(22)	0.7042(79)
	0.02	$16^3\times32$	830-2740	1.0041(73)	0.8586(34)
	0.03	$16^3\times32$	850-2600	0.9990(75)	0.9057(33)
0.46	0.01	$16^3\times32$	810-2400	0.872(79)	0.3198(80)
	0.02	$16^3\times32$	830-2020	0.934(58)	0.5403(91)
	0.03	$16^3\times32$	850-2680	0.980(18)	0.6856(54)
0.47	0.01	$16^3\times32$	810-2560	1.029(44)	0.5760(74)
		$24^3\times32$	1460-1990*	1.005(20)	0.7868(73)
		$32^3\times32$	840-1790	1.002(39)	0.6857(83)
	0.015	$16^3\times32$	860-3170	0.897(25)	0.5721(69)
	0.0175	$16^3\times32$	800-3270	1.012(30)	0.5948(75)
	0.02	$16^3\times32$	860-2050	1.010(32)	0.6152(94)
		$24^3\times32$	2310-3340	0.972(21)	0.7054(83)
	0.025	$16^3\times32$	830-2100	1.047(32)	0.6877(87)
	0.03	$16^3\times32$	870-2700	0.980(15)	0.7072(64)
0.475	0.01	$16^3\times32$	860-1810	0.977(34)	0.6060(73)
		$24^3\times32$	850-2280	1.004(10)	0.8126(45)
	0.02	$16^3\times32$	820-4170	0.995(14)	0.6753(55)
	0.03	$16^3\times32$	810-2720	0.993(16)	0.7261(44)
0.48	0.01	$16^3\times32$	810-2080	0.998(29)	0.653(15)
		$24^3\times32$	850-2200	0.9834(72)	0.8213(44)
		$32^3\times32$	840-2030	1.010(24)	0.7337(75)
	0.02	$16^3\times32$	800-4310	1.019(12)	0.7332(46)
		$24^3\times32$	820-2250	0.989(11)	0.8685(49)
	0.03	$16^3\times32$	830-2740	0.998(14)	0.7522(74)
0.49	0.01	$16^3\times32$	800-2310	0.977(19)	0.6945(61)
		$32^3\times32$	830-2100	0.960(11)	0.7494(65)
	0.02	$16^3\times32$	830-2180	0.986(15)	0.7751(67)
	0.03	$16^3\times32$	840-1950	0.984(16)	0.7970(73)
0.50	0.01	$16^3\times32$	860-2530	1.030(21)	0.7356(71)
	0.02	$16^3\times32$	860-2210	0.994(12)	0.7995(47)
	0.03	$16^3\times32$	800-1990	1.003(13)	0.8400(55)

Table 4.3: Parameters and ensemble properties of simulations for twelve flavors. The provided number of "Trajectories" are those trajectories used for measurements and analysis. Blocks of 30 trajectories is used for the ensemble labeled with *.

β	m_f	Size	$\langle\bar{\psi}\psi\rangle$	plaquette
0.45	0.01	$16^3\times32$	0.32521(24)	0.438841(86)
	0.02	$16^3\times32$	0.34687(17)	0.433429(51)
	0.03	$16^3\times32$	0.36290(14)	0.429172(47)
0.46	0.01	$16^3\times32$	0.26870(81)	0.46159(21)
	0.02	$16^3\times32$	0.31240(35)	0.45113(11)
	0.03	$16^3\times32$	0.33586(12)	0.445219(42)
0.47	0.01	$16^3\times32$	0.09047(29)	0.499437(36)
		$24^3\times32$	0.09108(18)	0.499444(25)
		$32^3\times32$	0.09156(14)	0.499404(19)
	0.015	$16^3\times32$	0.17613(89)	0.48930(16)
	0.0175	$16^3\times32$	0.22488(38)	0.480376(82)
	0.02	$16^3\times32$	0.25025(38)	0.475026(90)
		$24^3\times32$	0.24997(26)	0.475111(61)
	0.025	$16^3\times32$	0.27868(42)	0.46857(12)
	0.03	$16^3\times32$	0.29695(25)	0.464180(81)
0.475	0.01	$16^3\times32$	0.07809(36)	0.504488(35)
		$24^3\times32$	0.07651(15)	0.504623(16)
	0.02	$16^3\times32$	0.18298(53)	0.492759(97)
	0.03	$16^3\times32$	0.26986(33)	0.475247(92)
0.48	0.01	$16^3\times32$	0.06560(27)	0.509371(36)
		$24^3\times32$	0.06662(10)	0.509293(13)
		$32^3\times32$	0.066839(50)	0.509268(10)
	0.02	$16^3\times32$	0.13642(26)	0.503794(35)
		$24^3\times32$	0.13750(17)	0.503630(20)
	0.03	$16^3\times32$	0.23246(40)	0.488078(91)
0.49	0.01	$16^3\times32$	0.05326(29)	0.517924(22)
		$32^3\times32$	0.054203(68)	0.5178681(83)
	0.02	$16^3\times32$	0.10335(24)	0.515238(26)
	0.03	$16^3\times32$	0.15996(36)	0.509369(52)
0.50	0.01	$16^3\times32$	0.044202(84)	0.525995(14)
	0.02	$16^3\times32$	0.08816(16)	0.524097(24)
	0.03	$16^3\times32$	0.12876(13)	0.521058(30)

Table 4.4: The averaged plaquette value and $\langle\bar{\psi}\psi\rangle$ from simulations for twelve flavors.

limited statistics could not provide enough information to determine the correlation matrix, and an uncorrelated χ^2 gave better control over the convergence of the fits.

4.2 Meson Spectroscopy

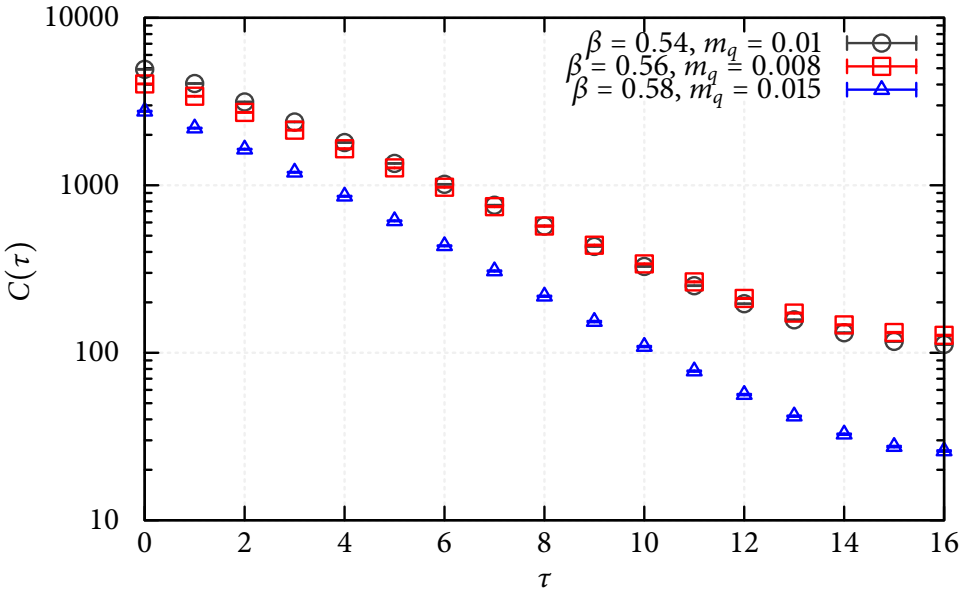

Figure 4.1: Pion propagator with eight flavors.

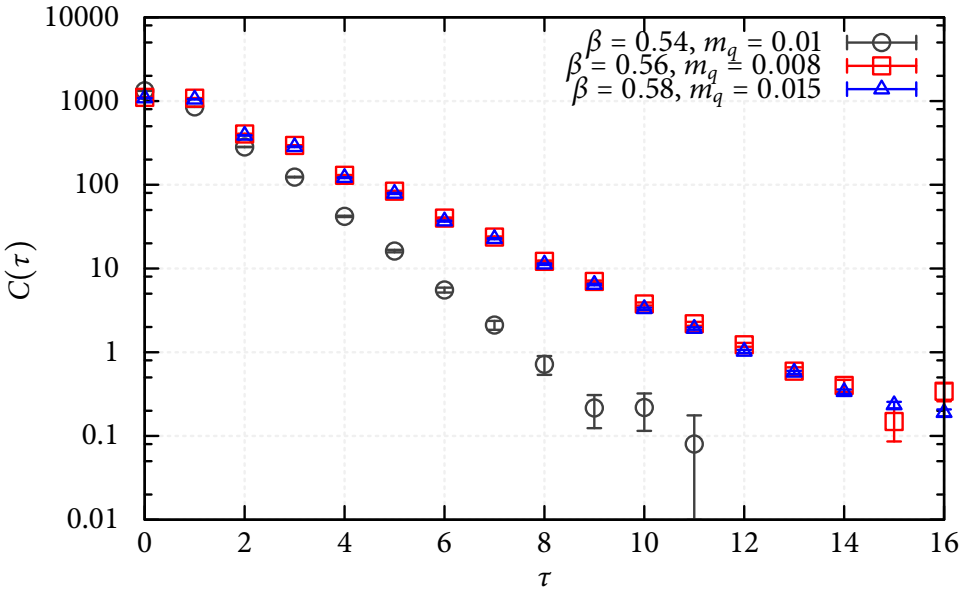

Figure 4.2: Rho propagator with eight flavors.

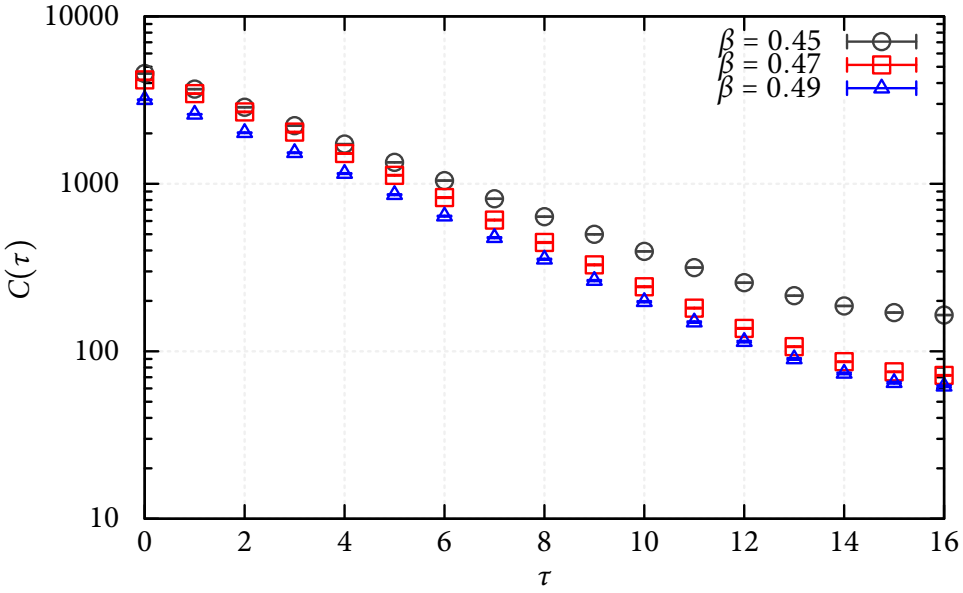

Figure 4.3: Pion propagator with twelve flavors at $m_q = 0.01$.

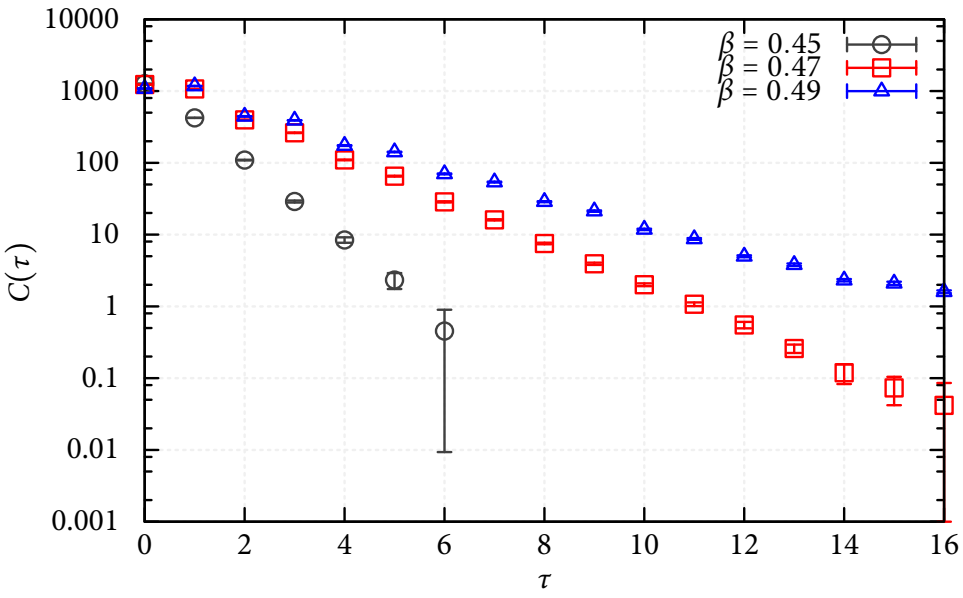

Figure 4.4: Rho propagator with twelve flavors at $m_q = 0.01$.

As stated before, a source size of 16^3 is used for all the zero temperature WALL2Z propagators to extract meson masses. Figure 4.1, 4.2, 4.3 and 4.4 show typical WALL2Z propagators for pion and rho extracted from a few ensembles. Only $\tau = 0 \sim 16$ is displayed in these figures, since the propagators are folded and $N_\tau = 32$ was used in all of the zero temperature simulations. These propagator shows very clear exponential behavior, indicating massive particle states and in contrast with power law behavior that would occur in a conformal theory. For strong coupling (small input β), the ρ propagators can be very noisy for larger values of τ, thus the figures do not show some values of the propagators for large τ.

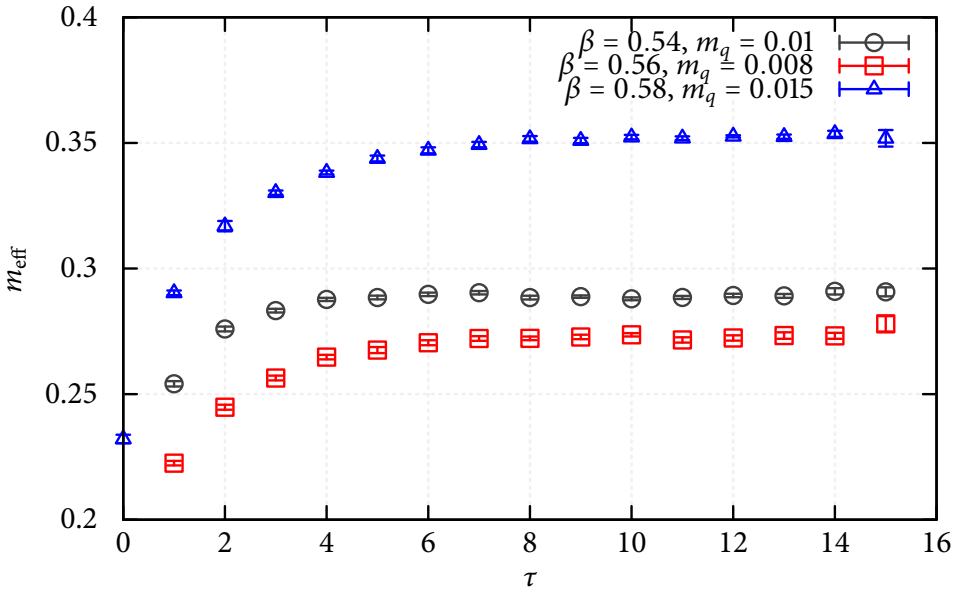

Figure 4.5: Pion effective mass plot for eight flavors.

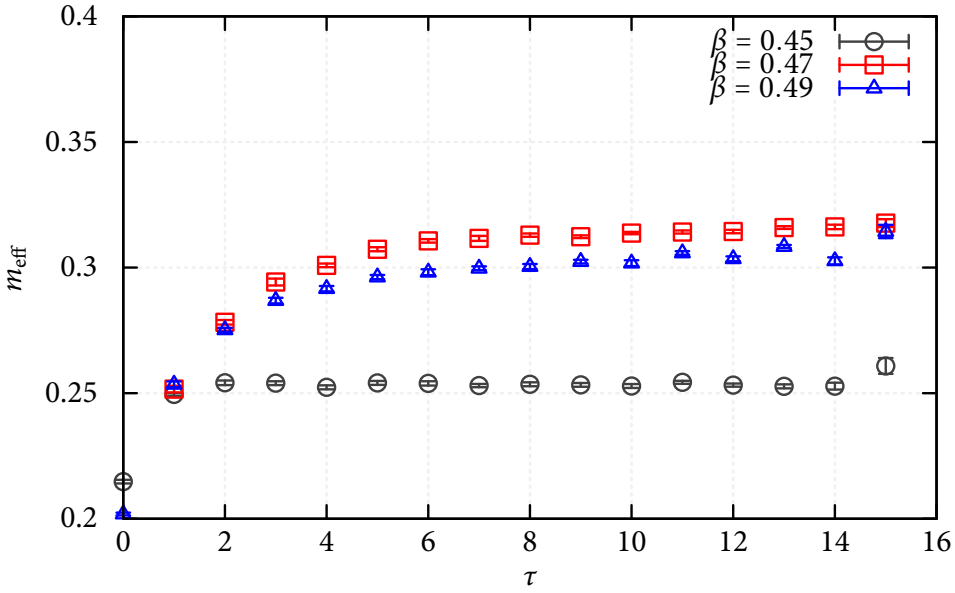

Figure 4.6: Pion effective mass plot for twelve flavors at $m_q = 0.01$.

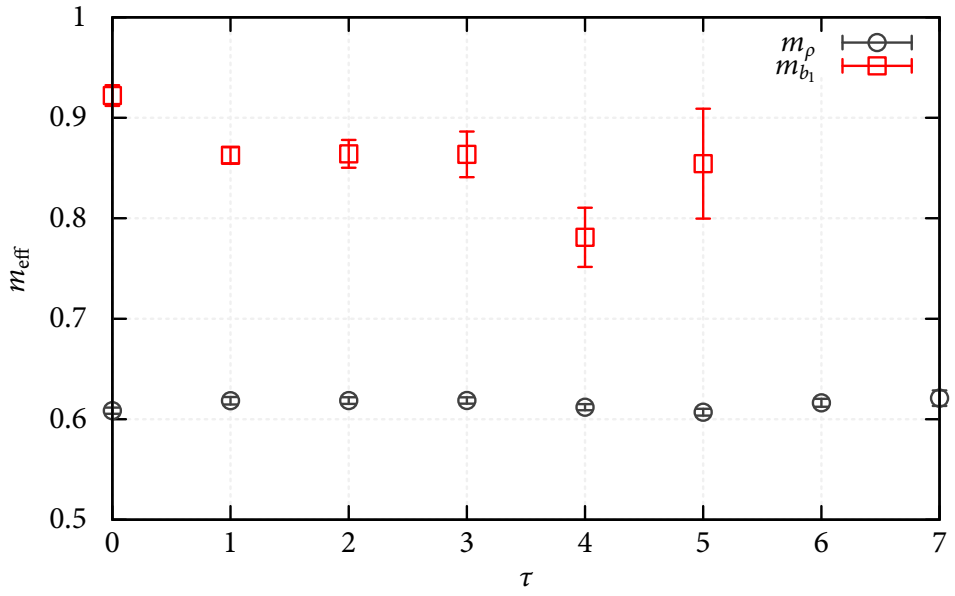

Figure 4.7: Rho and b_1 effective mass plot at $\beta = 0.58$, $m_q = 0.015$ and a lattice size of $32^3 \times 32$, for eight flavors. Results at large τ with huge error bars are not plotted here.

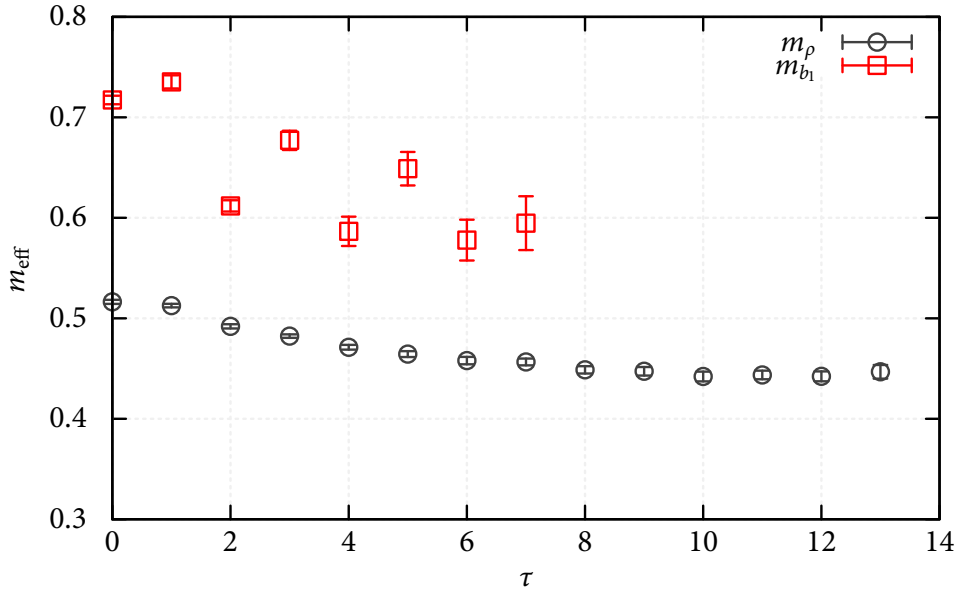

Figure 4.8: Rho and b_1 effective mass plot at $\beta = 0.49$, $m_q = 0.01$ and a lattice size of $32^3 \times 32$, for twelve flavors. Results at large τ with huge error bars are not plotted here.

β	0.008	0.01	0.015	0.016	0.02	0.024	0.025	0.03
0.54		1			1			1
0.56	5			3		3		
0.58			5				3	

Table 4.5: t_{min} for double states spectrum fit with eight flavors

β	0.01	0.015	0.0175	0.02	0.025	0.03
0.45	1			1		1
0.46	1			1		1
0.47	5	1	1	1	1	1
0.475	5			1		1
0.48	5			3		1
0.49	5			3		3
0.50	5			5		3

Table 4.6: t_{min} for double states spectrum fit with twelve flavors

Figure 4.5 and 4.6 show the Pion effective mass obtained from solving the non-oscillating part (the first row) of equation (3.52) with the values of the propagator at $t = \tau$ and $t = \tau + 1$. They show very good and long plateaus, indicating good signals. However, in the case of the rho propagators, the oscillating state, b_1, can be hardly seen directly from the propagators by eye, which implies the extraction of b_1 mass is hard. And the rho and b_1 effective masses obtained from solving (3.52) with the values of propagator from $t = \tau \sim \tau + 3$ are shown in figure 4.7 and 4.8. It can be seen that the effective masses of b_1 hardly reaches any plateau before the signal disappears into the noise and data is not shown in the figure for large τ values. Other meson states are similar to rho and b_1, in the sense that the oscillating states in the staggered meson propagators can be very noisy at large temporal separations, and might not reach a pleasant plateau to the eyes. Therefore, the fitting range needs to be carefully chosen and systematic errors are introduced to the measurements, which are laid out in the following paragraphs.

Selected meson masses are listed in table 4.7 and 4.9 for eight and twelve flavors,

β	m_q	Size	f_π	m_π	m_{π_2}	m_ρ
0.54	0.01	$16^3\times32$	0.1595(10)	0.28833(17)	0.762[42]	0.944[26]*
		$24^3\times32$	0.1592(12)	0.28897(19)	0.774[22]	0.969[18]
	0.02	$16^3\times32$	0.1923(12)	0.38945(13)	0.964[22]	1.107[34]*
	0.03	$16^3\times32$	0.21539(97)	0.46427(10)	1.0948(95)	$1.260(13)_2$
0.56	0.008	$16^3\times32$	0.0915(12)	0.27448(98)	0.480[26]	$0.619(13)_4$
		$24^3\times32$	0.0898(14)	0.27276(69)	0.4605(81)	0.6002(67)
	0.016	$16^3\times32$	0.1250(12)	0.37046(43)	0.6335(68)	0.7929(60)
		$24^3\times32$	0.12230(96)	0.37218(26)	0.6434(51)	0.8031[43]
	0.024	$16^3\times32$	0.14821(87)	0.44154(27)	0.7873(61)	$0.9466(51)_2$
		$24^3\times32$	0.1480(14)	0.44168(18)	0.7938(72)	0.9577[47]
0.58	0.015	$16^3\times32$	0.0866(12)	0.3531(10)	0.4718(65)	0.6111(65)
		$24^3\times32$	0.0899(13)	0.35237(79)	0.4750[51]	0.6131(37)
		$32^3\times32$	0.09094(92)	0.35232(42)	0.4741(46)	0.6080(48)
	0.025	$16^3\times32$	0.1179(23)	0.44921(78)	0.6316(35)	0.7732[50]
		$24^3\times32$	0.1187(11)	0.44926[28]	0.6296[46]	0.7787(26)

Table 4.7: Meson masses and f_π for eight flavors. Inflated errors are indicated by dark red brackets. Changed t_{min}'s are indicated by subscripts beside the errors. The tag * is used to show the fitted $\chi^2/\text{dof} > 3$. Please see text for detailed explanations.

β	m_q	Size	m_σ	m_{b_1}	m_{ρ_2}	m_{a_1}
0.54	0.01	$16^3\times32$	0.754[22]	0.93[66]*	0.995[16]	1.131[80]
		$24^3\times32$	0.827(24)	1.04[37]	1.014[25]	1.24[11]
	0.02	$16^3\times32$	1.000(37)	0.9[1.3]*	1.191[13]	1.220[86]
	0.03	$16^3\times32$	1.127(64)	$3[18]_2$	$1.261[16]^\star_0$	$1.89[25]^\star_0$
0.56	0.008	$16^3\times32$	0.480(21)	$0.98[14]_4$	0.629(23)	0.777(88)
		$24^3\times32$	0.552(12)	1.13(21)	0.5998(56)	0.872(57)
	0.016	$16^3\times32$	0.683(16)	0.863(70)	0.8171(89)	1.035(48)
		$24^3\times32$	0.732(10)	1.09[17]	0.8203(44)	1.044(19)
	0.024	$16^3\times32$	0.845(21)	$1.98[46]_2$	0.9849(58)	1.112(56)
		$24^3\times32$	0.870(17)	1.18[23]	0.9865[88]	1.280[70]
0.58	0.015	$16^3\times32$	0.578(13)	0.728(83)	0.6105(55)	0.749(32)
		$24^3\times32$	0.6005(59)	0.840(56)	0.6192(45)	0.845(22)
		$32^3\times32$	0.6050(59)	0.900(69)	0.6139(57)	0.842(35)
	0.025	$16^3\times32$	0.731(17)	0.98[33]	0.7848(57)	0.946(39)
		$24^3\times32$	0.7537(58)	0.96[10]	0.7890[28]	1.014[20]

Table 4.8: Continuation of table 4.7.

β	m_q	Size	f_π	m_π	m_{π_2}	m_ρ
0.45	0.01	$16^3\times32$	0.2784(24)	0.25341(15)	1.46[13]$_0$	
	0.02	$16^3\times32$	0.2864(19)	0.35352(13)	1.529[92]$_0$	
	0.03	$16^3\times32$	0.2950(17)	0.42888(12)		
0.46	0.01	$16^3\times32$	0.2361(19)	0.26343(20)	1.18(11)	
	0.02	$16^3\times32$	0.2674(23)	0.36123(19)	1.353(44)	
	0.03	$16^3\times32$	0.2815(15)	0.435917(88)		
0.47	0.01	$16^3\times32$	0.1088(11)	0.31551(93)	0.557(14)	0.659(15)
		$24^3\times32$	0.1105(21)	0.31475(47)	0.579(16)	0.706(11)
		$32^3\times32$	0.1091(16)	0.31463(35)	0.547[24]	0.6799(63)
	0.015	$16^3\times32$	0.1743(15)	0.34795(35)	0.879[32]	1.000[12]
	0.0175	$16^3\times32$	0.2081(15)	0.35985(20)	1.039[46]	1.146(11)$_0$
	0.02	$16^3\times32$	0.2190(19)	0.37676(19)	1.102[86]	1.194(16)$_0$
		$24^3\times32$	0.2279(19)	0.37703(11)	1.130(22)	1.2125(83)$^*_0$
	0.025	$16^3\times32$	0.2411(21)	0.41258(20)	1.255(80)	
	0.03	$16^3\times32$	0.2557(20)	0.44652(15)	1.298[39]$_0$	
0.475	0.01	$16^3\times32$	0.0965(12)	0.3170(14)	0.549[18]	0.623(16)
		$24^3\times32$	0.0965(17)	0.31694(68)	0.4869[81]	0.5839(46)
	0.02	$16^3\times32$	0.1789(12)	0.39842(24)	0.892[26]	1.024[20]*
	0.03	$16^3\times32$	0.2391(19)	0.45459(11)	1.198(26)	
0.48	0.01	$16^3\times32$	0.0836(12)	0.3189(15)	0.4416(99)	0.5369(87)
		$24^3\times32$	0.08433(65)	0.31215(39)	0.4350[40]	0.5247(44)
		$32^3\times32$	0.08451(97)	0.31448(60)	0.4453(49)	0.5309(33)
	0.02	$16^3\times32$	0.14487(92)	0.41495(41)	0.752[14]	0.8796[72]
		$24^3\times32$	0.1453(23)	0.41508(30)	0.761[11]	0.8938(50)
	0.03	$16^3\times32$	0.2127(16)	0.46671(17)	1.084[34]	1.1662(84)$^*_0$
0.49	0.01	$16^3\times32$	0.06756(98)	0.3262(33)	0.4152(95)	0.5230(62)
		$32^3\times32$	0.07037(64)	0.30445(70)	0.3706[33]	0.4547(29)
	0.02	$16^3\times32$	0.1176(15)	0.42140(71)	0.6029[95]	0.7211[50]*
	0.03	$16^3\times32$	0.1584(19)	0.49365(33)	0.852(14)	0.9900(93)
0.50	0.01	$16^3\times32$	0.05471(52)	0.3533(27)	0.411[20]	0.5236(50)
	0.02	$16^3\times32$	0.10039(84)	0.4159(14)	0.5547(56)	0.6377(37)
	0.03	$16^3\times32$	0.1365(11)	0.49788(59)	0.711[13]	0.8265(38)

Table 4.9: Meson masses for twelve flavors. Inflated errors are indicated by dark red brackets. Changed t_{min}'s are indicated by subscripts beside the errors. The tag * to show the fitted $\chi^2/\text{dof} > 3$. Please see text for detailed explanations.

β	m_q	Size	m_σ	m_{b_1}	m_{ρ_2}	m_{a_1}
0.45	0.01	$16^3\times32$	$1.16(45)_0$		$1.526(22)_0$	$2.20(42)_0$
	0.02	$16^3\times32$	$1.20[44]_0$			
	0.03	$16^3\times32$				
0.46	0.01	$16^3\times32$	0.95(28)		$1.354[30]_0$	$1.98[41]_0$
	0.02	$16^3\times32$	0.542(78)		$1.421(12)_0$	$1.77[19]_0$
	0.03	$16^3\times32$			$1.519(16)_0$	$2.39[56]_0$
0.47	0.01	$16^3\times32$	0.570(16)	0.86(25)	0.693(16)	0.85(13)
		$24^3\times32$	0.556(14)	0.69(11)	0.659(16)	1.00(14)
		$32^3\times32$	0.588(11)	1.08(14)	0.678(12)	0.898(77)
	0.015	$16^3\times32$	0.834(32)	1.10[33]	1.064[29]	1.18[16]
	0.0175	$16^3\times32$	0.989(54)	$3.3[1.2]_0$	1.258(13)	1.356(85)
	0.02	$16^3\times32$	1.21[20]	$3.2[1.3]_0$	1.288(19)	1.66(27)
		$24^3\times32$	1.098(41)	$2.68[69]^*_0$	1.331(15)	1.522(71)
	0.025	$16^3\times32$	0.84(23)		$1.380[13]_0$	$2.00[25]_0$
	0.03	$16^3\times32$	$1.14[17]_0$		1.447(23)	1.56(40)
0.475	0.01	$16^3\times32$	0.487(12)	0.81(16)	0.620(10)	0.771(73)
		$24^3\times32$	0.5207(44)	0.966(90)	0.5899(58)	0.806(27)
	0.02	$16^3\times32$	0.876[22]	$0.92[58]^*$	1.090[20]	1.22[12]
	0.03	$16^3\times32$	1.092(94)		1.387[12]	1.35(16)
0.48	0.01	$16^3\times32$	0.4485(51)	0.639(44)	0.541(11)	0.621(25)
		$24^3\times32$	0.4753(46)	0.782(56)	0.5240(40)	0.723(24)
		$32^3\times32$	0.4792(36)	0.698[32]	0.5320(33)	0.685(18)
	0.02	$16^3\times32$	0.793(14)	0.95[95]	0.9021(72)	1.142[56]
		$24^3\times32$	0.786(11)	0.969[84]	0.9101(59)	1.187(55)
	0.03	$16^3\times32$	1.070[58]	$3.9[1.5]^*_0$	1.253[12]	1.50[15]
0.49	0.01	$16^3\times32$	0.4176(29)	0.664(27)	0.5309(80)	0.609(16)
		$32^3\times32$	0.4327(26)	0.582[43]	0.4567(34)	0.5788[92]
	0.02	$16^3\times32$	0.6481(86)	$0.77[27]^*$	0.7208(47)	0.867(26)
	0.03	$16^3\times32$	0.863(33)	0.89[45]	1.001(12)	1.19(11)
0.50	0.01	$16^3\times32$	0.3860(26)	0.588(10)	0.5345(53)	0.5554(64)
	0.02	$16^3\times32$	0.6001(72)	0.796(50)	0.6523(58)	0.762(19)
	0.03	$16^3\times32$	0.780(17)	0.93[20]	0.8428[52]	0.996[43]

Table 4.10: Continuation of table 4.9.

respectively. WALL2Z sources with the box size of 16^3 are used in all the meson mass measurements for their better signal, except for f_π, which needs a point source. The maximum temporal separation, $t_{\max}$, used to fit the propagator, is always chosen to be $N_\tau/2$, which is 16 for zero temperature studies, because the propagators are folded, $C(t) = \big(C(0,t) + C(0,N_\tau - t)\big)/2$. Table 4.5 and 4.6 shows the minimum temporal separations, $t_{\min}$, for the staggered meson propagators containing two states (3.52), including the π_2, σ, ρ, ρ_2, a_1 and b_1, of staggered fermion. For single states fit, which are done to determine f_π and m_π using the first part of equation (3.52), and are much more stable than the double states fits, $t_{\min}^{\text{single}}$ is chosen to be $t_{\min}^{\text{double}} + 4$. Different $t_{\min}$ have been used for different ensembles, because the parameter space in this thesis covers a large range of lattice scales, which can be seen from the values of m_ρ. The values of $t_{\min}$ are chosen after closely examining the effective mass plot for each meson channel. The resulting $t_{\min}$ values of 1, 3 and 5 correspond to the m_{ρ_2} values of $1 < m_{\rho_2}$, $0.7 < m_{\rho_2} < 1$ and $m_{\rho_2} < 0.7$, respectively. For coarser lattices, the minimum fitting range is smaller. The errors quoted in table 4.7 4.8 and 4.9 4.10 consist of statistical errors from the Jackknife procedures and the systematic errors, which are explained as following. Fitted values from $t_{\min}$ and $t_{\min} + 1$ are compared against each other, and if $|m(t_{\min}) - m(t_{\min}+1)|$ is larger than twice the statistical error at $t_{\min}$ estimated by Jackknife procedure, the statistical error is inflated such that $|m(t_{\min}) - m(t_{\min}+1)|$ is twice the inflated error. Otherwise, the statistical error is left as is, since the systematics can be seen as included within the statistical error. Thus, the deviation always satisfies $\Delta_{\text{fit}}^{\text{spect}} \leq 2$, where

$$\Delta_{\text{fit}}^{\text{spect}} = \frac{|m(t_{\min}) - m(t_{\min}+1)|}{\text{Err}[m](t_{\min})}. \tag{4.1}$$

And in table 4.7 4.7 and 4.9 4.10, such inflated errors are enclosed by dark red bracket

instead of the normal parenthesis. Among all the measurements, there are some of the channels where the fits fail to converge at certain t_{min}, and then following procedure is used. If the fit fails to converge at t_{min} but not $t_{\text{min}} + 1$, the value from $t_{\text{min}} + 1$ is quoted and the systematic check against $t_{\text{min}} + 2$ is performed. If the fit also fails to converge at $t_{\text{min}} + 2$, or the fit fails to converge at $t_{\text{min}} + 1$ but not at t_{min}, the value from $t_{\text{min}} - 1$ is quoted and the systematic error check against t_{min} is performed. If all the above fails to give convergent results, it is conceivable that the value is not measured accurately enough, and thus we leave certain table cells blank. The subscripts beside the errors Tables 4.7 4.7 and 4.9 4.10 indicate the t_{min} used after the above workaround. There are a few cases where the fitted $\chi^2/\text{dof} > 3$, and the tag * is used to indicate those values with such large χ^2dof in the tables. Figure 4.9 and 4.10 show scatter plots of χ^2/dof and resulting $\Delta_{\text{fit}}^{\text{spect}}$ with an overlay of the histogram of the χ^2/dof, for single state propagators and double state propagators respectively.

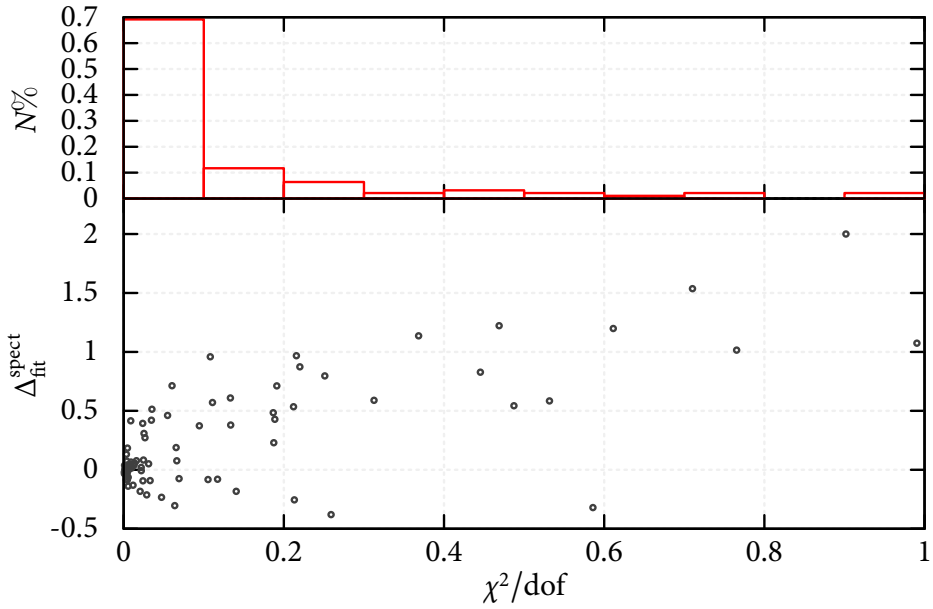

Figure 4.9: χ^2/dof versus Δ_{fit} for single state propagators, m_π and f_π.

m_{valence}	f_π	m_π	m_{π_2}	m_ρ
0.02	0.09690(73)	0.41450(46)	0.5078[35]	0.5722(22)
0.03	0.11674(83)	0.49560[41]	0.6128[26]	0.6657(20)

Table 4.11: Twelve flavors valence spectrum measured on $\beta = 0.49$, $m_{\text{sea}} = 0.01$, $32^3 \times 32$ ensemble.

m_{valence}	m_σ	m_{b_1}	m_{ρ_2}	m_{a_1}
0.02	0.5549(27)	0.701[35]	0.5749(23)	0.6992(95)
0.03	0.6499(31)	0.787(23)	0.6698(20)	0.795(12)

Table 4.12: Continuation of table 4.12.

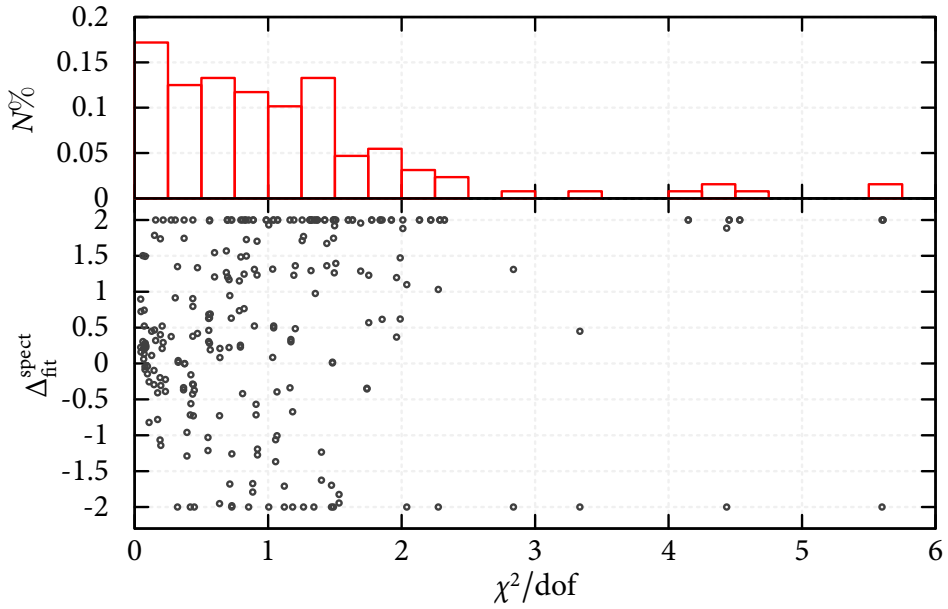

Figure 4.10: χ^2/dof versus Δ_{fit} for double states propagators.

4.3 Partially Quenched Meson Masses with Twelve Flavors

Partially quenched spectra are studied for one of the twelve-flavor ensembles. The ensemble with twelve flavors at $\beta = 0.49$, $m_q = 0.01$ and the lattice size of $32^3 \times 32$ was used, and the partially quenched spectra with $m_{\text{valence}} = 0.02$ and 0.03 have been measured. The

results are listed in table 4.11 4.12, where the inflated errors using the aforementioned scheme are labeled with dark red brackets. Except for m_π, the differences between the full dynamical results ($m_q = 0.02$ and 0.03, $16^3 \times 32$) and the partially quenched results ($m_{\text{sea}} = 0.01$, $m_{\text{valence}} = 0.02$ and 0.03) are huge, compared to normal 2+1 flavors QCD simulations.

These are lattices with rather heavy pions ($m_\pi L \gtrsim 6$), so finite volume effects are not expected to be large. However, for all particle except the pion, partial quenching changes mass by a large amount, and hence partial quenching for twelve flavors is not at all reliable. For this reason, we have not done any further partially quenched simulations. More detailed understanding of how partial quenching affects the system needs further investigations.

4.4 Quark Potential

The two-step fits we have done for heavy quark potential are described in section 3.3.5 and are done with the double Jackknife method to estimates the statistical error. Table 4.13 and 4.14 shows the string tension σ, as well as r_0 and a^{-1}, along with both the temporal and spatial fit range. a^{-1} in the table are determined from the assumption that the physical r_0 is 0.5fm. The maximum temporal separation, t_{max}, is fixed to be 9, which is the largest value measured. The minimum spatial separation, r_{min} is fixed to be $\sqrt{2}$, because for $r \gtrsim \sqrt{2}$, the fitted results hardly change for a short range of r. It is also numerically hard to go to larger r_{min}, because the signal of $1/r$ in the form of the potential will be lost. Theoretically, one needs to go to sufficiently large t to get the quark potential $V(r)$ from equation (3.64). But numerically, there is a limit beyond which the noise will dominate. The value t_{min} is chosen, such that if t_{min} is further increased, the fitted

β	m_q	Size	t	r	σ	r_0	a^{-1}/GeV
0.54	0.01	$16^3\times32$	3 ~ 9	$\sqrt{2}$ ~ 6	0.1523[54]	2.793[30]	1.102[12]
		$24^3\times32$	3 ~ 9	$\sqrt{2}$ ~ 6	0.1531(32)	2.800[22]	1.1050[88]
	0.02	$16^3\times32$	3 ~ 9	$\sqrt{2}$ ~ 6	0.2155[66]	2.350(15)	0.9275(61)
	0.03	$16^3\times32$	3 ~ 9	$\sqrt{2}$ ~ 6	0.2569{93}	2.126{12}	0.8391{46}
0.56	0.008	$24^3\times32$	5 ~ 9	$\sqrt{2}$ ~ 8	0.0454(22)	5.02(10)	1.982(41)
	0.016	$16^3\times32$	4 ~ 9	$\sqrt{2}$ ~ 6	0.0828[58]	3.79[11]	1.497[42]
		$24^3\times32$	4 ~ 9	$\sqrt{2}$ ~ 6	0.0824(14)	3.787(24)	1.4945(94)
	0.024	$16^3\times32$	4 ~ 9	$\sqrt{2}$ ~ 6	0.1239[62]	3.146[68]	1.242[27]
		$24^3\times32$	4 ~ 9	$\sqrt{2}$ ~ 6	0.1229(33)	3.149(27)	1.243(11)
0.58	0.015	$16^3\times32$	5 ~ 9	$\sqrt{2}$ ~ 8	0.0425[74]	5.23[51]	2.07[20]
		$24^3\times32$	5 ~ 9	$\sqrt{2}$ ~ 8	0.0439(19)	5.179(92)	2.044(36)
		$32^3\times32$	5 ~ 9	$\sqrt{2}$ ~ 8	0.0438(16)	5.195(80)	2.050(32)
	0.025	$16^3\times32$	5 ~ 9	$\sqrt{2}$ ~ 8	0.0646(64)	4.27(16)	1.687(63)
		$24^3\times32$	5 ~ 9	$\sqrt{2}$ ~ 8	0.0677[36]	4.195[86]	1.656[34]

Table 4.13: Static quark potential measurements with eight flavors.

results will not change too much relative to the error, and r_{max} is chosen as large as possible without losing the signal. The errors quoted in table 4.13 and 4.14 also include the systematic error. Here, a similar approach has been employed as for the meson spectra. The fitted results of r_0 from t_{min}, r_{max} and the ones from $t_{\text{min}}+1$, $r_{\text{max}}-1$ are compared. If the difference between the two is larger than 2σ, the statistical error bars are inflated to keep the difference at $2\sigma_{\text{inflated}}$. Thus, the deviation always satisfies $\Delta_{\text{fit}}^{\text{potential}} \leq 2$, where

$$\Delta_{\text{fit}}^{\text{potential}} = \frac{|x(t_{\text{min}}, r_{\text{max}}) - x(t_{\text{min}}+1, r_{\text{max}}-1)|}{\text{Err}[x](t_{\text{min}}, r_{\text{max}})}\,. \tag{4.2}$$

Those errors quoted in dark red bracket are inflated error bars. If the fit fails to converge at $t_{\text{min}}+1$ and $r_{\text{max}}-1$, the original statistical errors are quoted and enclosed in purple curly braces. In the configurations with strong couplings and large masses, the fits to $V(r)$ for Cornell potential form give quite large values of χ^2/dof. And those that have

β	m_f	Size	t	r	σ	r_0	a^{-1}/GeV
0.45	0.01	$16^3\times32$	2 ~ 9	$\sqrt{2}$ ~ 4	0.45[15]*	1.616[63]*	0.638[25]*
	0.02	$16^3\times32$	2 ~ 9	$\sqrt{2}$ ~ 4	0.40[18]*	1.444(88)*	0.570(35)*
	0.03	$16^3\times32$					
0.46	0.01	$16^3\times32$	2 ~ 9	$\sqrt{2}$ ~ 4	0.332[33]*	1.932[29]*	0.762[11]*
	0.02	$16^3\times32$	2 ~ 9	$\sqrt{2}$ ~ 4	0.478(27)*	1.720[23]*	0.6789[91]*
	0.03	$16^3\times32$	2 ~ 9	$\sqrt{2}$ ~ 4	0.472[90]*	1.571[53]*	0.620[21]*
0.47	0.01	$16^3\times32$	5 ~ 9	$\sqrt{2}$ ~ 8	0.0447(42)	5.21(21)	2.056(83)
		$24^3\times32$	5 ~ 9	$\sqrt{2}$ ~ 8	0.0322[86]	6.00[52]	2.37[21]
		$32^3\times32$	5 ~ 9	$\sqrt{2}$ ~ 8	0.0436(30)	5.26(14)	2.076(57)
	0.015	$16^3\times32$	3 ~ 9	$\sqrt{2}$ ~ 6	0.1489(73)	2.910(42)	1.148(17)
	0.0175	$16^3\times32$	3 ~ 9	$\sqrt{2}$ ~ 6	0.228{10}*	2.366{20}*	0.9338{77}*
	0.02	$16^3\times32$	2 ~ 9	$\sqrt{2}$ ~ 4	0.286(11)*	2.098(11)*	0.8281(43)*
		$24^3\times32$	2 ~ 9	$\sqrt{2}$ ~ 4	0.290[17]*	2.123[24]*	0.8377[96]*
	0.025	$16^3\times32$	2 ~ 9	$\sqrt{2}$ ~ 4	0.325[28]*	1.931[27]*	0.762[11]*
	0.03	$16^3\times32$	2 ~ 9	$\sqrt{2}$ ~ 4	0.370[35]*	1.805[26]*	0.712[10]*
0.475	0.01	$16^3\times32$	5 ~ 9	$\sqrt{2}$ ~ 8	0.036[19]	5.85[61]	2.31[24]
		$24^3\times32$	5 ~ 9	$\sqrt{2}$ ~ 8	0.0334(19)	6.05(14)	2.386(56)
	0.02	$16^3\times32$	4 ~ 9	$\sqrt{2}$ ~ 6	0.122[24]	3.03[28]	1.20[11]
	0.03	$16^3\times32$	2 ~ 9	$\sqrt{2}$ ~ 4	0.311[17]*	2.014(10)*	0.7947(41)*
0.48	0.01	$16^3\times32$	5 ~ 9	$\sqrt{2}$ ~ 8	0.0225(39)	7.31(55)	2.89(22)
		$24^3\times32$	5 ~ 9	$\sqrt{2}$ ~ 8	0.0202[15]	7.66[29]	3.02[11]
		$32^3\times32$	5 ~ 9	$\sqrt{2}$ ~ 8	0.0212(15)	7.49(24)	2.957(95)
	0.02	$16^3\times32$	4 ~ 9	$\sqrt{2}$ ~ 6	0.0808[47]	3.892[97]	1.536[38]
		$24^3\times32$	4 ~ 9	$\sqrt{2}$ ~ 6	0.0818(27)*	3.862(43)*	1.524(17)*
	0.03	$16^3\times32$	3 ~ 9	$\sqrt{2}$ ~ 6	0.226(13)	2.365[34]	0.933[13]
0.49	0.01	$16^3\times32$	6 ~ 9	$\sqrt{2}$ ~ 9	0.0153[94]	8.8(1.4)	3.48(56)
		$32^3\times32$	6 ~ 9	$\sqrt{2}$ ~ 9	0.0141[12]	9.24[35]	3.65[14]
	0.02	$16^3\times32$	5 ~ 9	$\sqrt{2}$ ~ 8	0.0448[76]	5.27[56]	2.08[22]
	0.03	$16^3\times32$	4 ~ 9	$\sqrt{2}$ ~ 6	0.1005(86)	3.48(10)	1.375(40)
0.50	0.01	$16^3\times32$	6 ~ 9	$\sqrt{2}$ ~ 9	0.0090(42)	11.5(2.7)	4.5(1.1)
	0.02	$16^3\times32$	5 ~ 9	$\sqrt{2}$ ~ 8	0.0380(24)	5.72(15)	2.258(60)
	0.03	$16^3\times32$	4 ~ 9	$\sqrt{2}$ ~ 6	0.0701(40)	4.242(91)	1.674(36)

Table 4.14: Static quark potential measurements with twelve flavors.

$\chi^2/\mathrm{dof} > 3$ are indicated by * in the table. The reason that they have large χ^2/dof is quite likely because the potential at strong couplings and large masses cannot be described by the Cornell potential very well. Figure 4.11 shows χ^2/dof of the Cornell potential fit versus $\Delta_{\mathrm{fit}}^{\mathrm{potential}}$ of the string tension with an overlay of a histogram of the χ^2/dof.

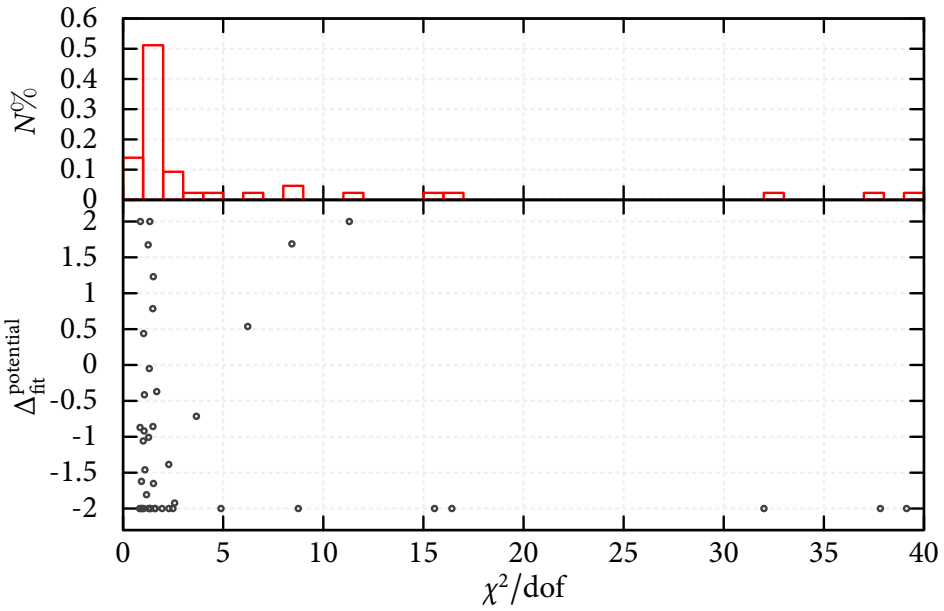

Figure 4.11: χ^2/dof versus $\Delta_{\mathrm{fit}}^{\mathrm{potential}}$ of the string tension. Those points that have $\chi^2/\mathrm{dof} > 3$ are from strong coupling and large m_q with twelve flavors, and labeled with * in table 4.14.

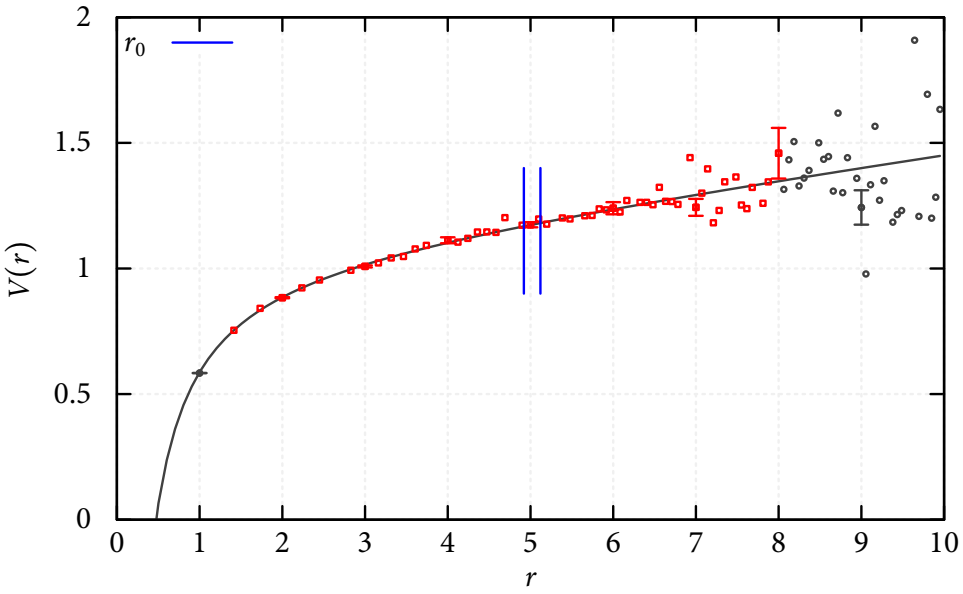

Figure 4.12: Quark potential with eight flavors at $\beta = 0.56$ and $m_q = 0.008$ with a lattice size of $24^3 \times 32$. To avoid cluttering, representative error bars of $V(r)$ are only shown at each integer r point.

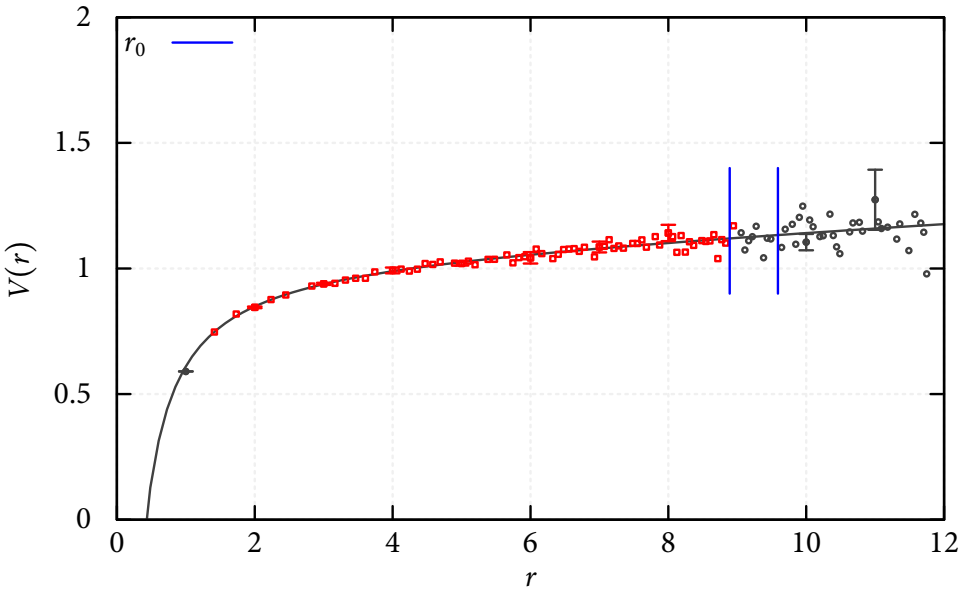

Figure 4.13: Quark potential with twelve flavors at $\beta = 0.49$ and $m_q = 0.01$ with a lattice size of $32^3 \times 32$. To avoid cluttering, representative error bars of $V(r)$ are only shown at each integer r point.

Figures 4.12 and 4.13 show typical fits to the Cornell potential form (equation (3.65)) for the measured potential for eight flavors and twelve flavors respectively. It can be seen that for weak coupling and small masses, the potential measured in this thesis can be described by Cornell potential very well, and the linear rising piece of the potential can be seen clearly.

4.5 Finite Volume Effect

The results on different lattice sizes with eight flavors show mild volume dependence, while results with twelve flavors show larger volume dependence for the weaker coupling ensembles.

With eight flavors, comparing the results in the Table 4.2, 4.7 and 4.8 for lattice en-

semble of sizes $32^3\times32$ and $24^3\times32$ at $\beta = 0.58$ and $24^3\times32$ and $16^3\times32$ at other 2 β values, it is evidently that the finite volume effect is saturated.

With twelve flavors, looking at the Table 4.4, 4.9 and 4.10, at $\beta \leq 0.48$, finite volume effects are under control with the largest volumes for each lattice ensembles. At $\beta = 0.49$ and $m_q = 0.01$, there are not enough comparisons to assert that the volume used is large enough, yet comparing $16^3\times32$ and $32^3\times32$ show that the finite volume effects are within 5 σ levels for most of the observables, but m_ρ and m_{ρ_2} show around 10 σ deviation from $16^3\times 32$ to $32^3\times 32$ at $m_q = 0.01$. However, the finite volume effect at this coupling but larger m_q is very mild from partially quenched studies in section 4.3. Nevertheless, at $\beta = 0.50$, no measure of finite volume effect is done. And from the degeneracy of m_ρ and m_{a_1} which will be discussed in section 4.6.2, or even from the direct measurement of m_ρ ($m_\rho(\beta = 0.50, m_q = 0.01) > m_\rho(\beta = 0.49, m_q = 0.01)$), it can be inferred that the finite volume effect at this weak coupling is very large at $\beta = 0.50$ and $m_q = 0.01$. One can estimate the lower bound of the finite volume effect at $\beta = 0.50$ from comparing $16^3\times32$ and $32^3\times32$ at $\beta = 0.49$, but more trustworthy determination of the finite size effect needs much more simulations. Nevertheless, we find the masses of the ρ and a_1 are indeed well separated from the lattice ensemble with the size of $32^3\times32$ at $\beta = 0.49$. Degeneracy of parity partners, such as the ρ and a_1 is an indicator of finite volume effects and since we do not find degeneracy, this argues that we are not seeing large finite volume effects for this ensemble.

It is very important to keep in mind the effects of finite volume on the results presented here as we discuss the phases of the systems we have studied.

4.6 Phases at the Chiral Limit

4.6.1 Linear Extrapolations Versus Chiral Perturbation

Throughout this thesis, simple linear analytic extrapolations to the massless quark limit, $m_q = 0$, will be used. For QCD-like theories in the chirally broken phase, there will be chiral logarithms in such an extrapolation. *A priori* one does not have any understanding of the quark mass range over which chiral logs might be seen, since this requires knowing the size of the decay constant and the chiral condensate at the chiral limit. The equation (1.12) can be rewritten to depend explicitly on quark mass m_q as

$$\begin{aligned} M_\pi^2 &= 2Bm_q\Big\{1 + \xi m_q \frac{1}{N_f}\log\big(\frac{\xi m_q}{\Lambda_M}\big)\Big\}, \\ F_\pi &= F\Big\{1 - \xi m_q \frac{N_f}{2}\log\big(\frac{\xi m_q}{\Lambda_F}\big)\Big\}, \\ \langle\bar{\psi}\psi\rangle &= F^2B\Big\{1 - \xi m_q \frac{N_f^2-1}{N_f}\log\big(\frac{\xi m_q}{\Lambda_C}\big)\Big\}, \end{aligned} \tag{4.3}$$

where $\xi = \frac{2B}{(4\pi F)^2}$, and the sign difference in $\langle\bar{\psi}\psi\rangle$ is due to different normalization.

Equation (4.3) shows the continuum chiral perturbation series up to the next-to-leading order. There are explicit factors of N_f multiplying chiral logarithms, and the expansion coefficients depend on N_f implicitly. Thus the quark mass range where chiral logarithms are important is unknown. Simply plugging in the numbers in the simulations at weak couplings reveals that $\xi \sim 10$ for eight flavors and ~ 50 for twelve flavors, due to the small values of f_π we have measured, which means that the above expansion series is totally invalid for the mass range ($m_q \sim 0.01$) we have simulated. Nevertheless, chiral perturbation theory is expected to be a better description at strong couplings, where we can achieve lighter pions, relative to f_π. Figure 4.14 and figure 4.15 shows the

fits of the continuum next-to-leading order chiral perturbation form (4.3) to eight-flavor at $\beta = 0.54$ and twelve-flavor at $\beta = 0.45$, respectively. In the figures, the values of $\langle\bar{\psi}\psi\rangle$ are normalized such that it represents the chiral condensate per fermion flavor and it is summed over three colors, as described in section 1.1.2. This normalization introduces a factor of $\frac{3}{4}$ to the values measured with CPS and quoted in this thesis (described in section 3.3.4. It can be seen that both $\langle\bar{\psi}\psi\rangle$ and f_π follows the next-to-leading order chiral perturbation description, while m_π is slightly off. This is expected, since there are not exactly $N_f^2 - 1$ Goldstone pions due to the staggered fermion flavor symmetry breaking, and thus the continuum chiral perturbation theory describes the mass of the pions poorly.

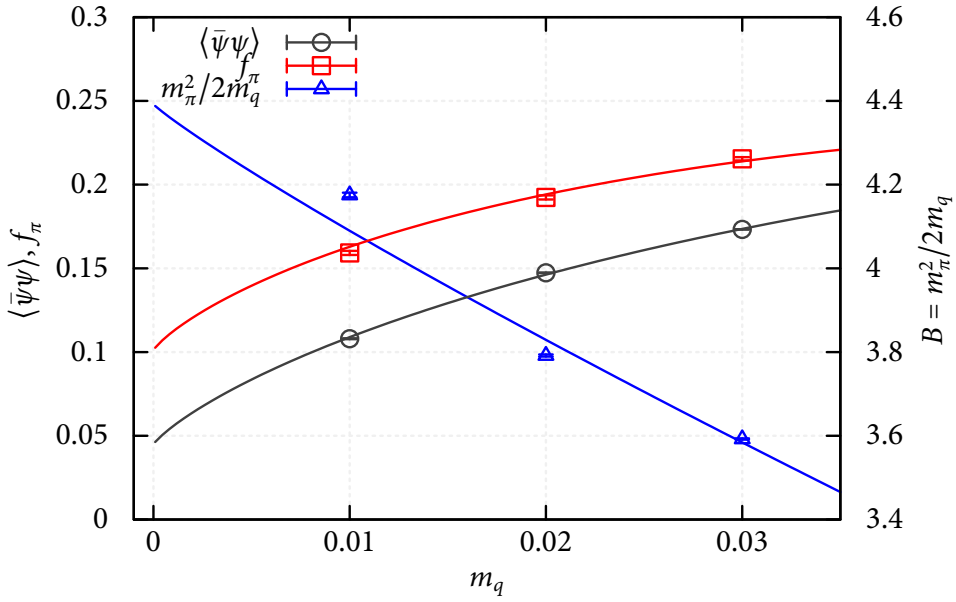

Figure 4.14: Next-to-leading order chiral perturbation fit to eight-flavor ensembles at $\beta = 0.54$. $\langle\bar{\psi}\psi\rangle$ is normalized to be the average per flavor and sum of colors.

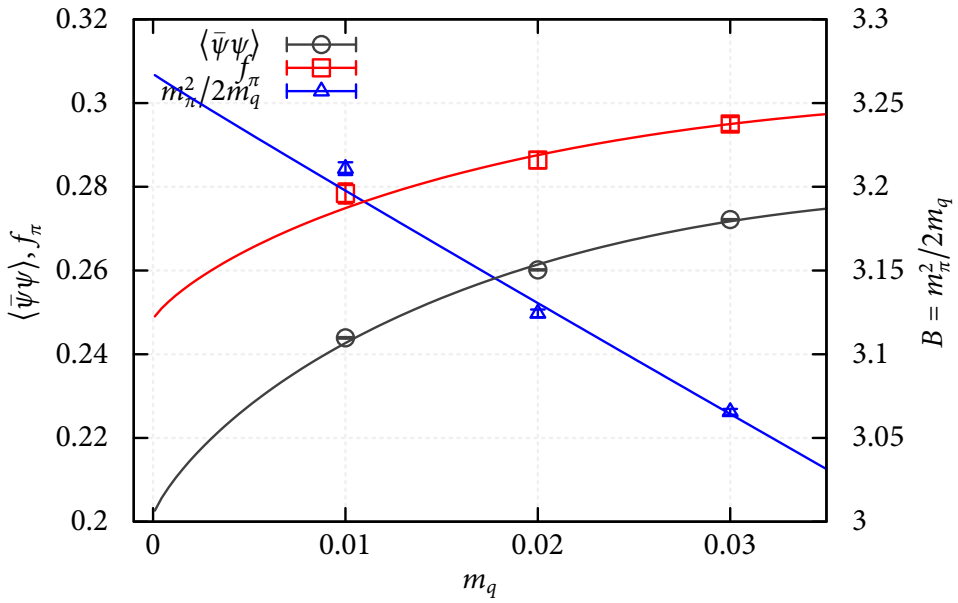

Figure 4.15: Next-to-leading order chiral perturbation fit to twelve-flavor ensembles at $\beta = 0.45$. $\langle\bar{\psi}\psi\rangle$ is normalized to be the average per flavor and sum of colors.

Compared to linear extrapolations described in the next section 4.6.2, values in the chiral limit from the chiral perturbation extrapolations are off by 10% to 20%. This is small and does not impose any qualitative changes of any hadronic observables in the chiral limit, which is also true for smaller number of flavors. In 2 + 1 flavor QCD, where much work has been done on this topic, simple linear extrapolations are rather accurate [71], and higher order chiral perturbation expansion is still unstable for current state of the art simulations. Admittedly, the extrapolation to the chiral limit is needed to study the theory with massless quarks in this work, while in 2 + 1 flavor QCD, one only needs the extrapolation to the physical quark mass.

On the other hand, if there were conformal symmetry in the system, the explicit input quark mass not only breaks chiral symmetry explicitly, it also breaks conformal symmetry explicitly. In addition, the conformal symmetry is also explicitly broken by

β	0.54	0.56	0.58
$\langle\bar{\psi}\psi\rangle$	0.10879(45)	0.02571(21)	0.01519(21)
f_π	0.1332(18)	0.0624(21)	0.0493(29)
m_π^2	0.01842(60)	0.0189(16)	0.0076(49)
m_{π_2}	0.629(19)	0.305(12)	0.241(12)
m_σ	0.672(48)	0.396(20)	0.382(18)
m_ρ	0.822(10)	0.4407(90)	0.352(13)
m_{b_1}	1.16(11)	1.08(29)	0.81(18)
m_{ρ_2}	0.946(11)	0.4090(89)	0.351(15)
m_{a_1}	0.988(40)	0.653(78)	0.585(93)
$\sigma^{1/2}$	0.3318(77)	0.1488(75)	0.133(12)

Table 4.15: Values of various observables at massless quark limit via linear extrapolation for eight flavors.

the lattice cutoff and volume. Thus, the applicability of chiral perturbation theory is not at all clear in this circumstances.

Therefore, the linear extrapolations are employed here. And given the quality of the data and the amount of statistics, it is believable that such linear extrapolations do give qualitative results and provide a sneak peek at the nature of the system that has a walking coupling constant. However, it is important to remember that this ansatz is made.

4.6.2 Establishing Phases with Linear Extrapolation

Table 4.15 and 4.16 shows the results of linear extrapolation of various quantities for eight and twelve flavors, respectively. With twelve flavors, to avoid the distortion brought in by the mass dependent rapid cross over, which will be discussed later, the results from $m_q = 0.01$ at $\beta = 0.46$ and $m_q = 0.03$ at $\beta = 0.48$ are not included in the extrapolations. The errors quoted in the table are determined by super-jackknife method, which is described in the appendix A.2.

β	0.45	0.46	0.48	0.49	0.50
$\langle\bar{\psi}\psi\rangle$	0.30878(33)	0.2655(11)	-0.00382(20)	0.00249(19)	0.00199(14)
f_π	0.2699(34)	0.2390(76)	0.0237(30)	0.0258(13)	0.01336(97)
m_π^2	0.00449(13)	0.01141(44)	0.02550(80)	0.01957(66)	0.0477(23)
m_{π_2}			0.130(14)	0.1322(66)	0.251(14)
m_σ			0.173(13)	0.2173(92)	0.1799(74)
m_ρ			0.1680(84)	0.1875(61)	0.3481(73)
m_{b_1}			0.428(92)	0.413(73)	0.389(45)
m_{ρ_2}		1.225(49)	0.1539(90)	0.1879(71)	0.3693(79)
m_{a_1}			0.184(66)	0.288(28)	0.342(16)
$\sigma^{1/2}$		0.701(81)	0.005(12)	0.020(10)	0.041(21)

Table 4.16: Values of various observables at massless quark limit via linear extrapolation for twelve flavors. At $\beta = 0.46$, only measurements from $m_q = 0.02, 0.03$ are used; while at $\beta = 0.48$, only from $m_q = 0.01, 0.02$. Please see text for explanation.

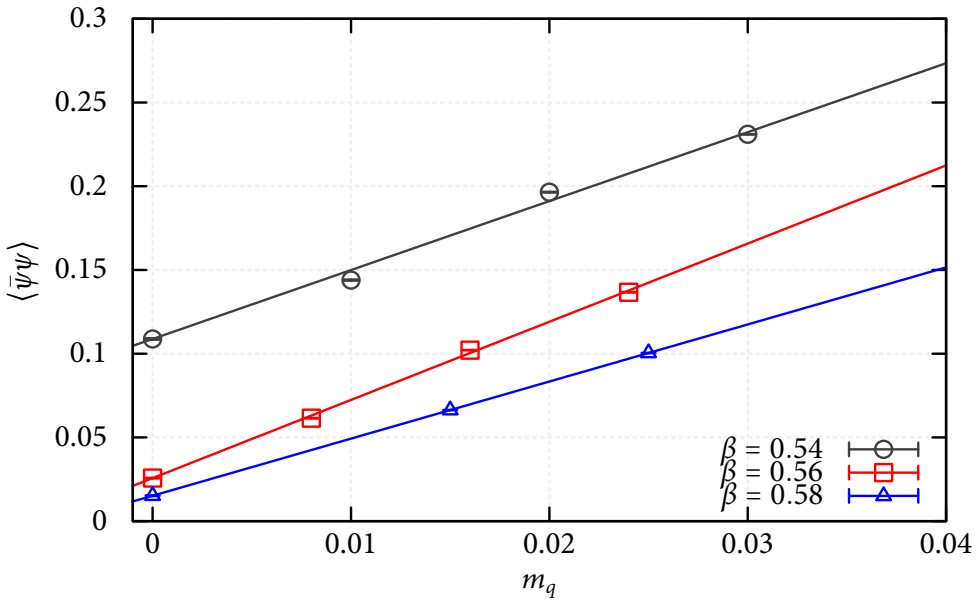

Figure 4.16: $\langle\bar{\psi}\psi\rangle$ with eight flavors.

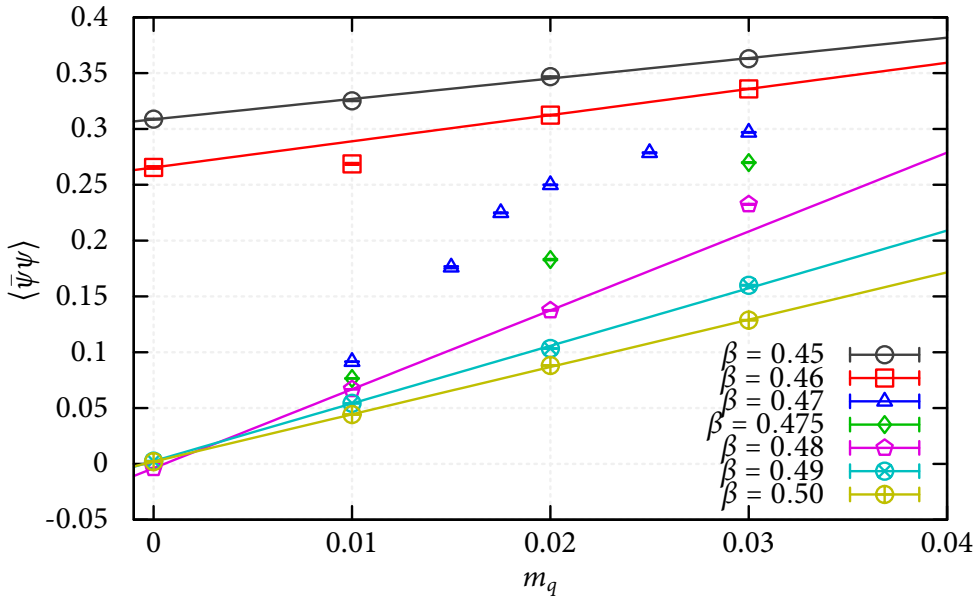

Figure 4.17: $\langle\bar{\psi}\psi\rangle$ with twelve flavors.

Figure 4.16 and 4.17 show $\langle\bar{\psi}\psi\rangle$ with various couplings and mass points for eight flavors and twelve flavors, respectively. With both eight and twelve flavors, non-zero values of $\langle\bar{\psi}\psi\rangle$ in the chiral limit, in the strong coupling region, $\beta \simeq 0.54$ for eight flavors and $\beta \lesssim 0.46$ for twelve flavors, suggest the system is clearly in a chirally broken phase. And the Goldstone pion behavior, $m_\pi^2 \propto m_q$ shown in figure 4.18 and 4.19, verifies this assertion that the system has broken chiral symmetry in the massless quark limit.

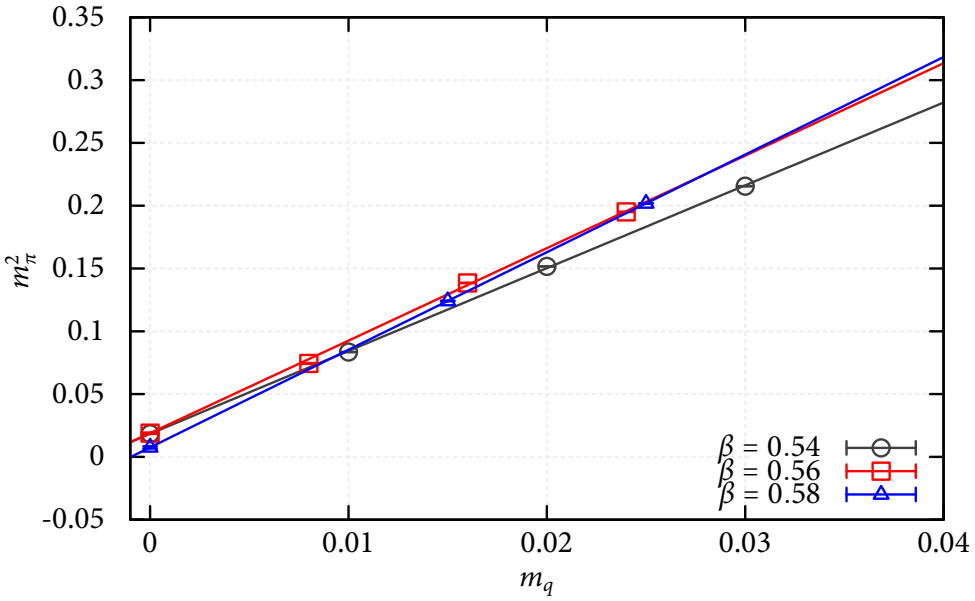

Figure 4.18: m_π^2 with eight flavors.

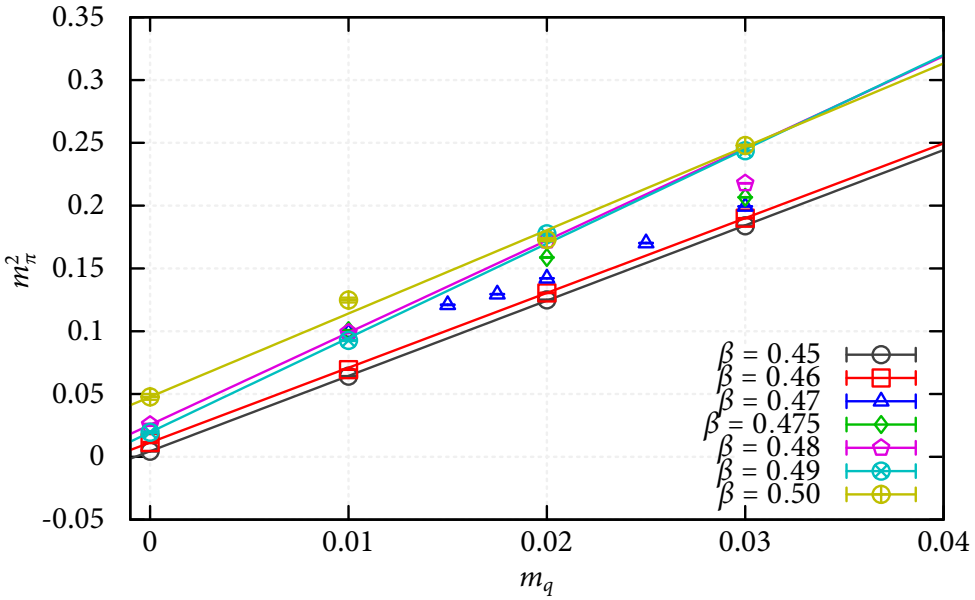

Figure 4.19: m_π^2 with twelve flavors.

While decreasing the input bare coupling, for eight flavors, the change of $\langle\bar{\psi}\psi\rangle$ in

lattice units in the chiral limit from $\beta = 0.54$ to $\beta = 0.56$ is much larger than the change from $\beta = 0.56$ to $\beta = 0.58$, though these three lattice bare couplings are equally spaced. Such change is also seen with twelve flavors. In addition, it can be seen that there is a clear mass dependent cross-over from $\beta \simeq 0.45$ to $\beta \simeq 0.49$. Figure 4.20 shows the evolution of $\langle\bar{\psi}\psi\rangle$ at various quark masses with $\beta = 0.47$ for twelve flavors. The visible longer thermalization time and longer autocorrelation at $m_q = 0.015$ indicates that, at this quark mass, the system is closer (compared to systems at other masses) to the second order critical point, which will be described in section 6.2, and the system is influenced by it the most.

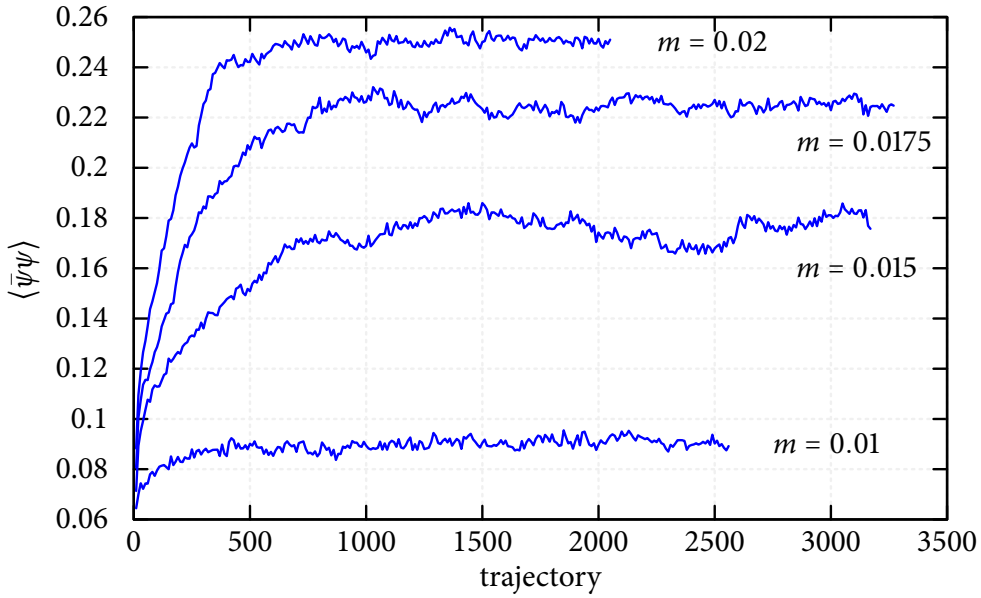

Figure 4.20: $\langle\bar{\psi}\psi\rangle$ at $\beta = 0.47$ with twelve flavors for different m_q.

In the following discussions the region between $\beta \simeq 0.54$ and $\simeq 0.58$ (for eight flavors) will be referred to as $\Delta\beta_8$ and the region from $\beta \simeq 0.46$ and $\simeq 0.49$ (for twelve flavors) as $\Delta\beta_{12}$. In this range of β values, both systems are showing rapid changes. The evolution of $\langle\bar{\psi}\psi\rangle$, both ordered and disordered starts, for eight flavors across this region will be

shown later in figure 6.5 in section 6.1. No signal of a first order lattice artifact bulk transition was observed in this region with the DBW2 gauge action. For twelve flavors, it is unlikely for such first order bulk transition to appear at $m_q \gtrsim 0.02$. Simulations with both ordered and disordered start have been performed, but within the quark masses and input couplings studied with large quark masses, $m_q \geq 0.01$, no clear bulk transition is visible. From figure 4.17, this cross over becomes more rapid when the quark mass becomes smaller. A bulk transition is indeed found with much smaller quark masses presented here. It will be discussed in section 6.2. The rapid cross-over for both eight and twelve flavors may be influenced by lattice higher order operators, which are irrelevant in the continuum limit, but manifest themselves in the large a^2 errors when the bare input lattice coupling is strong.

Both systems of eight and twelve flavors exhibit convex curves of $\langle\bar{\psi}\psi\rangle$ versus m_q at fixed β, at the strong coupling side of $\Delta\beta$ region, indicating while changing bare coupling, the simulations with smaller quark masses enters the cross-over prior to the simulations with larger masses. And the concave curve of $\langle\bar{\psi}\psi\rangle$ versus m_q at fixed β, at the weak coupling side, shown clearly for twelve flavors, shows that the simulations with smaller quark masses receive less influence from the cross-over. However, it is unclear how large this influence is to the system with large mass at $\beta = 0.48$. Nevertheless at $\beta = 0.49$, it can be seen from the linear extrapolations that the influence of the cross over is very small at $m_q = 0.03$. With this slight concave shape of the $\langle\bar{\psi}\psi\rangle$ values at $m_q = 0.01$, 0.02 and 0.03, it can be certain that the extrapolated value at massless limit is the lower bound of the $\langle\bar{\psi}\psi\rangle$ that could be obtained from linear extrapolations.

The true continuum physics of the system is simulated in the weak coupling side of the cross-over, at $\beta > \Delta\beta$. It can be still seen clearly, with eight flavors, that the chiral

condensate in the chiral limit is non-zero and $m_\pi^2 = 2Bm_q$, which indicate that the system is still in the chirally broken phase with eight flavors. For twelve flavors in the weak coupling region, the extrapolation of $\langle\bar{\psi}\psi\rangle$ becomes very small at $\beta = 0.49$, but with the large volume ($32^3\times32$), $m_\pi^2 = 2Bm_q$ is well satisfied. It is known that finite volume effects can affect the extrapolation of m_π^2 to $m_q = 0$ in 4 flavors [67]. Comparing the results of observables obtained in 2 different volumes for $\beta = 0.49$, there might still be $\lesssim 10\%$ error introduced by finite size effect. Nevertheless, the evidence argues in favor of the existence of a non-zero dimensionful parameter, B, which suggests that the system be in the chirally broken phase.

Although the deeper mechanism is unknown to the author of this thesis, it is interesting to note that this dimensionful parameter B (from $m_\pi^2 = 2Bm_q$) in lattice units barely changes (from ~ 3 to ~ 4) across the cross over region $\Delta\beta$, despite the aforementioned large lattice scale changes in eight and twelve flavors. In addition, the values of B in lattice units from both eight and twelve flavors are almost the same, and do not differ much from 2+1 flavors studies or even quenched studies (usually around ~ 3.5).

All evidence gathered in this thesis is consistent with the phenomenon of chiral symmetry breaking, but with a much smaller scale in lattice units than the theory with $\beta \lesssim 0.45$. The lattice scale change can be analyzed via different observables.

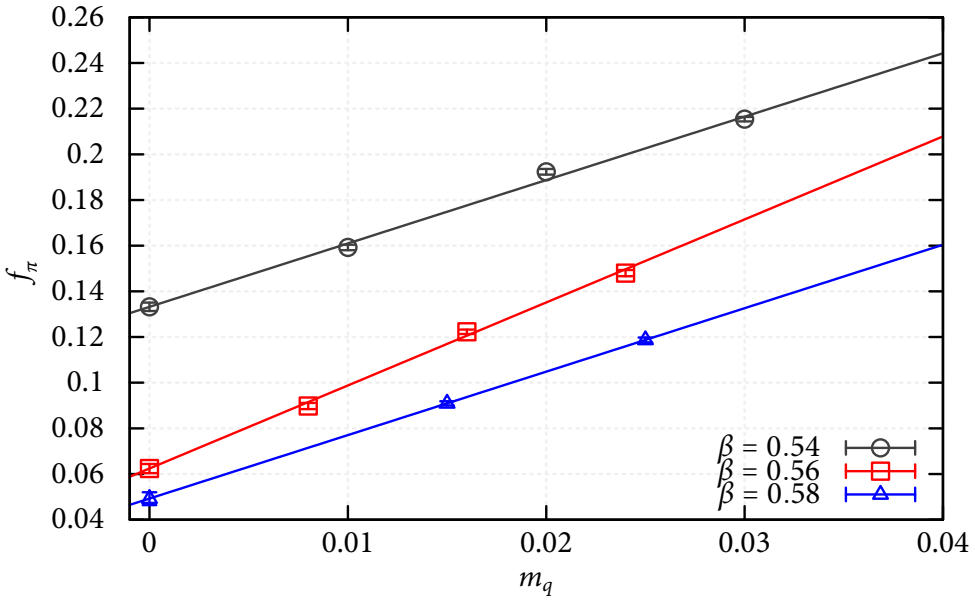

Figure 4.21: f_π with eight flavors.

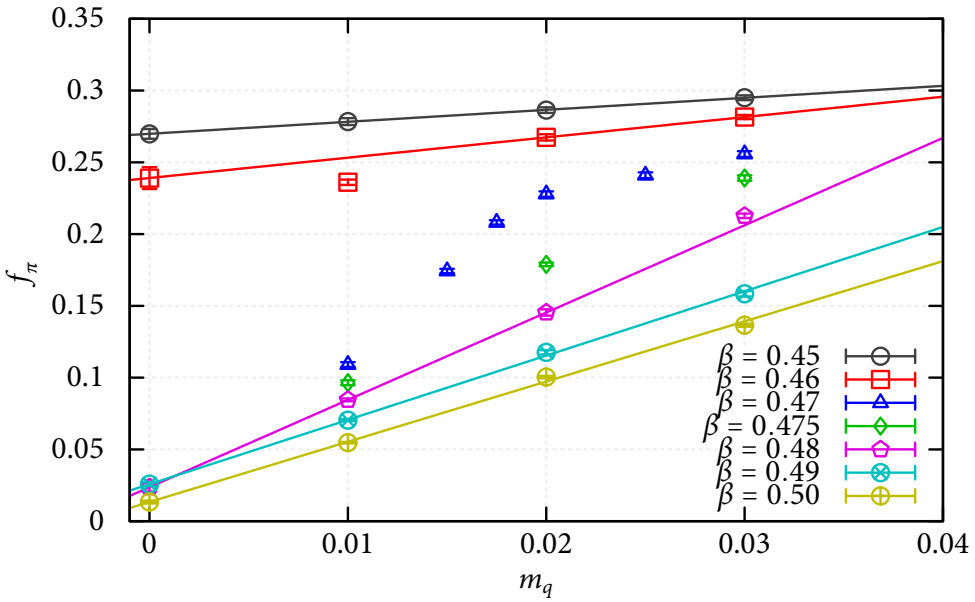

Figure 4.22: f_π with twelve flavors.

Shown in figure 4.21 and 4.22, is the pion decay constant, f_π, for both eight and twelve

flavors, respectively. There is the evidence for a non-zero dimensionful parameter, f_π, on the weak coupling side of $\Delta\beta$ region. The values of f_π in the chiral limit changes by about 2 times for eight flavors, across the $\Delta\beta_8$ region; for twelve flavors, across the $\Delta\beta_{12}$ region, this change is about 10 times. The Gell–Mann–Oakes–Renner relation, $\langle\bar{\psi}\psi\rangle \propto m_\pi^2 f_\pi^2/m_q$, can be used to predict the scale change of $\langle\bar{\psi}\psi\rangle$. The value of m_π^2/m_q is almost independent of β for both eight and twelve flavors on both sides of $\Delta\beta$ region, which means that $\langle\bar{\psi}\psi\rangle \propto f_\pi^2$ across the region. This gives a 4 times change in $\langle\bar{\psi}\psi\rangle$ for eight flavors, which can be verified by the extrapolated value of $\langle\bar{\psi}\psi\rangle$ at massless quark limit; and a 100 times change in $\langle\bar{\psi}\psi\rangle$ for twelve flavors, which is a very small value that is indistinguishable from zero within the error from numeric simulations, and most importantly, it is consistent with the aforementioned scale change expected from the change in f_π.

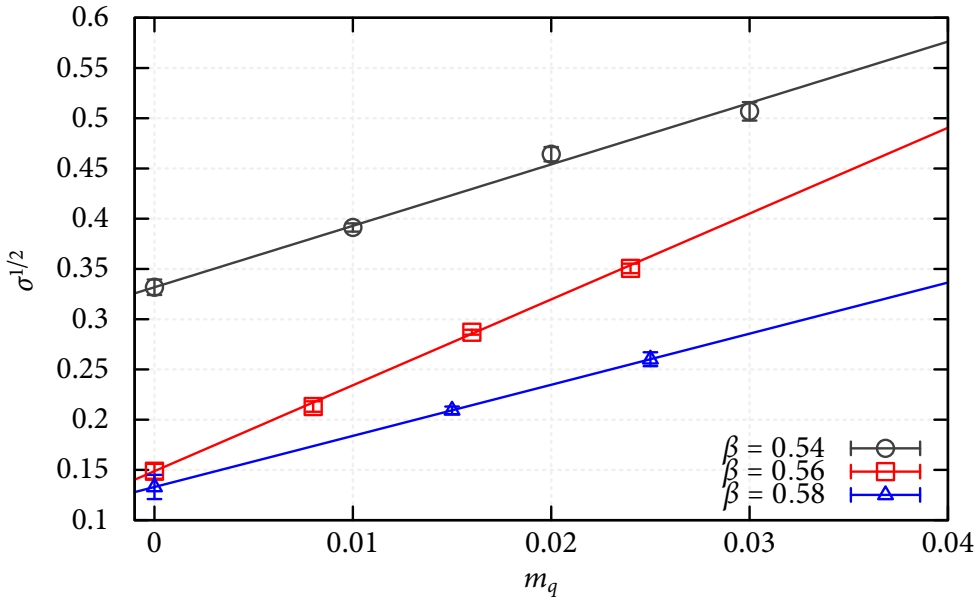

Figure 4.23: $\sigma^{1/2}$ with eight flavors.

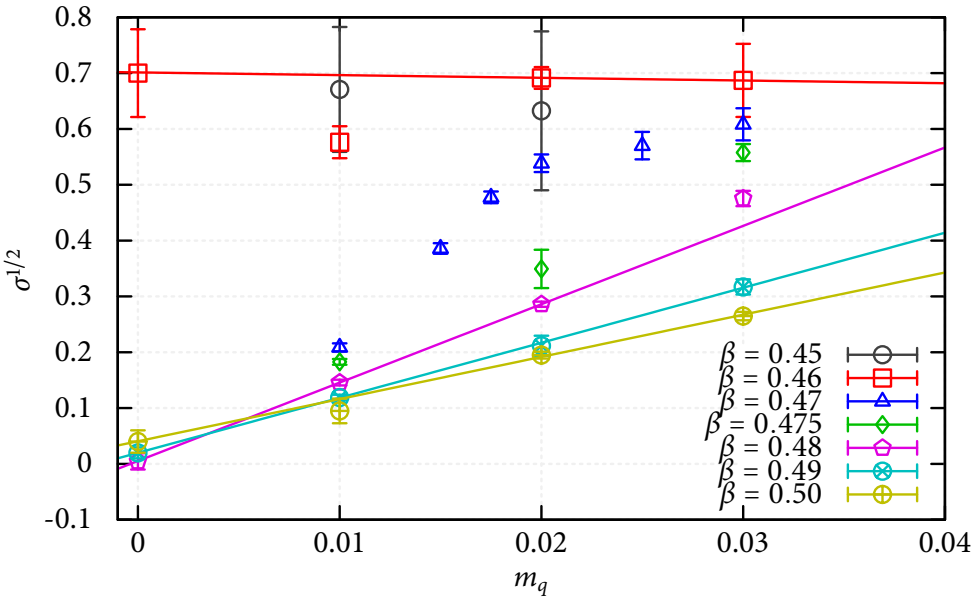

Figure 4.24: $\sigma^{1/2}$ with twelve flavors.

The string tension, σ, is also a good candidate for investigating scale changes, shown in figure 4.23 and 4.24, for both eight and twelve flavors, respectively. Being a dimension 2 quantity, σ should scale as f_π^2. It is easily seen for eight flavors that the value of σ in lattice units changes by roughly 4 times, which is consistent with aforementioned scale change. For twelve flavors, a 100 times change of σ is expected in lattice unit as for $\langle\bar{\psi}\psi\rangle$. In numerical studies, it is very hard to extract string tension reliably for either very large values or very small values. Unfortunately, on both sides of $\Delta\beta_{12}$ region, the values of string tension are pushing the limit of numerical reliability. Nonetheless, these values are consistent with a 100 times change.

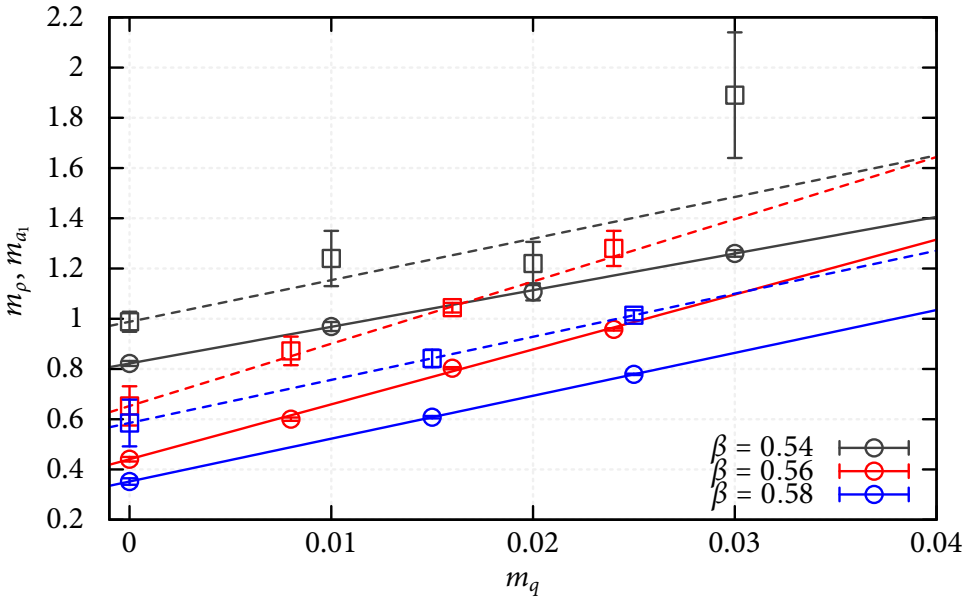

Figure 4.25: m_ρ versus m_{a_1} with eight flavors. Circles and solid lines are data points and linear fits respectively for m_ρ, while boxes and dashed lines represent m_{a_1}.

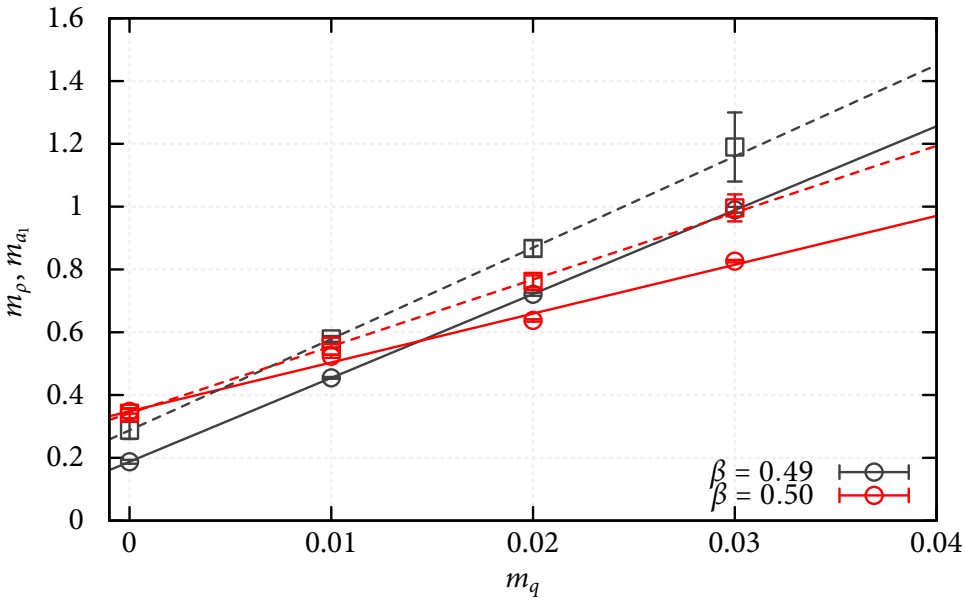

Figure 4.26: m_ρ versus m_{a_1} with twelve flavors. Circles and solid lines are data points and linear fits respectively for m_ρ, while boxes and dashed lines represent m_{a_1}.

It was observed [72] that, for 4 flavors, the spectrum of parity partners, like the ρ and a_1 , becomes degenerate if the volume is too small, even if the theory is still in the broken chiral symmetry phase. The masses of the ρ and a_1 are shown in figure 4.25 and 4.26, where, for twelve flavors, only values at weaker couplings are shown, because the larger masses that result from stronger coupling are hard to extract. Eight-flavor QCD shows no visible parity doubling, while for twelve flavors parity doubling is clearly visible at $\beta = 0.50$, but not at $\beta = 0.49$. It suggests that finite volume effects are present in the simulations at $\beta = 0.50$. However, the finite size effect at $\beta = 0.49$ is small because of the use of a larger volume ($32^3 \times 32$). In addition to that the chiral symmetry is indeed broken spontaneously in the twelve flavor theory.

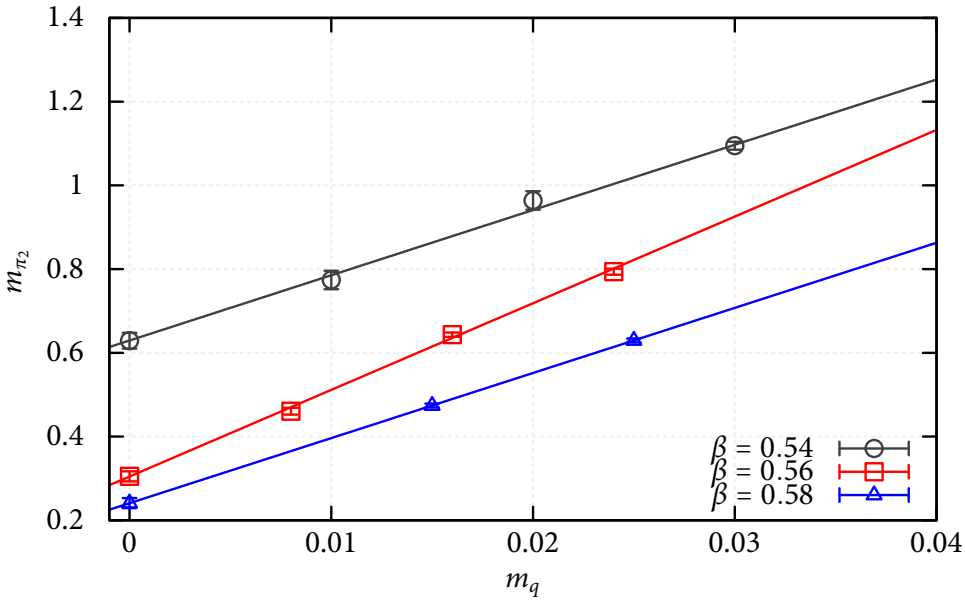

Figure 4.27: m_{π_2} with eight flavors.

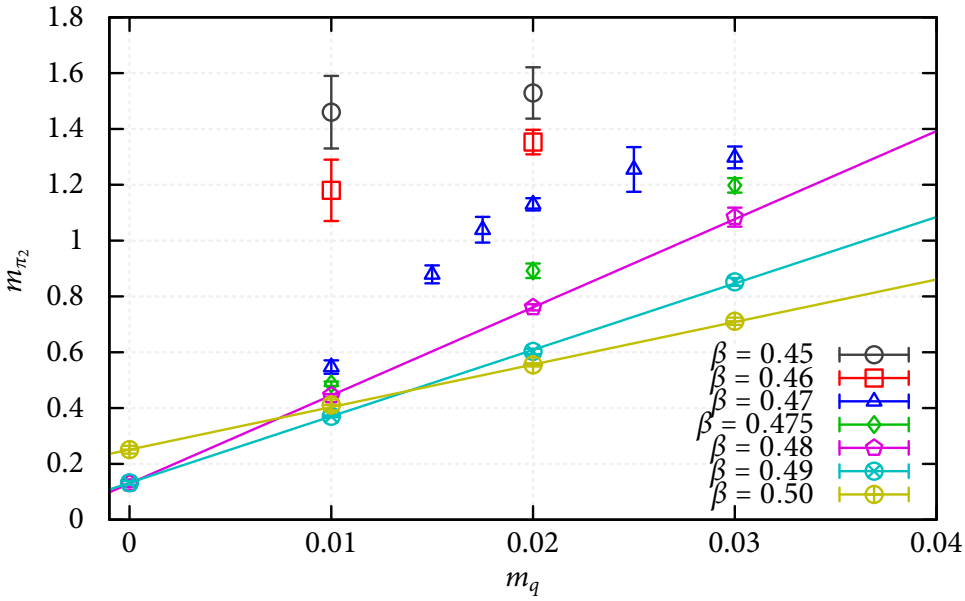

Figure 4.28: m_{π_2} with twelve flavors.

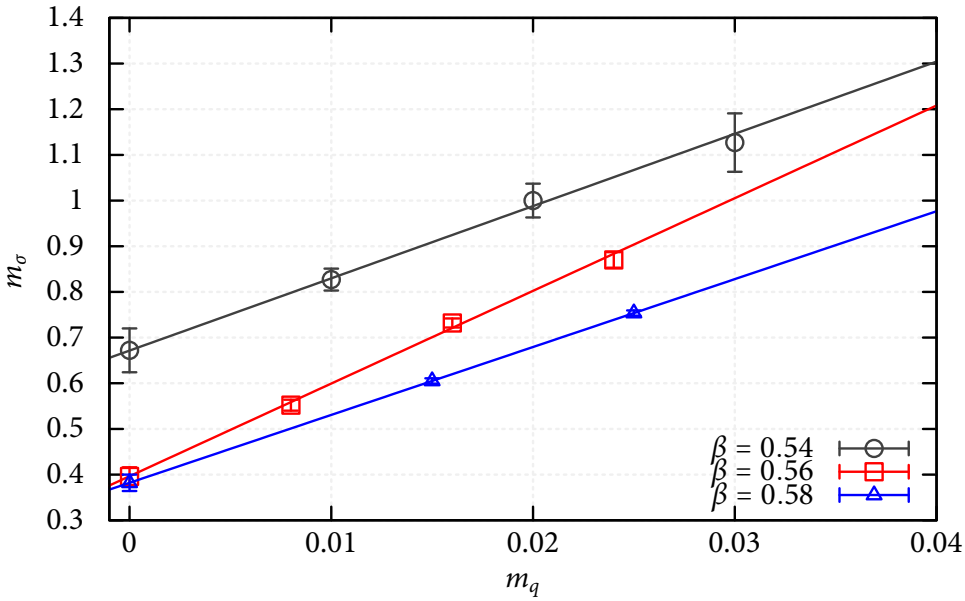

Figure 4.29: m_σ with eight flavors.

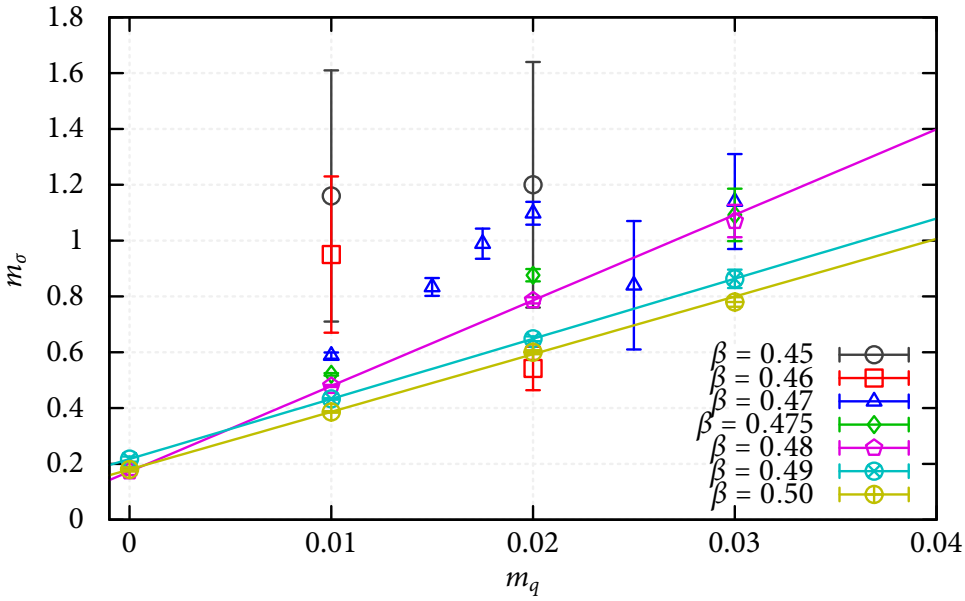

Figure 4.30: m_σ with twelve flavors.

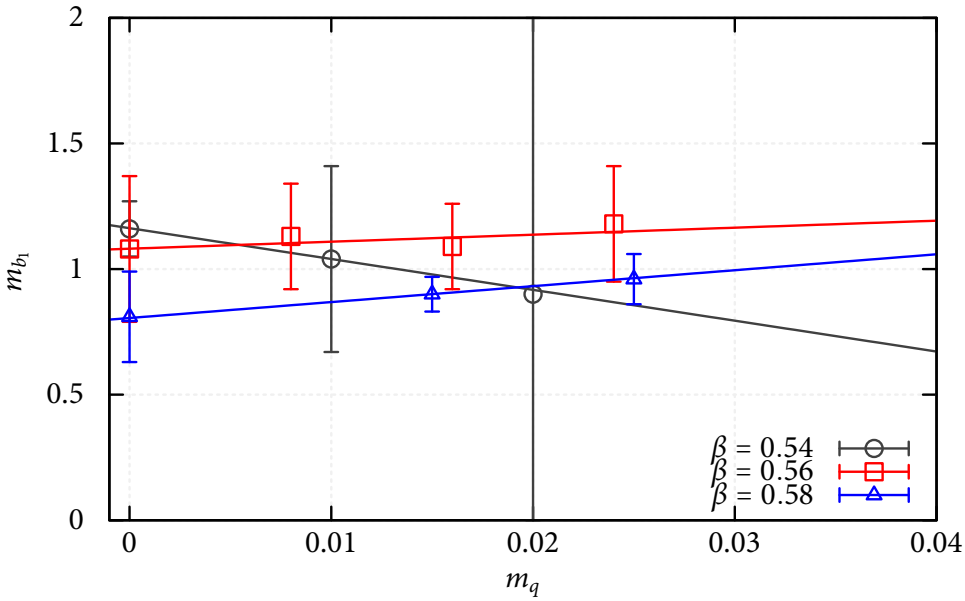

Figure 4.31: m_{b_1} with eight flavors.

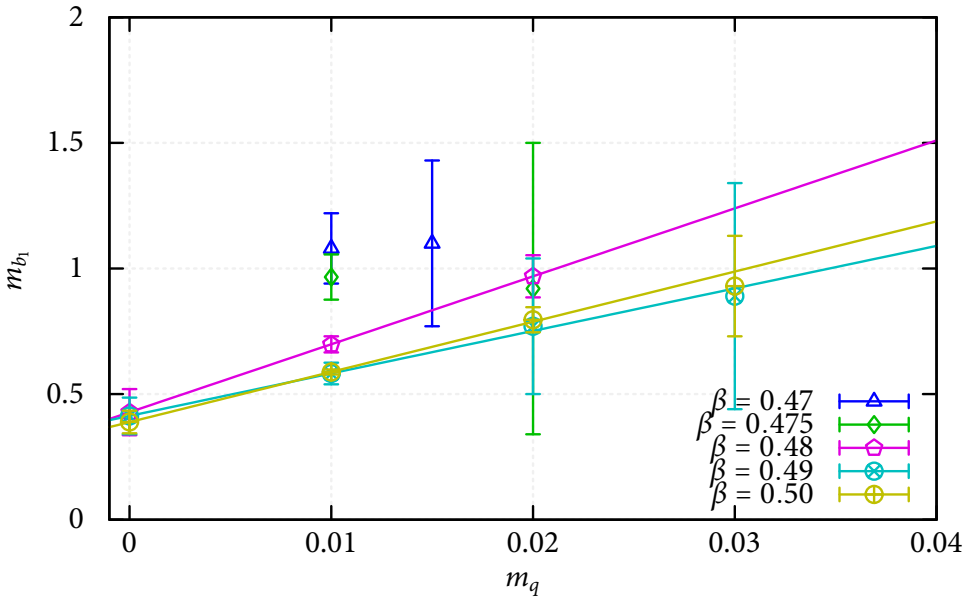

Figure 4.32: m_{b_1} with twelve flavors.

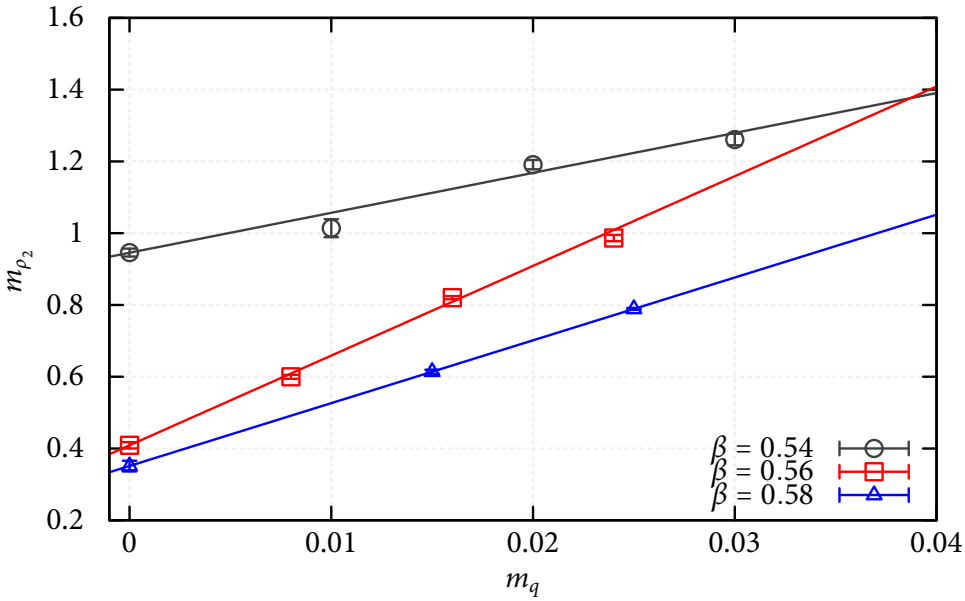

Figure 4.33: m_{ρ_2} with eight flavors.

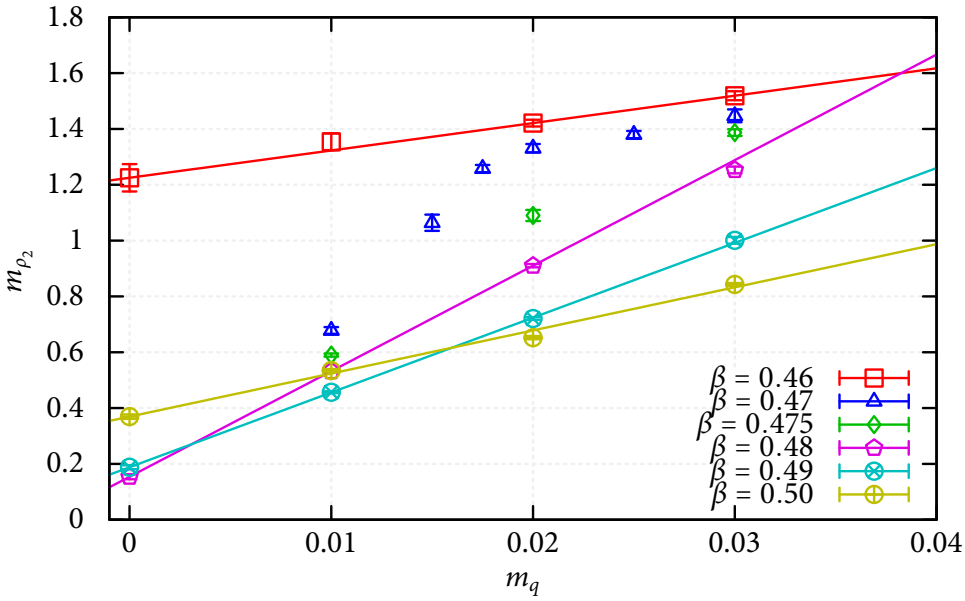

Figure 4.34: m_{ρ_2} with twelve flavors.

The rest of the extrapolation figures, 4.27, 4.28, 4.29, 4.30, 4.31, 4.32, 4.33 and 4.34 show that the linear extrapolations describe the data fairly well, and they all exhibit the same rapid cross over region.

4.7 Flavor Symmetry Breaking

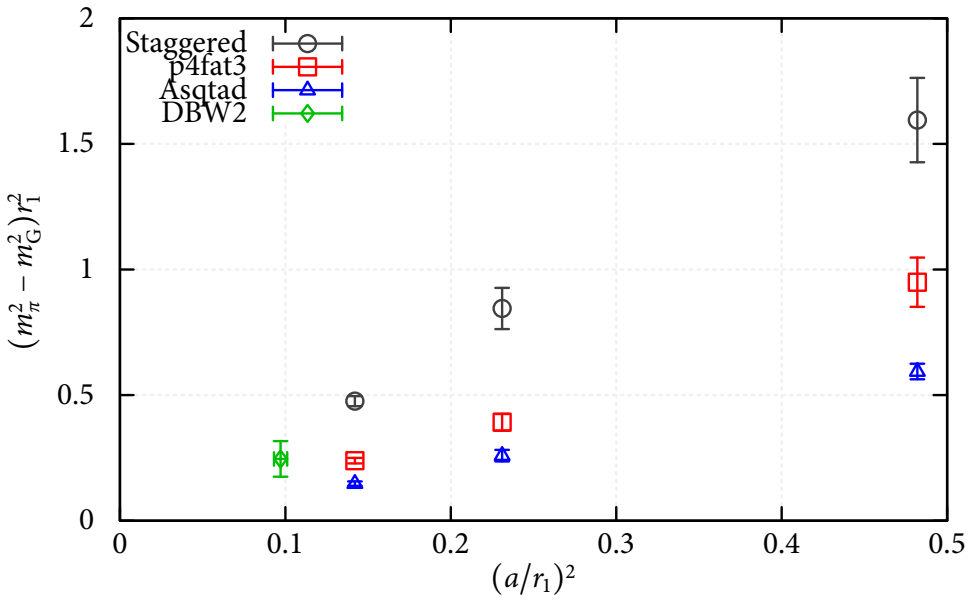

Figure 4.35: A comparison of $N_f = 2$ DBW2 results with quenched results from [1], where the chiral limit has been taken. Except for the "DBW2" points, all labels refer to the type of valence quark used on a quenched ensemble.

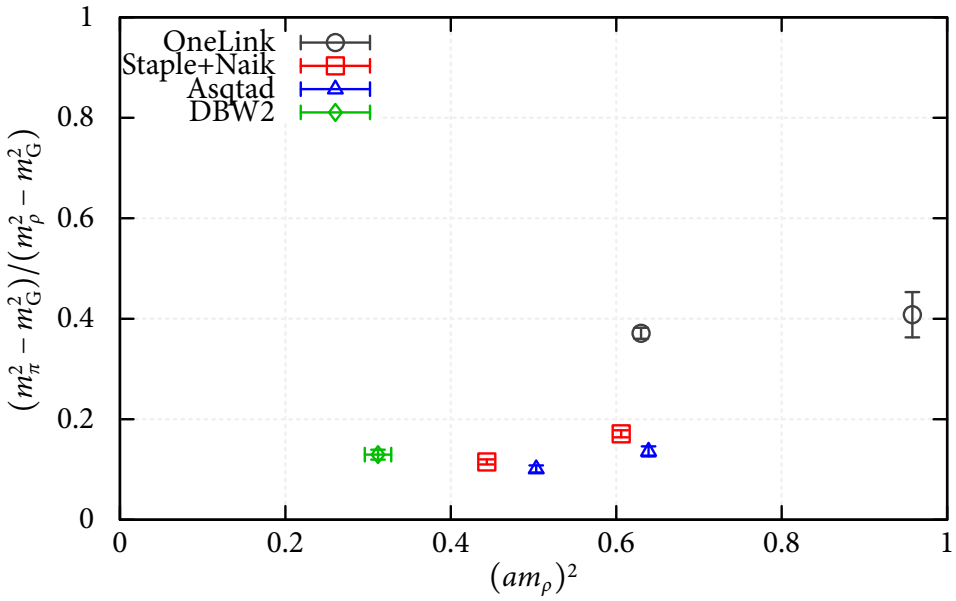

Figure 4.36: A comparison of $N_f = 2$ DBW2 results with $N_f = 2$ results from [2, 3] at $m_\pi/m_\rho = 0.55$. Except for the "DBW2" points, all labels refer to the type of valence quark used on a fixed dynamical ensemble.

Flavor symmetry breaking effects have been measured between the Goldstone pion and the non-local (non-Goldstone) pions for the DBW2 simulations with naive staggered fermions and 2 dynamical flavors. In figure 4.35 and figure 4.36, our results are compared with results from improved staggered actions in quenched [1] and 2-flavor ("Staple+Naik" sea quarks with Symanzik improved gauge action) [2, 3] simulations. Although the comparisons are at different lattice spacings, it appears that the DBW2 gauge action has reduced the splittings seen with naive staggered fermions and the Wilson gauge action.

For a realistic measurement of the splitting at the number of quark flavors, all the non-local pions at $\beta = 0.56$ for eight flavors and $\beta = 0.49$ for twelve flavors have been measured. The resulting pion masses are in table 4.17 and 4.18. The pion states are labeled

using the conventions set forth in [73], which labels meson states by their transformation properties under the lattice symmetry group ($r^{\sigma_s\sigma_{123}}$). In figure 4.37, for eight flavors, all the pions has good linearity of m_π^2 versus m_q, and their extrapolations surprisingly vanish in the massless quark limit. And for twelve flavors in figure 4.38, the results are quite non-linear. Apart from the local (Goldstone) pion, the behavior of the non-local pions are astonishingly different from those of conventional QCD with 2 flavors or 2+1 flavors studies. Currently the author of this thesis is still lack of understandings as to why such behavior change would take place when the number of flavors is increased.

m_q	0.008	0.016	0.024
$t_{\min}$	6	6	4
$1++$	0.4588(38)	0.6564(51)	0.7995(30)
$1+-$	0.27274(56)	0.37230(26)	0.44166(13)
	0.4594(17)	0.6530(20)	0.8013(21)
$3''--$	0.4615(18)	0.6543(25)	0.7972(21)
	0.4600(19)	0.6515(24)	0.7975(22)
	0.4930(39)	0.7184(72)	0.8739(49)
$3''-+$	0.4924(43)	0.7151(75)	0.8865(51)
	0.4959(43)	0.7199(62)	0.8791(64)
	0.5098(40)	0.7400(84)	0.9035(59)
$3''++$	0.5046(45)	0.7394(74)	0.9146(73)
	0.5074(56)	0.7532(94)	0.9124(72)
	0.4902(22)	0.7090(39)	0.8741(33)
$3''+-$	0.4941(27)	0.7107(58)	0.8833(32)
	0.4934(17)	0.7115(44)	0.8841(39)
$1--$	0.5079(31)	0.7323(36)	0.9184(42)

Table 4.17: Non-local pion masses at $\beta = 0.56$ with a lattice size of $24^3\times32$ for eight flavors.

m_q	0.01	0.02	0.03
$t_{\min}$	11	8	6
$1++$	0.3847(25)	0.6377(78)	0.887(18)
$1+-$	0.30149(82)	0.42243(79)	0.49364(34)
$3''--$	0.3776(20)	0.6319(34)	0.8700(85)
	0.3782(18)	0.6268(31)	0.886(10)
	0.3776(25)	0.6266(28)	0.8784(80)
$3''-+$	0.3870(22)	0.6569(74)	0.926(27)
	0.3883(23)	0.6485(87)	0.929(24)
	0.3887(27)	0.6474(85)	0.959(19)
$3''++$	0.3900(27)	0.6622(95)	0.987(45)
	0.3911(23)	0.6784(77)	1.023(33)
	0.3931(33)	0.6651(84)	0.972(38)
$3''+-$	0.3873(21)	0.6567(59)	0.982(10)
	0.3875(22)	0.6617(52)	0.966(23)
	0.3875(22)	0.6556(67)	0.960(18)
$1--$	0.3903(23)	0.6726(47)	1.019(26)

Table 4.18: Non-local pion masses at $\beta = 0.49$ with lattice sizes of $32^3\times32$ with $m_q = 0.01$ and $16^3\times32$ with $m_q = 0.02$ and 0.03, for twelve flavors.

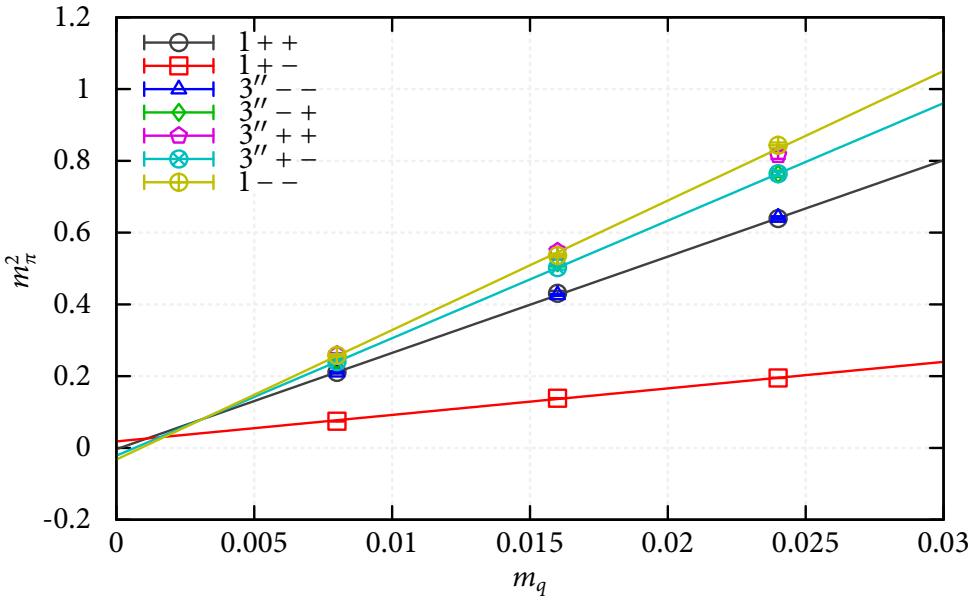

Figure 4.37: Mass splittings of all pions (local and non-local, except the singlet) for eight flavors at $\beta = 0.56$. Linear fits are done through states of $1 + -$, $1 + +$, $3'' + -$ and $1 - -$, from the bottom of the figure to the top.

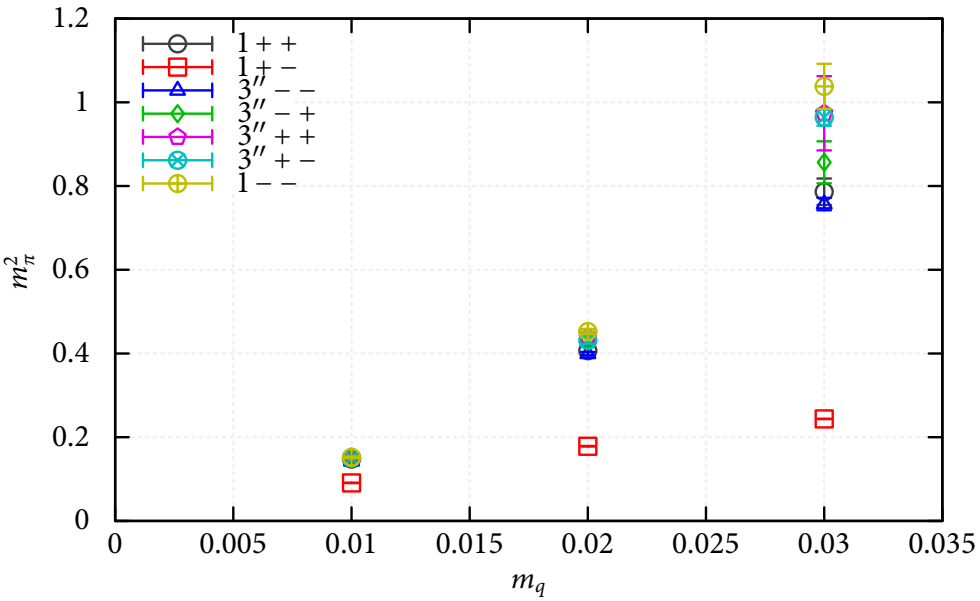

Figure 4.38: Mass splittings of all pions (local and non-local, except the singlet) for twelve flavors at $\beta = 0.49$.

The existence of non-Goldstone non-local pions is not a threat to the argument that the system has spontaneously broken chiral symmetry. Other hadronic observables measured might be affected a little by not having all the true light pions. However, the existence of the true pseudo Goldstone pion is a strong evidence that the chiral symmetry is spontaneously broken in the system with eight and twelve flavors.

4.8 Scaling Behavior and N_f Dependence

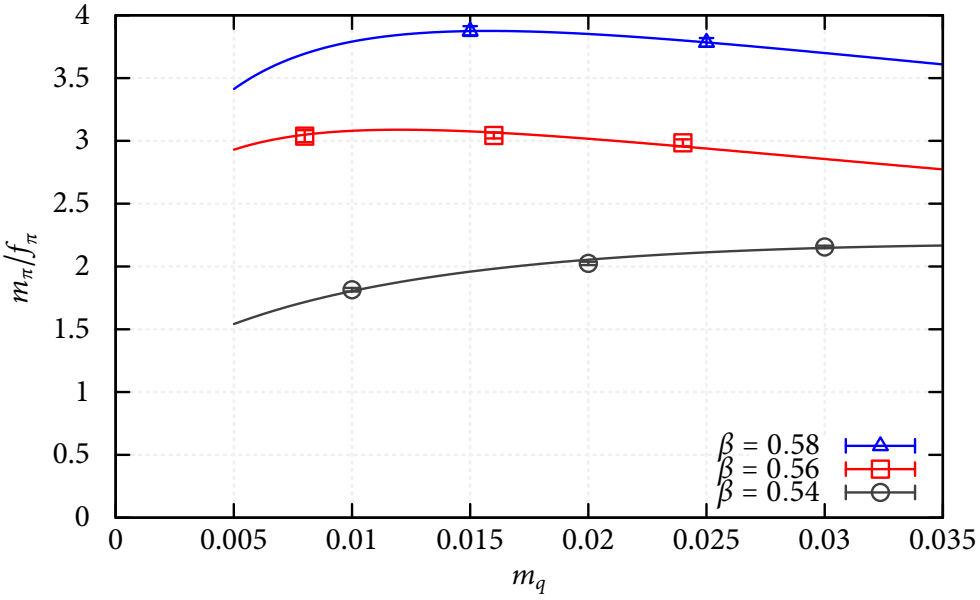

Figure 4.39: m_π/f_π versus m_q with eight flavors.

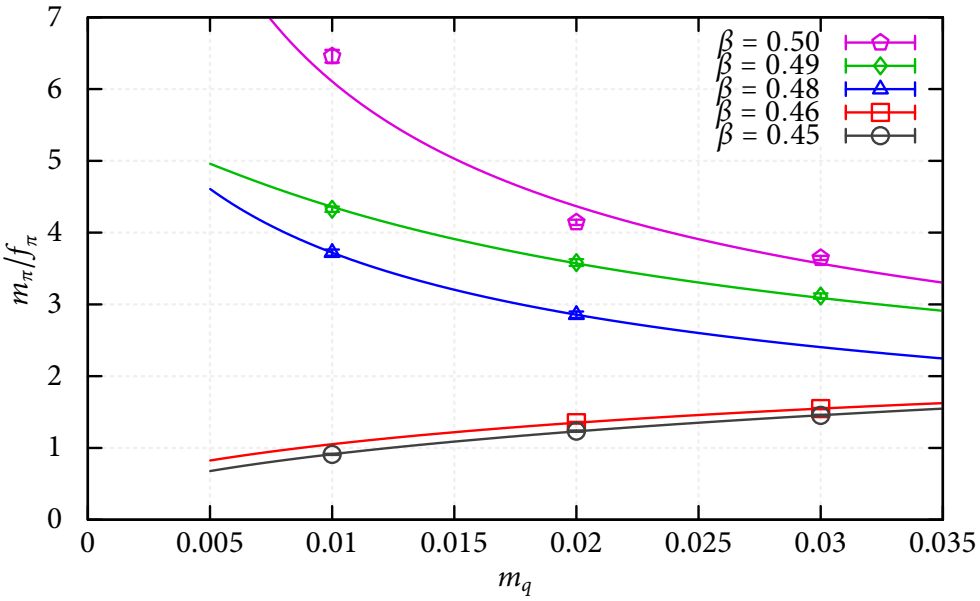

Figure 4.40: m_π/f_π versus m_q with twelve flavors.

Figure 4.39 and 4.40 shows how the dimensionless ratio, m_π/f_π, changes with the input quark mass, m_q, for eight and twelve flavors, respectively. The curves are the ratio of the functional forms of m_π and f_π obtained by linear extrapolation. Only the curve of m_π/f_π in the quark mass region simulated in this thesis is shown. Both figures show different behavior from those obtained with 2 + 1 flavors simulations, where m_π/f_π is usually an increasing function of m_q, as expected that $\lim_{m_q \to 0} m_\pi \to 0$.

With eight flavors, m_π/f_π becomes a decreasing function for $\beta > 0.56$ and $m_q > 0.015$. It is already argued previously in this thesis that the system with eight flavors is chirally broken, thus m_π/f_π must vanish in the chiral limit, where m_π vanishes and f_π stays finite. Therefore, in figure 4.39, the ratio m_π/f_π must rise rapidly in the small quark mass region, $m_q < 0.005$, and in the weak coupling region, $\beta \geq 0.56$. This makes the common practice of testing the scaling behavior of the lattice theory by fixing dimensionless ratios, such like m_π/f_π, much harder than 2 + 1 flavors, because much smaller quark masses must be

used to have a equal m_π/f_π for different couplings.

Such behavior becomes dramatic with twelve flavors. In figure 4.40, at $\beta \geq 0.48$, the ratio, m_π/f_π, becomes a purely decreasing function of m_q in the quark mass region simulated in this thesis. In the strong coupling region, $\beta \sim 0.45$ and 0.46, the practice of fixing m_π/f_π and doing a scaling test can be performed as usual. However, at weak coupling, $\beta \geq 0.48$, if the ratio of m_π/f_π at the quark mass range simulated in this thesis is fixed, it would result in a flow toward coarser lattices as β becomes larger by fixing m_π/f_π. It is important to note that this kind of "backward flow" does not lead to a continuum limit. To do a proper continuum scaling test, much smaller quark masses are required, where m_π becomes much smaller, so that m_π/f_π appears to be an increasing function of m_q in that region. Other hadronic scales instead of f_π could have been used to do the same scaling study, and the conclusion would be the same. Any study trying to probe the continuum limit from mass ratios in current quark mass region studied would lead to erroneous results. This is very important behavior, and needs to be considered for future simulations. If one wants to study the scaling of mass ratios at finite quark masses, much smaller input quark masses are needed in the simulations. If the naive lattice scale argument in section 4.6.2 was right, at least 10× smaller quark mass, $m_q \sim 0.001$, is needed to see the ratio m_π/f_π become a increasing function of m_q.

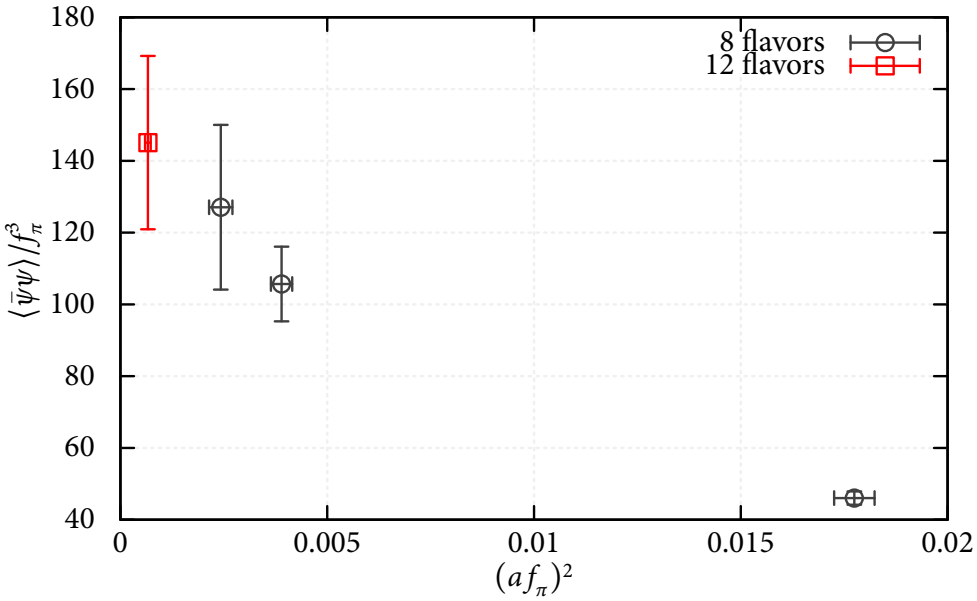

Figure 4.41: $\langle\bar{\psi}\psi\rangle$ versus f_π in the chiral limit. For twelve flavors, only result from $\beta = 0.49$ is shown.

Figure 4.41 shows the unrenormalized $\langle\bar{\psi}\psi\rangle$ versus a^2 in units of f_π in the chiral limit. For twelve flavors, only the result from $\beta = 0.49$ is shown. Because the scale of f_π differs a lot from eight flavors and twelve flavors, it is hard to make justified conclusions. However, as expected from a theory with slowly running coupling constant discussed in section 2.3, the values computed here for eight and twelve flavors are much larger than the QCD value (of order ~ 10), apart from an undetermined renormalization constant.

Chapter 5

Simulation Results at Finite Temperatures

5.1 Finite Temperature Study

Considerable evidence has been presented that both eight and twelve flavors at zero temperature is in a chirally broken phase. A check of these arguments is to run at finite temperature and look for evidence of chiral symmetry restoration. A few finite temperature simulations have been done: at fixed $\beta = 0.56$ and $m_q = 0.008$ and 0.016 with a lattice size of $24^3 \times 8$ for eight flavors; and at fixed $\beta = 0.49$ and $m_q = 0.01$ and 0.02 with a lattice size of $32^3 \times 8$ for twelve flavors. The parameters of simulations are detailed in table 5.1. These two β values were chosen to ensure that the data are from the weak coupling side of the cross over region $\Delta\beta_8$ and $\Delta\beta_{12}$, so the results are not contaminated by the lattice artifacts.

N_f	β	m_q	Size	Trajectories	$e^{-\Delta H}$	acceptance
8	0.56	0.008	$24^3\times 8$	570-2320	1.0079(85)	0.8280(47)
8	0.56	0.016	$24^3\times 8$	540-2530	1.0095(93)	0.8265(42)
12	0.49	0.01	$32^3\times 8$	540-2130	0.9956(87)	0.8720(42)
12	0.49	0.02	$32^3\times 8$	520-2110	0.989(19)	0.7192(86)

Table 5.1: Parameters of simulations for finite temperature studies at $N_\tau = 8$.

N_f	β	m_q	Size	$\langle\bar\psi\psi\rangle$	plaquette
8	0.56	0.008	$24^3\times 8$	0.03518(12)	0.544240(22)
8	0.56	0.016	$24^3\times 8$	0.07418(41)	0.543007(34)
12	0.49	0.01	$32^3\times 8$	0.041293(53)	0.518273(16)
12	0.49	0.02	$32^3\times 8$	0.08327(11)	0.516656(20)

Table 5.2: Values of $\langle\bar\psi\psi\rangle$ and plaquette from simulations for finite temperature studies at $N_\tau = 8$.

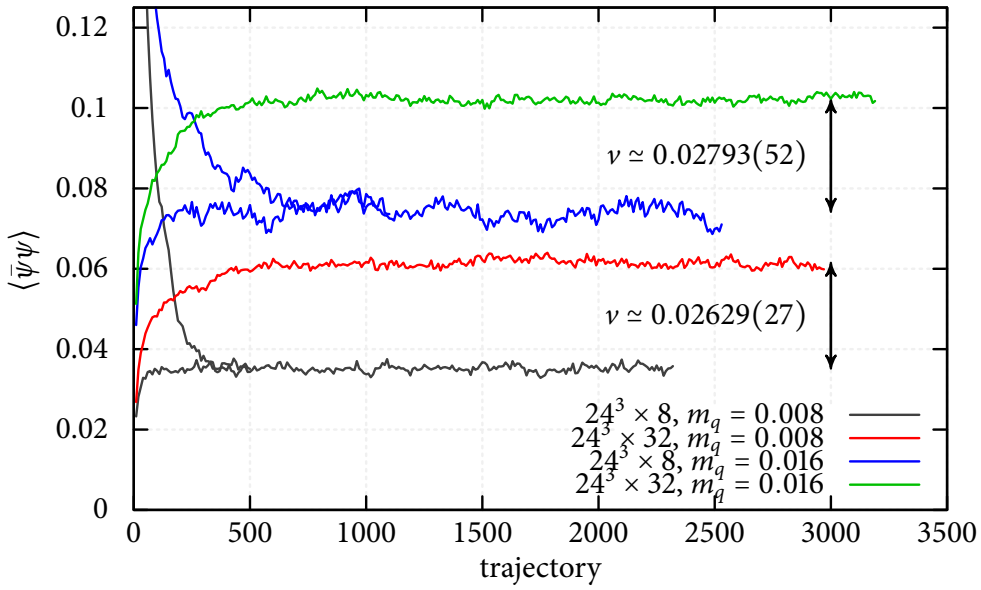

Figure 5.1: Evolution of $\langle\bar\psi\psi\rangle$ with eight flavors at $\beta = 0.56$. Both ordered (curves starting from below) and disordered (curves starting from above) starts are shown for finite temperature evolution.

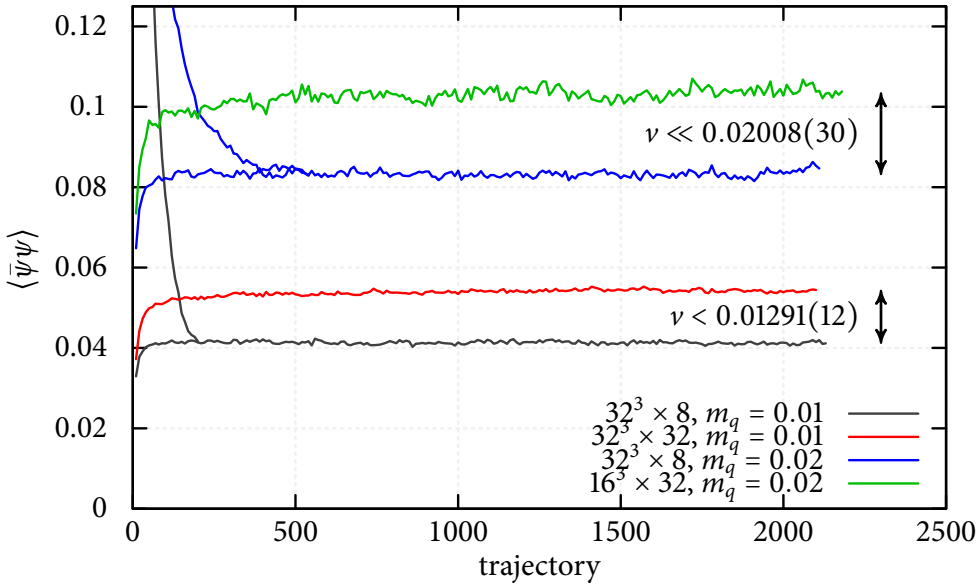

Figure 5.2: Evolution of $\langle\bar{\psi}\psi\rangle$ with twelve flavors at $\beta = 0.49$. Both ordered (curves starting from below) and disordered (curves starting from above) starts are shown for finite temperature evolution.

The evolution of $\langle\bar{\psi}\psi\rangle$ for both ordered and disordered starts is shown in figure 5.1 and 5.2, along with the evolutions from zero temperature. The difference between the values of $\langle\bar{\psi}\psi\rangle$ from $N_\tau = 32$ and from $N_\tau = 8$ simulations are labeled in the figures. The relative size of these differences and the true chiral condensate, μ, in the chiral limit estimated from the linear extrapolations of zero temperature measurements, are indicated in the figure. There are no simple relations between μ and the differences labeled in the figure. However, since the finite temperature $\langle\bar{\psi}\psi\rangle$ at finite quark masses also fits well with the linear ansatz (linearly extrapolate to zero at chiral limit), μ can be estimated from the linear extrapolation of these differences between $\langle\bar{\psi}\psi\rangle$ values from zero temperature and finite temperature simulations. Yet, such extrapolations are not presented here, because the linearity of $\langle\bar{\psi}\psi\rangle$ at finite temperature is not a necessity.

Meson screening masses are measured along the spatial direction with $t_{\min} = 7$ for f_π

m_q	f_π	m_π	m_ρ	m_{b_1}	m_{ρ_2}	m_{a_1}
0.008	0.03928(41)	0.4719(19)	0.8543(59)	0.934(19)	0.922(15)	0.8613(65)
0.016	0.0805(12)	0.4596(27)	0.8758(65)	1.000[27]	0.907(13)	0.910(11)

Table 5.3: Meson masses measured along spatial direction with $24^3\times 8$ at $\beta = 0.56$ for eight flavors.

m_q	f_π	m_π	m_ρ	m_{b_1}	m_{ρ_2}	m_{a_1}
0.01	0.04271(42)	0.52813(95)	0.8632(49)	0.918(11)	0.9122(85)	0.8654(53)
0.02	0.08415(95)	0.53752(65)	0.9021(37)	0.980(15)	0.9418(93)	0.9253(58)

Table 5.4: Meson masses measured along spatial direction with $32^3\times 8$ at $\beta = 0.49$ for eight flavors.

and m_π, and $t_{\text{min}} = 3$ for rest of the propagators. The results are in table 5.3 and 5.4. As the temperature increases from $N_\tau = 32$ to $N_\tau = 8$, meson masses, m_ρ, m_{ρ_2}, m_{a_1} and m_{b_1} increases. Recall at $N_\tau = 32$ zero temperature, f_π clearly extrapolate to non-zero values at chiral limit with linear ansatz. However at $N_\tau = 8$, the values of f_π linearly extrapolate to zero the same as $\langle\bar{\psi}\psi\rangle$ does, which is mentioned previously. In addition to the behavior of f_π at finite temperatures, the screening masses of the pion are also significantly different from those at zero temperature. This is shown in figure 5.3 and 5.4. At fixed β, N_τ is changed from 32 to 8, and a clear, dramatic change in the behavior of m_π with m_q is observed. Obviously, it is no longer a Goldstone boson.

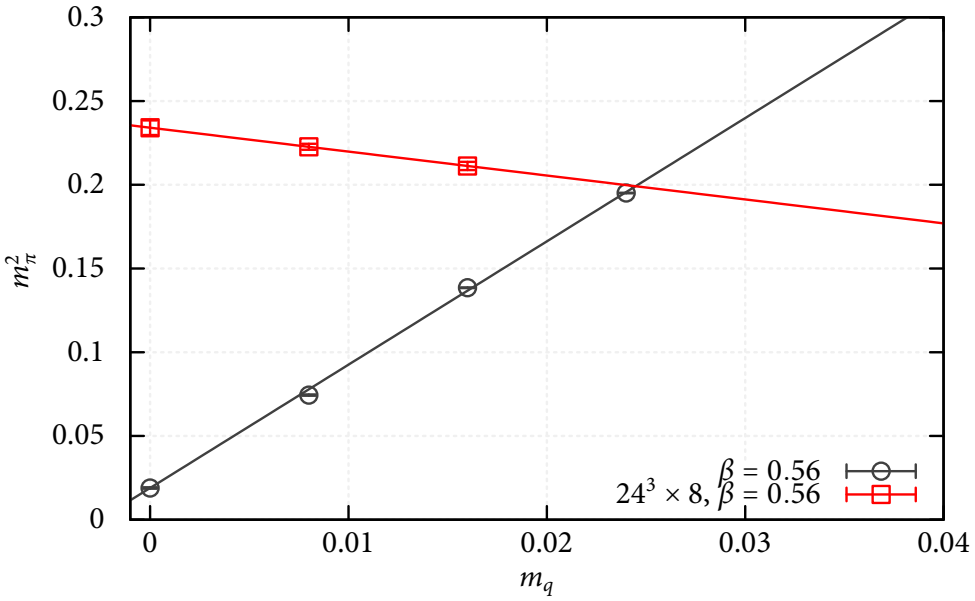

Figure 5.3: m_π^2 versus m_q with eight flavors at $N_\tau = 8$ and $N_\tau = 32$, $\beta = 0.56$, $m_q = 0.008$.

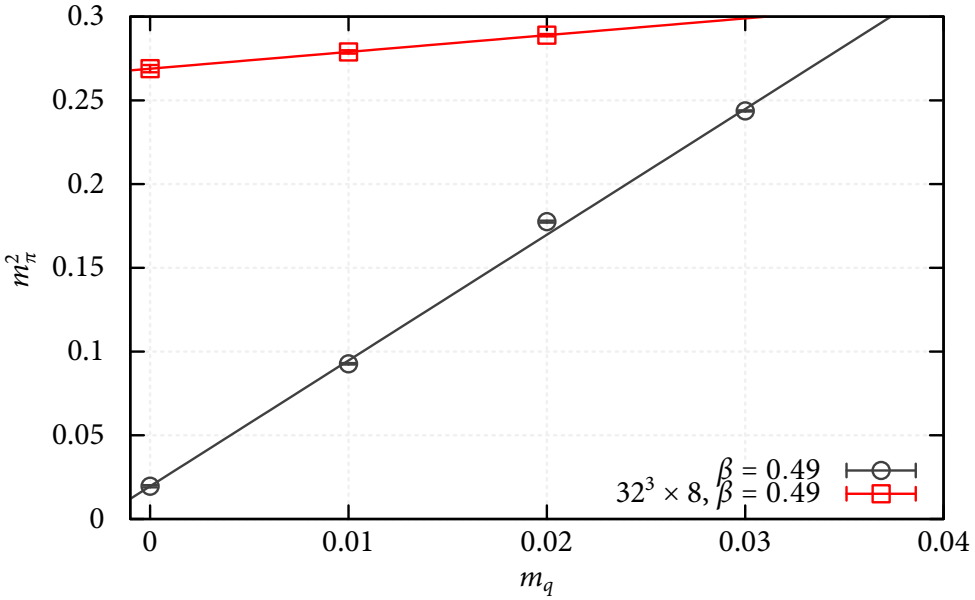

Figure 5.4: m_π^2 versus m_q with twelve flavors at $N_\tau = 8$ and $N_\tau = 32$, $\beta = 0.49$, $m_q = 0.008$.

The Wilson loops along the temporal direction have been measured for both N_τ

equals 8 and 32, as shown in table 5.5. The scatter plots of the real and imaginary parts of the Wilson loop along with the histograms of the real part are shown in figure 5.5, 5.6, 5.7 and 5.8. The histograms are normalized such that the height of each bar represents the percentage of the data points that is in the bin. It is clearly non zero at $N_\tau = 8$, and vanishes within errors for $N_\tau = 32$.

	$m_q = 0.008$		$m_q = 0.016$	
$N_f = 8$	$24^3\times 8$	$24^3\times 32$	$24^3\times 8$	$24^3\times 32$
	0.05717(50)	0.00013(19)	0.04738(42)	0.00013(23)
	$m_q = 0.01$		$m_q = 0.02$	
$N_f = 12$	$32^3\times 8$	$32^3\times 32$	$32^3\times 8$	$16^3\times 32$
	0.07642(28)	0.00020(13)	0.06799(18)	-0.00031(36)

Table 5.5: Real part of the unrenormalized Wilson loop.

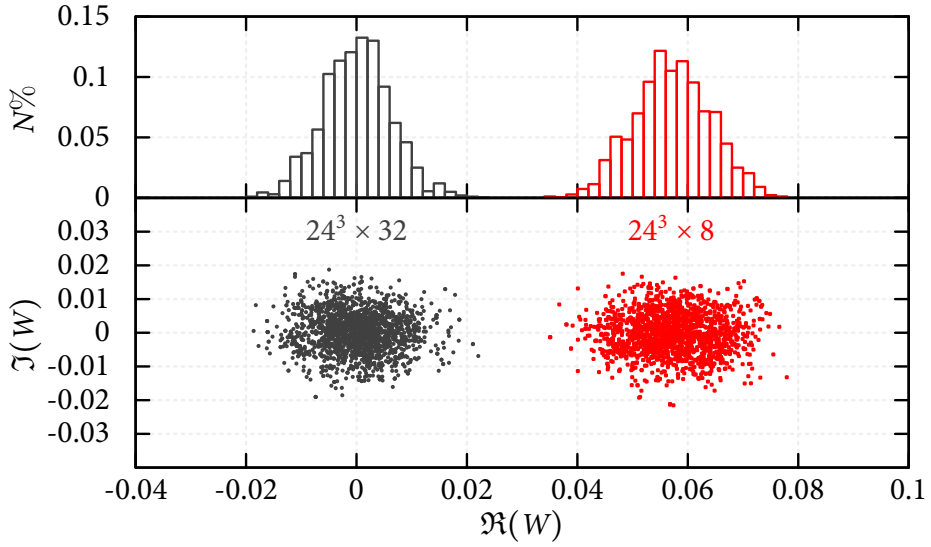

Figure 5.5: Wilson loop with eight flavors at $\beta = 0.56$, $m_q = 0.008$.

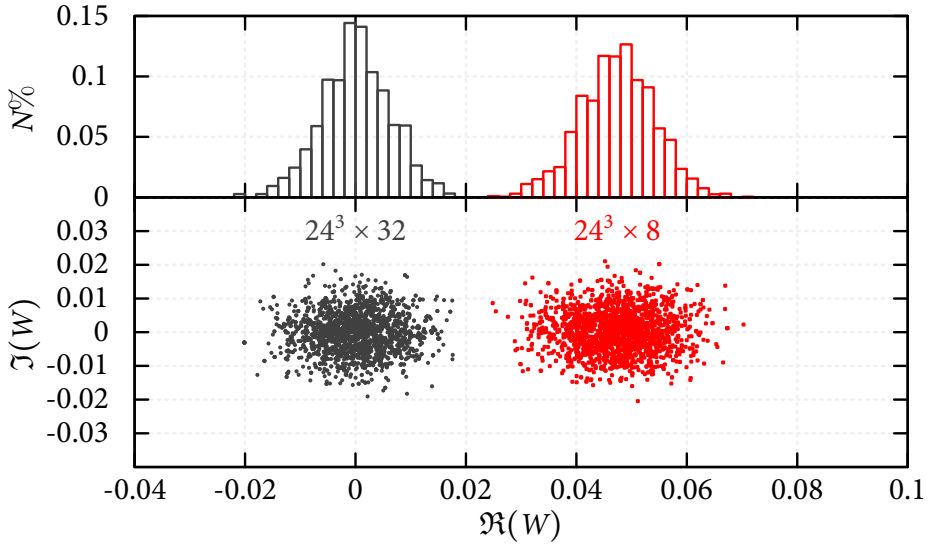

Figure 5.6: Wilson loop with eight flavors at $\beta = 0.56$, $m_q = 0.016$.

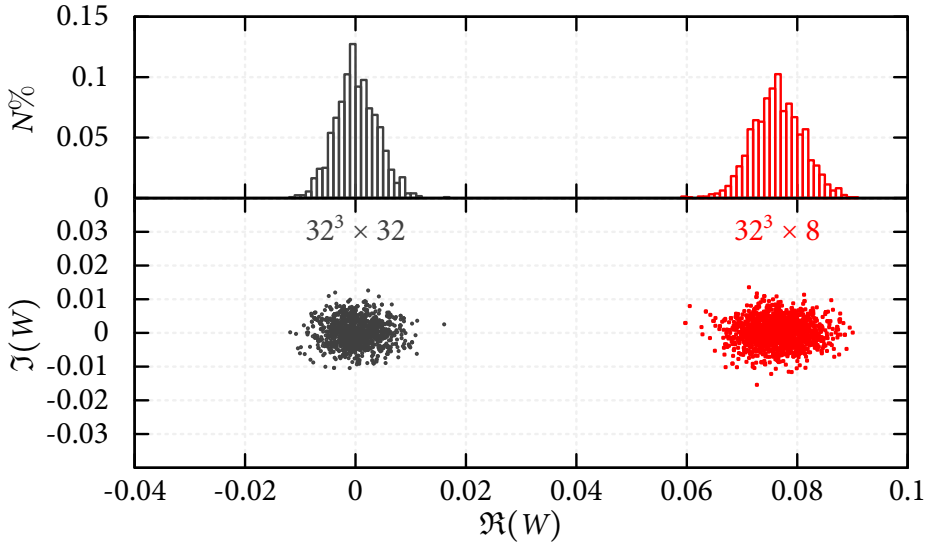

Figure 5.7: Wilson loop with twelve flavors at $\beta = 0.49$, $m_q = 0.01$.

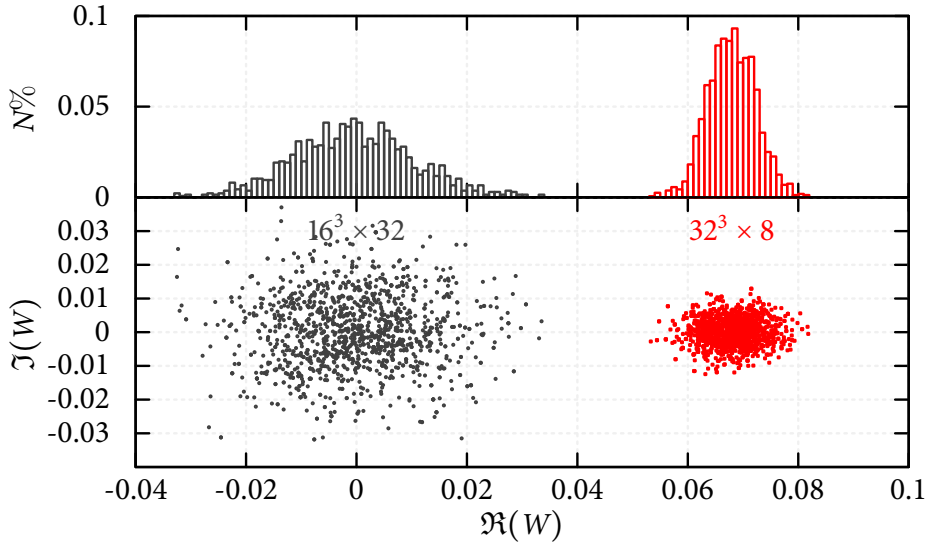

Figure 5.8: Wilson loop with twelve flavors at $\beta = 0.49$, $m_q = 0.02$.

The conclusion from the finite temperature studies is that there is a thermal transition taking place between $N_\tau = 8$ and $N_\tau = 32$ for both eight flavors and twelve flavors. This transition separates the zero temperature system with broken chiral symmetry with the finite temperature chirally symmetric system.

5.2 First Order Finite Temperature Phase Transition with Eight Flavors

Figure 5.9 shows the evolution of $\langle\bar{\psi}\psi\rangle$ at $\beta = 0.54$ and $N_\tau = 6$. By running with different quark masses, a metastability for nearly 4000 trajectories is seen at $m_q = 0.0195$ with a lattice size of $32^3\times6$. A discontinuity of $\Delta\langle\bar{\psi}\psi\rangle = 0.0416(20)$ at this quark mass has been found. Metastability is very sensitive to the quark mass; the quark mass has to be tuned to within 3% to see two co-existing states. A large spatial volume, 32^3 is also required,

as shown in the bottom panel of Figure 5.9, where the metastability is not apparent on a $16^3 \times 6$ volume.

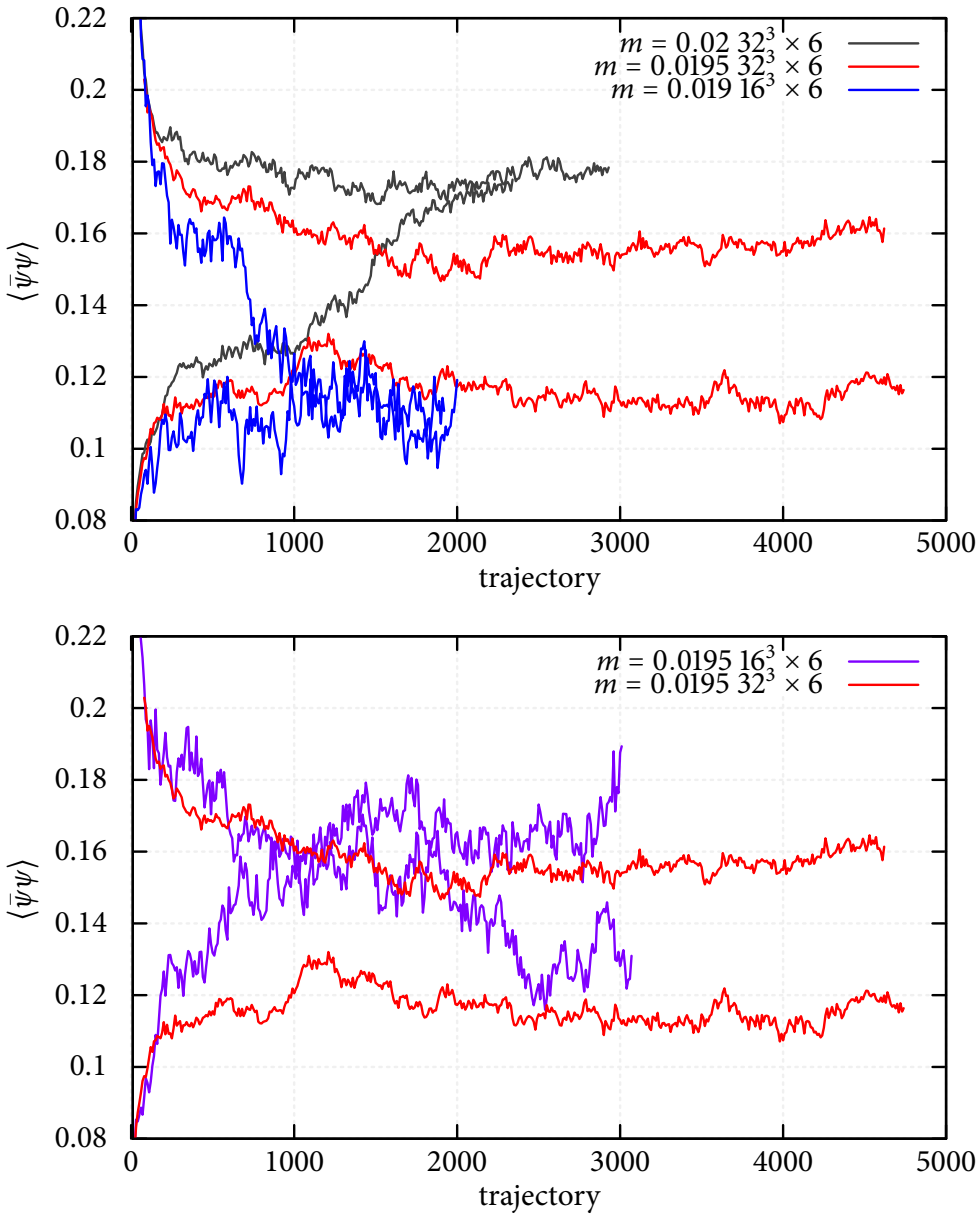

Figure 5.9: The evolution of $\langle\bar{\psi}\psi\rangle$, with both ordered (curves starting from bottom) and disordered starts (curves starting from top), using eight flavors at $\beta = 0.54$ and $N_\tau = 6$. The top panel shows the transition for 3 different masses. The bottom panel shows 2 different lattice volumes at the transition mass, $m_q = 0.0195$.

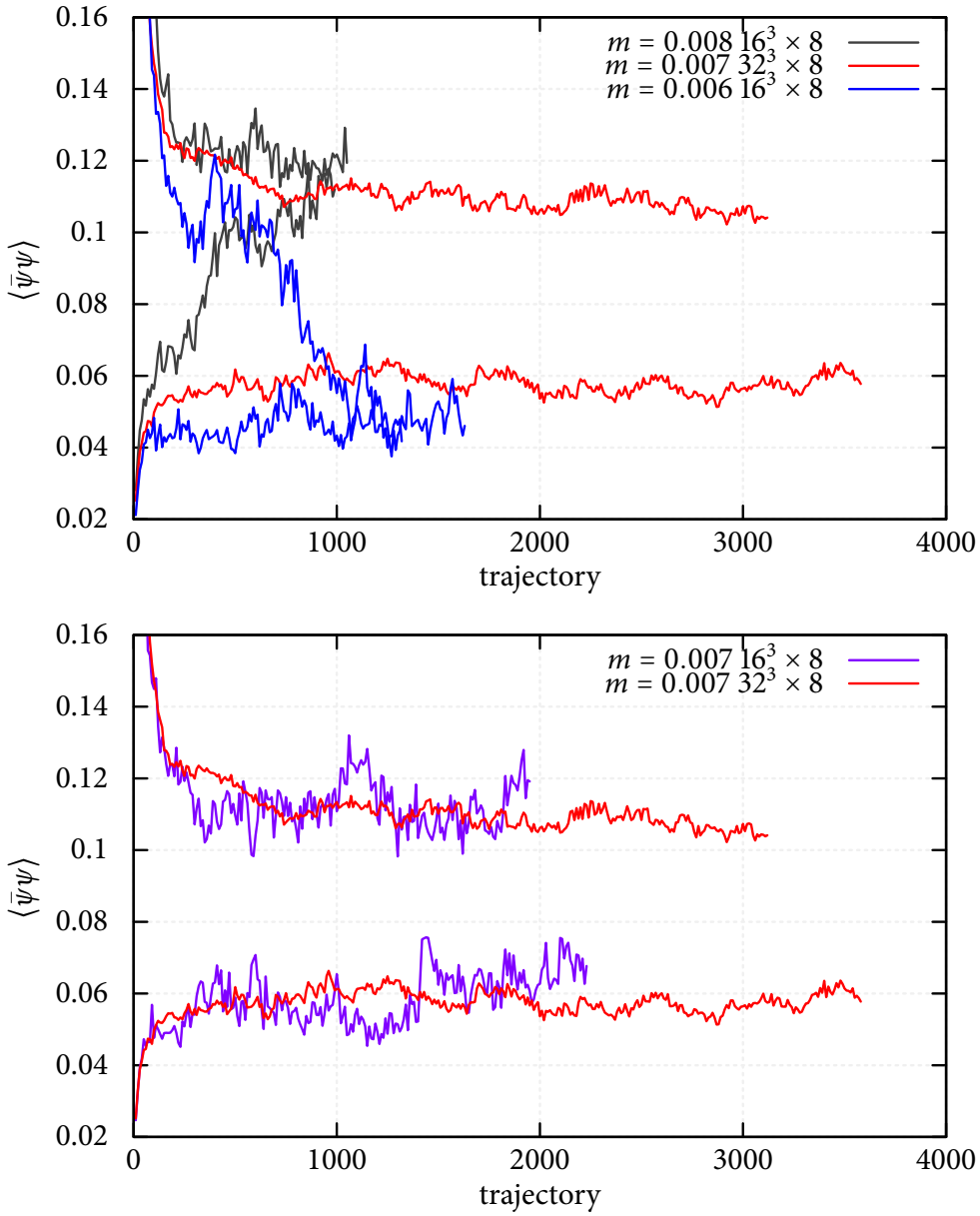

Figure 5.10: The evolution of $\langle\bar{\psi}\psi\rangle$ with both ordered (curves starting from bottom) and disordered starts (curves starting from top), using eight flavors at $\beta = 0.54$ and $N_\tau = 8$. The top panel shows the transition for 3 different masses. The bottom panel shows 2 different lattice volumes at the transition mass, $m_q = 0.007$.

For $N_\tau = 8$, shown in Figure 5.10, metastability is seen at a much smaller quark mass,

$m_q = 0.007$, for more than 2000 trajectories. The first order signal is stronger, with a discontinuity $\Delta\langle\bar{\psi}\psi\rangle = 0.0508(17)$. The quark mass is tuned within 15%. And both 16^3 and 32^3 volumes are clearly metastable.

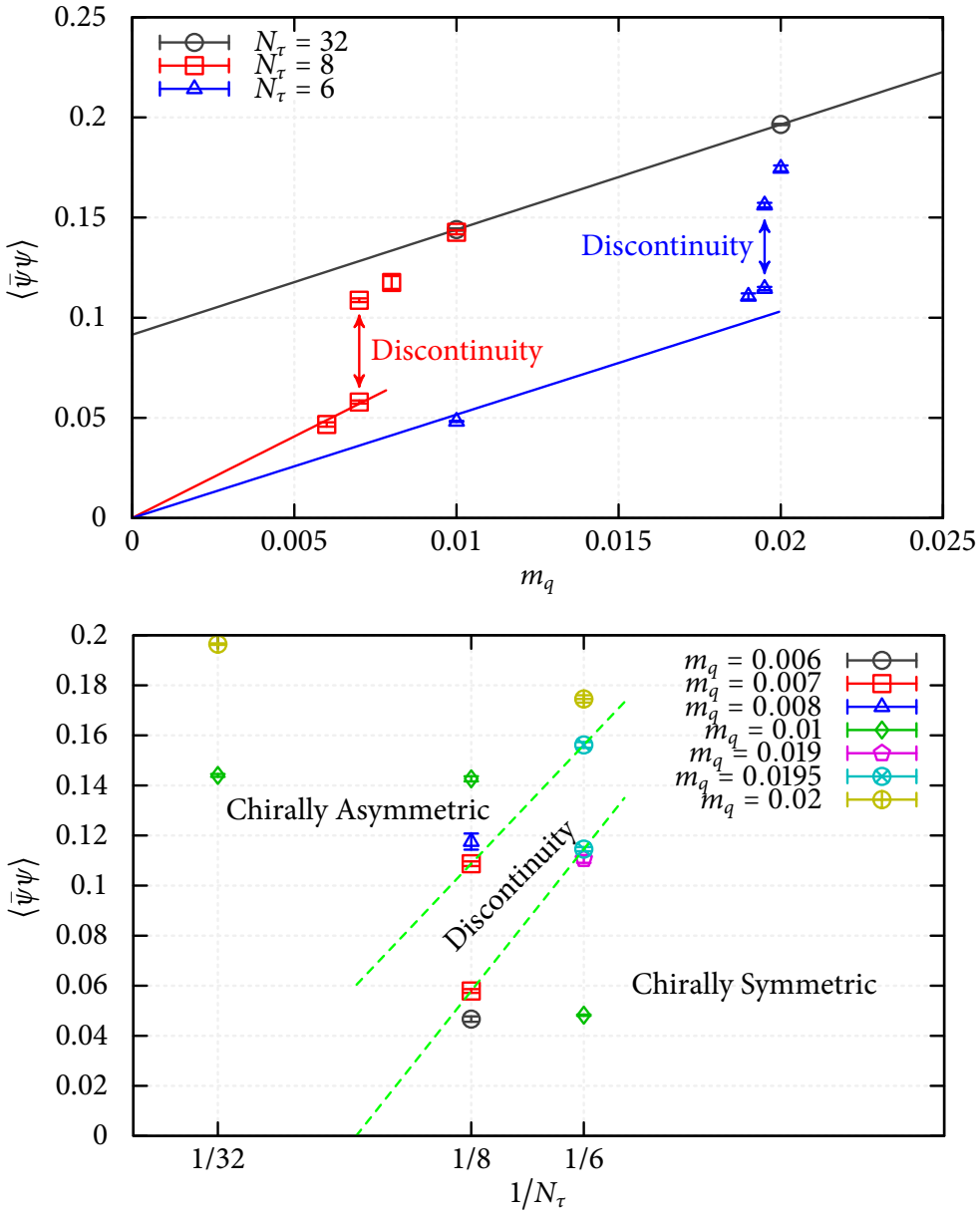

Figure 5.11: A diagram showing the values of $\langle\bar{\psi}\psi\rangle$ at $\beta = 0.54$ with the discontinuity due to the first order phase transition explicitly shown. The top panel shows $\langle\bar{\psi}\psi\rangle$ versus m_q and the bottom panel shows $\langle\bar{\psi}\psi\rangle$ versus temperature ($1/N_\tau$).

The chiral symmetry restoration transition is revealed in the two diagrams for eight flavors at $\beta = 0.54$ in Figure 5.11. The upper panel shows the value of $\langle\bar{\psi}\psi\rangle$ at different

temperatures while varying the quark mass. The top line shows a linear extrapolation of $\langle\bar{\psi}\psi\rangle$ at $N_\tau = 32$ to the chiral limit. The discontinuity separates the chirally broken phase (upper points) and the chirally symmetric phase (lower points). The two lower lines, for $N_\tau = 8$ and $N_\tau = 6$, which have slopes of 8.14 and 5.16 respectively, are linear fits to $\langle\bar{\psi}\psi\rangle$ in the chirally symmetric phase. They are forced to go to the origin, which is the expected behavior of $\langle\bar{\psi}\psi\rangle$ at finite temperature. The fit at $N_\tau = 6$ has a much larger χ^2/dof (about 260) than the fit at $N_\tau = 8$ (about 5). This can be seen as a sign of weakened first order signal due to the relatively large fermion mass. The lower panel of Figure 5.11 is another way of visualizing the phase diagram. The two dashed lines are linear fits to the metastable signal of $\langle\bar{\psi}\psi\rangle$ at the edge of chirally broken phase (upper left region), which has a slope of 1.14, and the edge of chirally symmetric phase (lower right region), which has a slope of 1.36. In between is the inaccessible discontinuity region of $\langle\bar{\psi}\psi\rangle$.

m_q	0.007	0.0195
$m_\pi(m_q)/f_\pi(m_q)$	1.665(15)	2.047(8)
$T_c(m_q)/f_\pi(m_q)$	0.819(47)	0.890(14)

Table 5.6: The critical temperature, $T_c(m_q)$, of the first order, chiral symmetry restoring, finite temperature phase transition with eight flavors, as observed at bare coupling $\beta = 0.54$.

Table 5.6 displays the critical temperature, $T_c(m_q)$, in units of $f_\pi(m_q)$. The values of $f_\pi(m_q)$ and $m_\pi(m_q)$ come from naive extrapolations of zero temperature results, where $m_\pi^2 \propto m_q$ and $f_\pi \propto m_q$. The quoted errors of m_π/f_π are only statistical errors. The errors quoted for T_c/f_π uses error propagation from the error of the linear extrapolation of f_π and the estimated error of T_c that is described in the following. First, the error can be estimated in the determination of m_q at the transition point from the range of quark masses which either do or do not show metastability. This gives a quark mass uncertainty of 0.001 for $N_\tau = 8$ and 0.0005 for $N_\tau = 6$. At the edge of the chirally symmetric phase,

using the two fits in the top panel of Figure 5.11, this uncertainty in m_q can be translated to an uncertainty in $\langle\bar{\psi}\psi\rangle$ of 0.00814 and 0.00258 at $N_\tau = 8$ and 6 respectively. These values can be further converted to an uncertainty on T_c by the relation of $\langle\bar{\psi}\psi\rangle$ and T_c at the edge of chirally symmetric phase which is represented by the lower dashed line in the lower panel of Figure 5.11. This procedure results in estimated errors on T_c of 0.00599 and 0.00190 at $N_\tau = 8$ and 6 respectively.

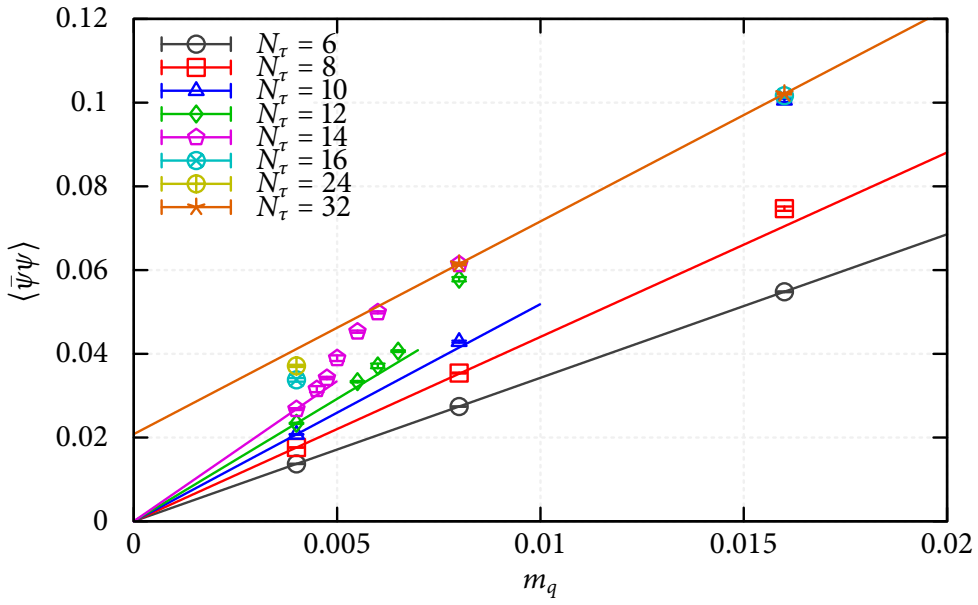

Figure 5.12: The values of $\langle\bar{\psi}\psi\rangle$ versus m_q for eight flavors at $\beta = 0.56$. The first order transition point cannot be resolved numerically with current simulations.

At weaker coupling, $\beta = 0.56$, where the lattices are much finer than those at $\beta = 0.54$, no clear signal of a first order transition has been found. Figure 5.12 shows a survey of the parameter space covered in the simulation. Among those points, for $m_q \leq 0.008$ and $N_\tau \neq 32$, the spatial volume of the lattices are 32^3. Similar to the previous figure, the line at $N_\tau = 32$ is a linear extrapolation of $\langle\bar{\psi}\psi\rangle$ at zero temperature. The lines drawn through the origin denote the m_q dependence of $\langle\bar{\psi}\psi\rangle$ at finite temperature. A careful scan in

various quark masses is done to search for a possible discontinuity of $\langle\bar{\psi}\psi\rangle$, for $N_\tau = 14$. Since the discontinuity in $\langle\bar{\psi}\psi\rangle$ is expected to be markedly smaller here than for $\beta = 0.54$, the focus has been on larger N_τ and smaller quark masses. Fixing $N_\tau = 14$ and tuning the quark mass, a clear metastability signal could not be found like the ones seen at stronger coupling, $\beta = 0.54$. The evolutions of $\langle\bar{\psi}\psi\rangle$ around $m_q = 0.005$ at $N_\tau = 14$ are shown in Figure 5.13. In this figure, the evolution of $\langle\bar{\psi}\psi\rangle$ at $m_q = 0.005$ is very noisy, similar to the one in Figure 5.9, at $\beta = 0.54$, $m_q = 0.007$ with a lattice size of $16^3\times 6$. It is a good indication that the critical point of the transition is near, but either a much larger lattice spatial volume is required to produce metastable states or the quark mass is large enough so that the first order transition has almost weakened to become second order.

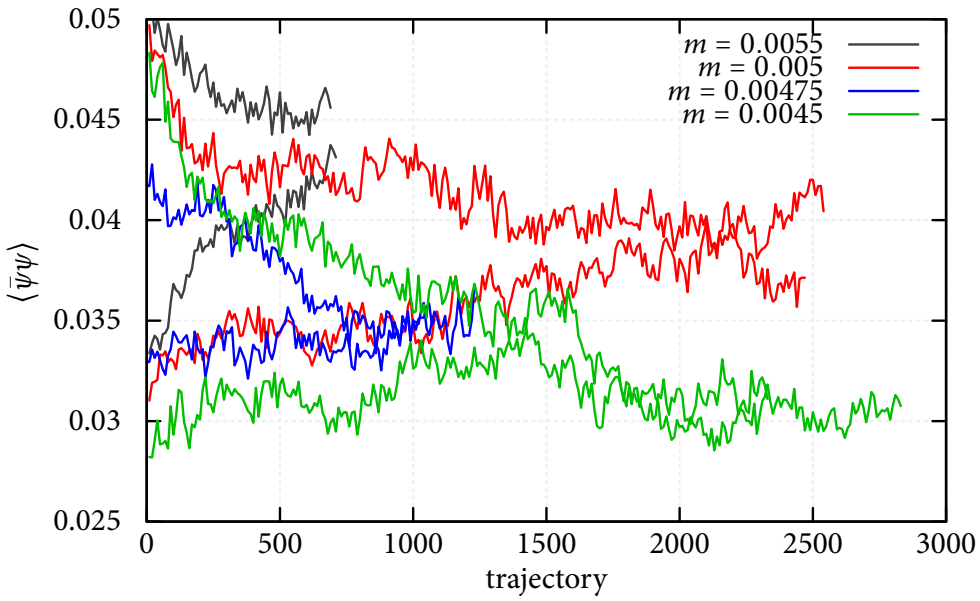

Figure 5.13: Evolutions of $\langle\bar{\psi}\psi\rangle$ with ordered and disordered starts at $N_\tau = 14$, $\beta = 0.56$.

Chapter 6

Bulk Transition at Zero Temperature

6.1 Bulk Transition with Eight Flavors

With eight flavors, an earlier study [74] using naive staggered fermions, the Wilson gauge action and R algorithm has revealed a bulk transition. At lattice coupling $\beta = 4.65$ and 4.60, where metastability was observed in the earlier study with R algorithm, simulations using both R algorithm with two different step sizes and RHMC algorithm have been performed. (Note: The convention of step size in R algorithm in current software may be different from the one used in the earlier study.) Figure 6.1 and figure 6.2 shows the evolution of $\langle\bar{\psi}\psi\rangle$ at $\beta = 4.65$ with both ordered and disordered start. Metastability is observed using the R algorithm with a step size of 0.00625. It went away when the same R algorithm was used but with half of the previous step size. The simulation using the RHMC algorithm shows consistency with the one using R algorithm with the step size of 0.003125. At a stronger coupling $\beta = 4.60$, figure 6.3 shows that, after about 400 trajectories of thermalization time, the ordered and disordered evolutions using R algorithm with step sizes of both 0.005 and 0.003125 stabilized at different values of $\langle\bar{\psi}\psi\rangle$,

thus exhibit the bulk transition signal. However, the evolutions using RHMC algorithm show no tendency of metastability, despite the fact that the ordered and disordered starts are not thermalized even after 800 trajectories. It is striking to see that there is such a large error associated with step size in R algorithm in the disordered start that it produced a phony metastability.

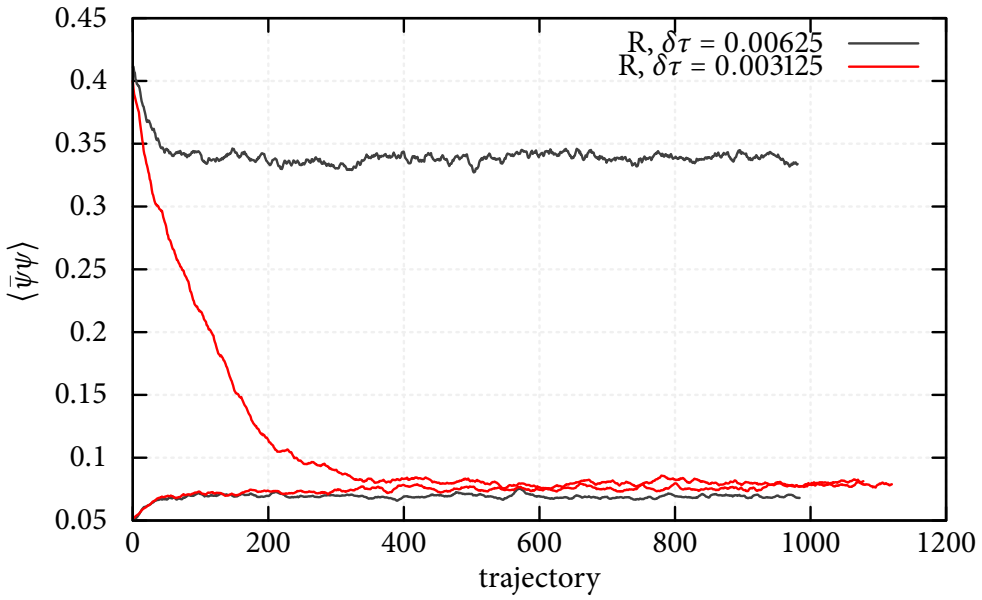

Figure 6.1: Evolutions of $\langle\bar{\psi}\psi\rangle$ with eight quark flavors, Wilson gauge and naive staggered fermion, at $\beta = 4.65$ and $m_q = 0.015$, and a lattice volume of $16^3\times 32$, with R algorithm. Two different step sizes are used, $\delta\tau = 0.00625$ (the two black lines separate from each other apart) and $\delta\tau = 0.003125$ (the two red lines merges together after about 350 trajectories). Within the evolution of the same step size, upper curve is from disordered start and lower curve is from ordered start. The value of $\langle\bar{\psi}\psi\rangle$ is measured at the end of each trajectory, and the data plotted are the simple moving average of nearest 10 measurements.

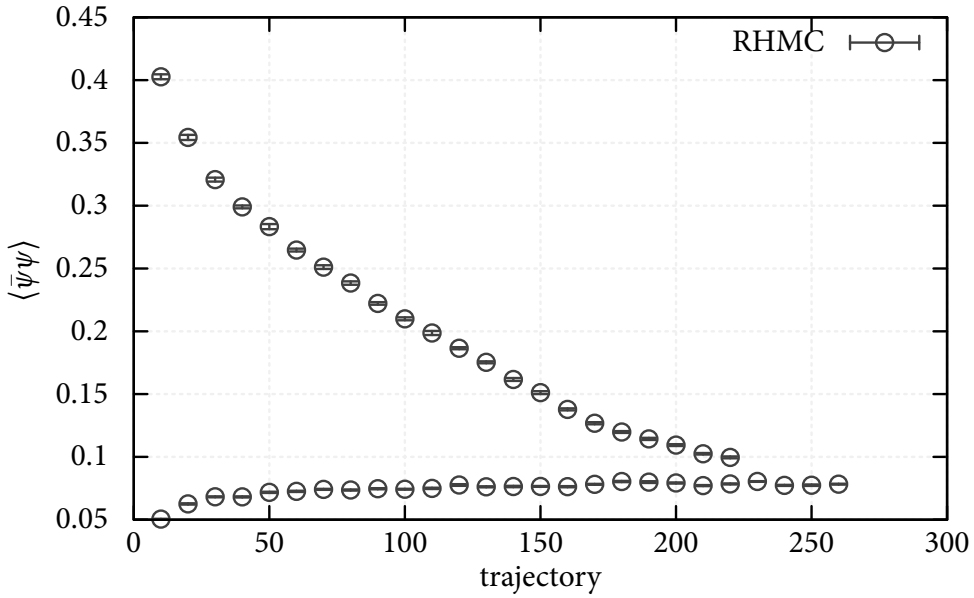

Figure 6.2: Evolutions of $\langle\bar{\psi}\psi\rangle$ with eight quark flavors, Wilson gauge and naive staggered fermion, at $\beta = 4.65$ and $m_q = 0.015$, and a lattice volume of $16^3 \times 32$, with RHMC algorithm. It behaves similar to the one with R algorithm with a smaller step size ($\delta\tau = 0.003125$). Upper curve is from disordered start and lower curve is from ordered start. The value of $\langle\bar{\psi}\psi\rangle$ is measured ten times at the end of every tenth trajectory.

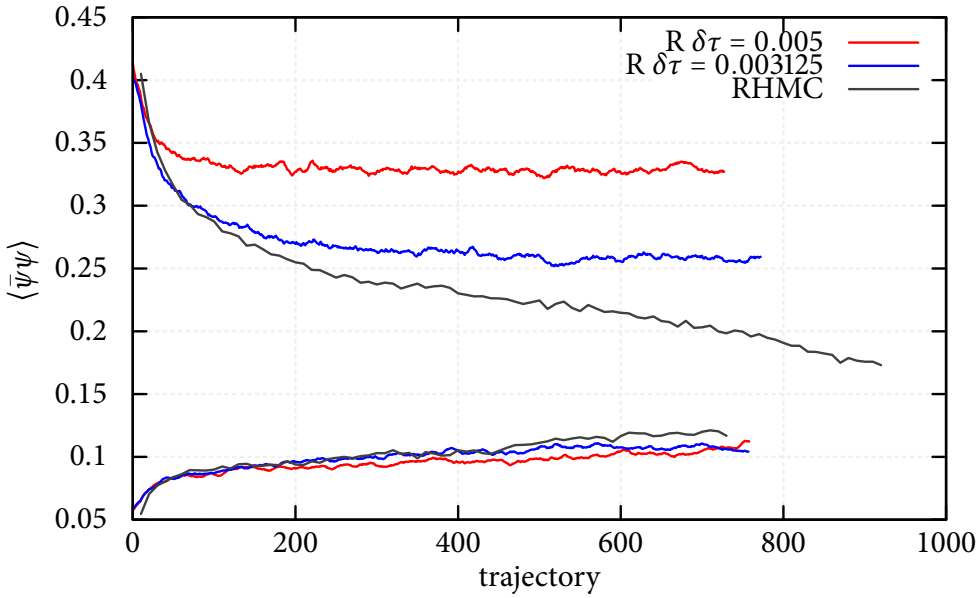

Figure 6.3: Comparison of R and RHMC algorithms on the evolutions of $\langle\bar{\psi}\psi\rangle$ with eight quark flavors, Wilson gauge and naive staggered fermion, at $\beta = 4.60$ and $m_q = 0.015$. Two different step sizes are used with R algorithm. Within the same algorithm, upper curve is from disordered start and lower curve is from ordered start. The value of $\langle\bar{\psi}\psi\rangle$ is measured at the end of each trajectory in the evolution with R algorithm and the data plotted are the simple moving average of nearest 10 measurements, while in the evolution of RHMC algorithm, it is measured ten times at the end of every tenth trajectory.

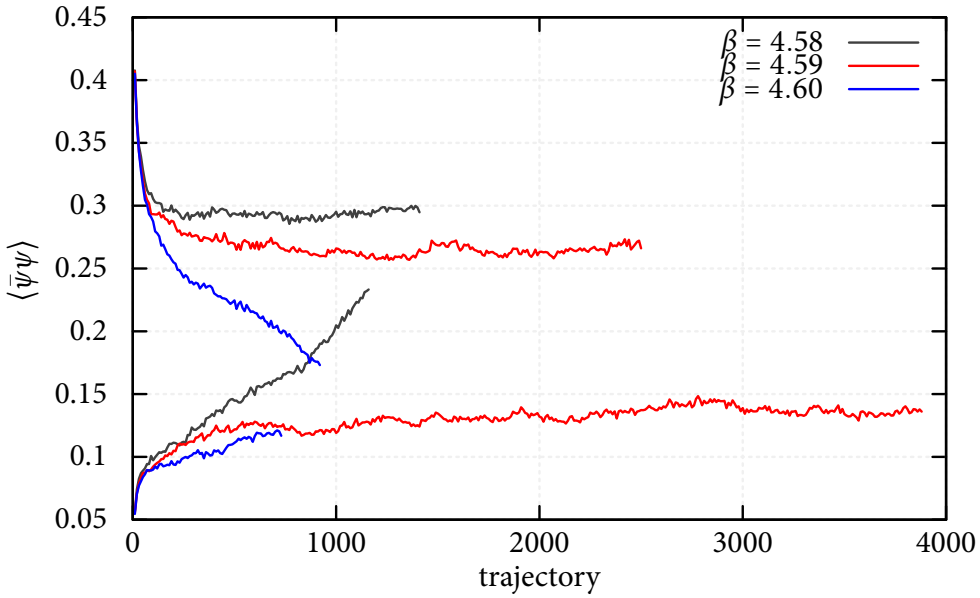

Figure 6.4: Evolutions of $\langle\bar{\psi}\psi\rangle$ with eight quark flavors, using RHMC algorithm, Wilson gauge and naive staggered fermion, at $m_q = 0.015$. The curves with low values at the beginning of the evolutions are ordered start, while the curves with high values at the beginning of the evolutions are disordered start. Within the same kind of start, the values of input coupling are $\beta = 4.58$, 4.59 and 4.60 from top to bottom.

Nevertheless, a bulk transition is found at $\beta = 4.59(1)$, using RHMC algorithm, as shown in figure 6.4. At $\beta = 4.59$, ordered and disordered starts thermalized after around 1500 trajectories, and depict the bulk transition. This is consistent with the earlier study [74].

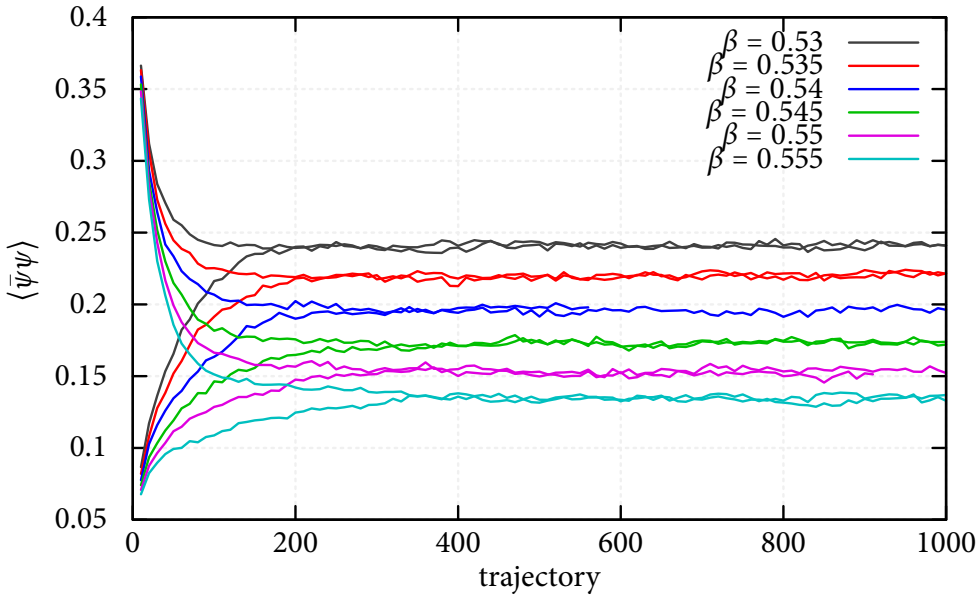

Figure 6.5: Evolution of ordered (lower curve) and disordered (upper curve) start, with $m_q = 0.02$ and a lattice size of $16^3 \times 32$, using DBW2 gauge action. The figure shows $\langle \bar{\psi}\psi \rangle$ for (from top to bottom) $\beta = 0.53, 0.535, 0.54, 0.545, 0.55, 0.555$.

Such a bulk transition was not observed with DBW2 gauge action for eight flavors. Figure 6.5 shows a series of simulations with β varies from 0.53 to 0.555 and input quark mass $m_q = 0.02$, which cover most part of strong coupling region and result in a large range of $\langle \bar{\psi}\psi \rangle$ values. No evidence of metastability is shown in that region.

6.2 Bulk Transition with Twelve Flavors

If the QCD system with twelve flavors is similar to the system with eight flavors, a zero-temperature bulk transition with twelve flavors is expected to exist at places comparable to where the eight-flavor bulk transition appears. In deed, the bulk transition was found, see figure 6.6, with naive staggered fermion and Wilson plaquette action at $\beta = 4.1$ and $m_q = 0.01$. A lattice size of $16^3 \times 32$ is used in searching for the transition.

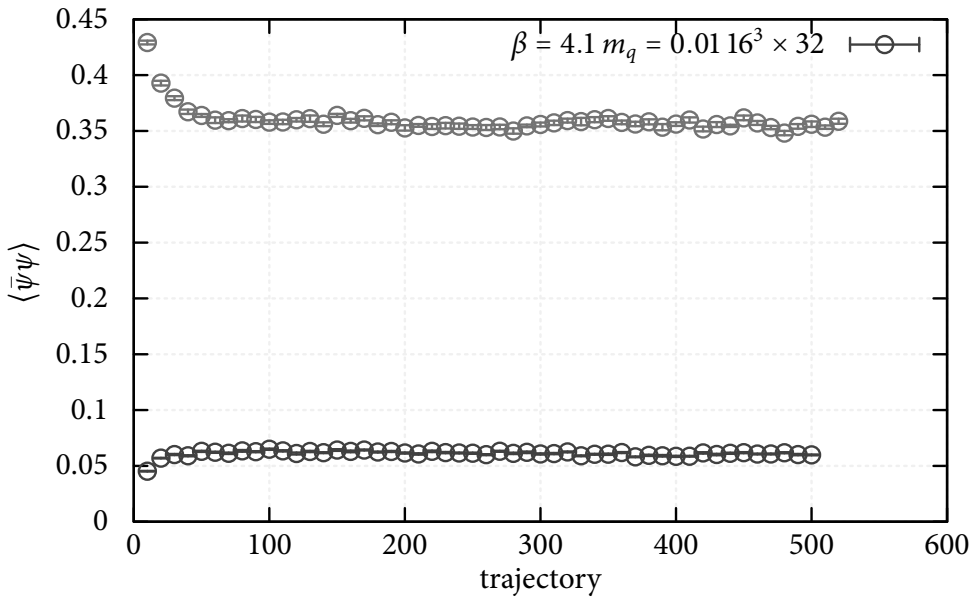

Figure 6.6: Evolution of $\langle\bar{\psi}\psi\rangle$ with naive staggered fermion and Wilson plaquette gauge at $\beta = 4.1$ and $m_q = 0.01$, with a lattice size of $16^3 \times 32$. The ordered start (bottom curve) and disordered start (top curve) are well separated.

As shown and discussed previously, there is only a rapid cross-over in the twelve-flavor system with $m_q \geq 0.01$ on the lattice with naive staggered fermion and DBW2 gauge. This brings one more similarity between system with eight flavors and system with twelve flavors, as the DBW2 action seems to replace the bulk transition, which appears with Wilson plaquette gauge action, with a cross-over region, at quark masses with $m_q \geq 0.01$.

However, as the quark masses becomes smaller, the bulk transition does appear in lattice simulations of twelve flavors with naive staggered fermions and the DBW2 gauge action. Figure 6.7 and figure 6.8 show the metastable lattice evolution of $\langle\bar{\psi}\psi\rangle$. Figure 6.7 shows the ensemble at $\beta = 0.46$ and $m_q = 0.006$, and figure 6.8 shows the ensemble at $\beta = 0.4626$ and $m_q = 0.008$. The differences of $\langle\bar{\psi}\psi\rangle$ value across the bulk transition shrinks, while the quark mass increases from $m_q = 0.006$ to $m_q = 0.008$. It is reasonable

to believe that this bulk transition ends at somewhere near $m_q \sim 0.01$ with a second order critical point. This is the cause of the rapid cross-over at $m_q \gtrsim 0.01$.

The bulk transition observed here does not appear depend on the lattice volume. As in figure 6.7 and 6.8, although the size of the lattice changes from $16^3 \times 32$ to $24^3 \times 32$, the position of the bulk transition and the value of $\langle \bar{\psi}\psi \rangle$ barely changes. Therefore, the bulk transition is not a finite volume effect. This, in turn, can remove the possibility of a thermal transition. The length of the shortest dimension of the lattice can be roughly equal to the temperature, baring the difference of lattice boundary condition. As the "temperature" rises 50%, the location of the bulk transition barely changes.

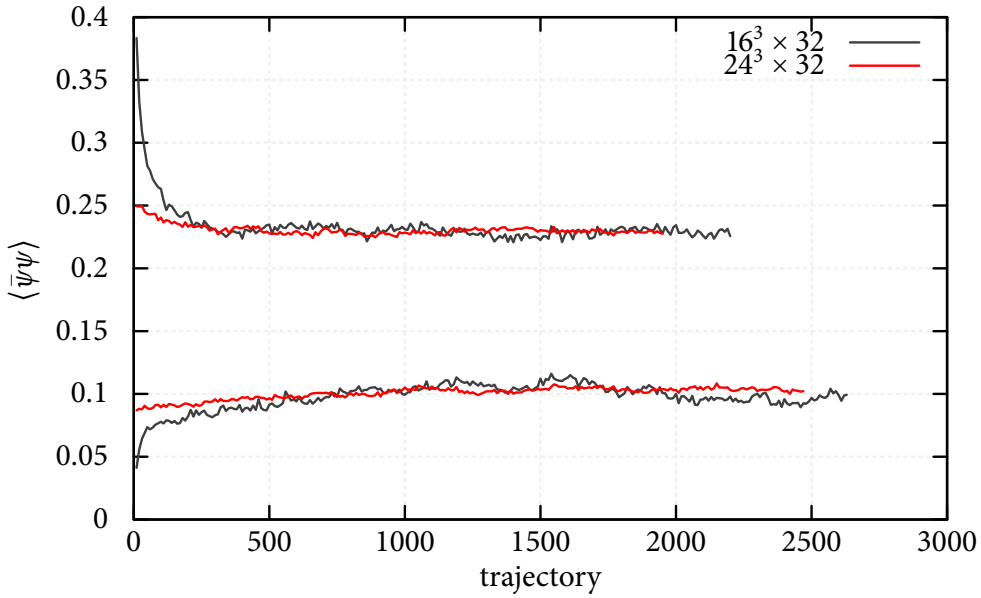

Figure 6.7: Evolution of $\langle \bar{\psi}\psi \rangle$ with naive staggered fermion and DBW2 gauge at $\beta = 0.46$ and $m_q = 0.006$. Both $16^3 \times 32$ and $24^3 \times 32$ lattices are shown to have metastability. The ordered starts (bottom curves) and disordered starts (top curves) are well separated.

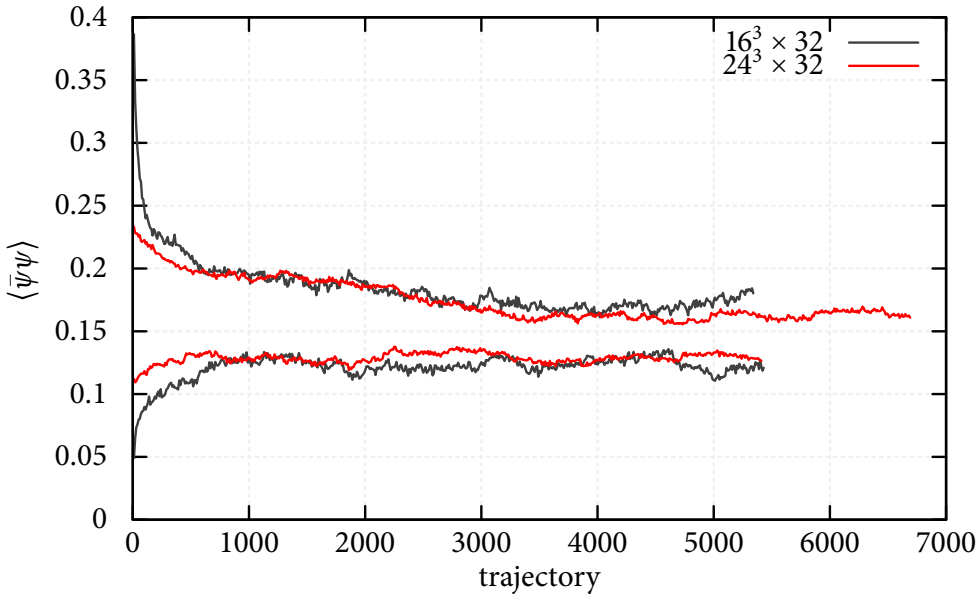

Figure 6.8: Evolution of $\langle\bar{\psi}\psi\rangle$ with naive staggered fermion and DBW2 gauge at $\beta = 0.4626$ and $m_q = 0.008$. Both $16^3 \times 32$ and $24^3 \times 32$ lattices are shown to have metastability. The ordered starts (bottom curves) and disordered starts (top curves) are well separated.

A selection of lattice ensembles simulated are listed in table 6.1, with the $\langle\bar{\psi}\psi\rangle$ and plaquette listed in table 6.2. The blocking size of 80 trajectories have been used similar to previous zero-temperature data, except for some ensembles with short trajectories, which are indicated in the table. The positions of the bulk transition are explicitly marked with "ordered" or "disordered", which is the start type of the lattice simulations.

Figure 6.9 shows most of the $\langle\bar{\psi}\psi\rangle$ values for the simulated ensembles. Two linear fits are shown in the figure at the weak coupling side of the transition. One is for the three mass points at $\beta = 0.49$, and the other for the lowest two mass points $m_q = 0.003$ and 0.004 at $\beta = 0.46$. Although the extrapolated value at the massless quark limit is small, it is however non-zero. It corresponds to a small change in the lattice scale from $\beta = 0.46$ to $\beta = 0.49$, which can be explicitly seen in the figure 6.10, where some selected values of f_π are shown.

β	m_f	Size	Trajectories	$e^{-\Delta H}$	acceptance
0.45	0.0025	$32^3\times32$	900-1170*	0.96(18)	0.380(24)
	0.005	$24^3\times32$	310-660^{*d}	0.966(62)	0.733(41)
0.46	0.003	$24^3\times32$	570-4480	0.9986(54)	0.8496(25)
		$32^3\times32$	1040-4470	1.009(12)	0.7792(39)
	0.004	$24^3\times32$	1010-4360	1.0027(74)	0.8115(37)
	0.005	$16^3\times32$	530-2080	0.975(17)	0.753(13)
		$24^3\times32$	1850-4160	1.013(16)	0.7391(58)
	0.006 ordered	$16^3\times32$	1360-2630	1.013(15)	0.8288(73)
		$24^3\times32$	1040-2470	0.999(19)	0.8079(72)
	0.006 disordered	$16^3\times32$	1210-2200^4	1.011(14)	0.8168(60)
		$24^3\times32$	520-1950	0.993(30)	0.676(10)
	0.0075	$24^3\times32$	310-480^{*d}	0.971(49)	0.798(18)
0.4626	0.008 ordered	$16^3\times32$	2000-5430	0.983(16)	0.690(12)
		$24^3\times32$	1020-5410	0.9854(74)	0.8081(36)
	0.008 disordered	$16^3\times32$	3510-5340	1.034(23)	0.6350(86)
		$24^3\times32$	3500-6690	0.9996(61)	0.8541(27)

Table 6.1: Parameters and ensemble properties of simulations for twelve flavors with quark masses $m_q < 0.01$. The provided number of "Trajectories" are those trajectories used for measurements and analysis. No blocking is used with the ensemble labeled with *, and blocking size of 40 trajectories is used with the ensemble labeled with ^{4}. The ensemble labeled with ^{d} is disordered start.

β	m_f	Size	$\langle\bar{\psi}\psi\rangle$	plaquette
0.45	0.0025	$32^3\times32$	0.30035(31)	0.444732(22)
	0.005	$24^3\times32$	0.30983(27)	0.442475(33)
0.46	0.003	$24^3\times32$	0.04639(19)	0.493119(10)
		$32^3\times32$	0.046152(97)	0.4931419(64)
	0.004	$24^3\times32$	0.05980(15)	0.492562(13)
	0.005	$16^3\times32$	0.07398(32)	0.491809(29)
		$24^3\times32$	0.07727(28)	0.491575(21)
	0.006 ordered	$16^3\times32$	0.1006(15)	0.48978(15)
		$24^3\times32$	0.10352(32)	0.489515(33)
	0.006 disordered	$16^3\times32$	0.22804(48)	0.47002(10)
		$24^3\times32$	0.22901(35)	0.469933(79)
	0.0075	$24^3\times32$	0.25302(46)	0.464840(68)
0.4626	0.008 ordered	$16^3\times32$	0.12328(68)	0.489835(81)
		$24^3\times32$	0.12921(44)	0.489100(54)
	0.008 disordered	$16^3\times32$	0.17054(92)	0.48321(15)
		$24^3\times32$	0.16229(43)	0.484496(64)

Table 6.2: The averaged plaquette value and $\langle\bar{\psi}\psi\rangle$ from simulations for twelve flavors with $m_q < 0.01$ near the bulk transition.

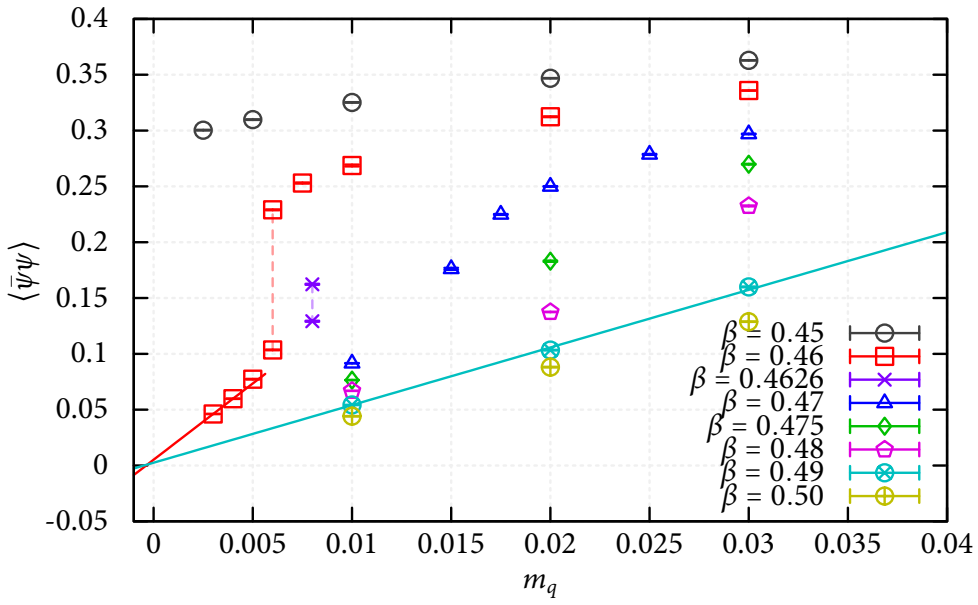

Figure 6.9: The complete picture of $\langle\bar{\psi}\psi\rangle$ of lattice simulations with twelve flavors. Two bulk transitions are indicated with dashed lines. Two linear fits are performed, one at $\beta = 0.46$ through $m_q = 0.003$ and 0.004; the other at $\beta = 0.49$ through $m_q = 0.01$, 0.02 and 0.03.

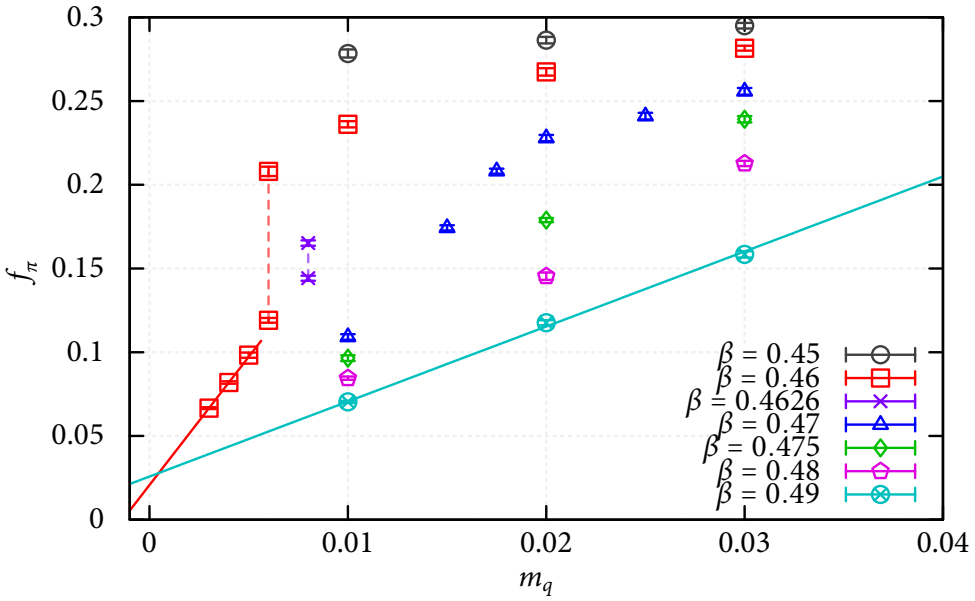

Figure 6.10: Some selected values of f_π showing the change of lattice scale change in lattice simulations with twelve flavors. The bulk transition is indicated with dashed lines. Two linear fits are performed, one at $\beta = 0.46$ through $m_q = 0.003$ and 0.004; the other at $\beta = 0.49$ through $m_q = 0.01$, 0.02 and 0.03.

The meson spectrum is measured near the transition, following the same procedure laid out in section 4.2. The values of t_{min} for two-state fits are given in table 6.3, and the resulting mass spectrum is shown in tables 6.4 and 6.5, where the notation is the same as in section 4.2 and was discussed there. The finite volume effect is indeed small, which can be seen by comparing the meson masses measured on two different volumes at $m_q = 0.005$ and $m_q = 0.003$. The results, at input quark mass $m_q = 0.003$, measured from $24^3\times32$ and $32^3\times32$ deviate within 3σ. There is a roughly 1.6× change in lattice scale across the bulk transition at the finite quark mass $m_q = 0.006$, which can be seen from the masses at two sides of the bulk transition. This translates to around $1.6^2 \simeq 2.5\times$ change in the values of $\langle\bar{\psi}\psi\rangle$ seen in table 6.2 at finite quark mass $m_q = 0.006$.

m_q	0.003	0.004	0.005	0.006 ordered	0.006 disordered
$\beta = 0.46$	5	5	5	3	1

Table 6.3: t_{min} for double states spectrum fit with twelve flavors near the bulk transition.

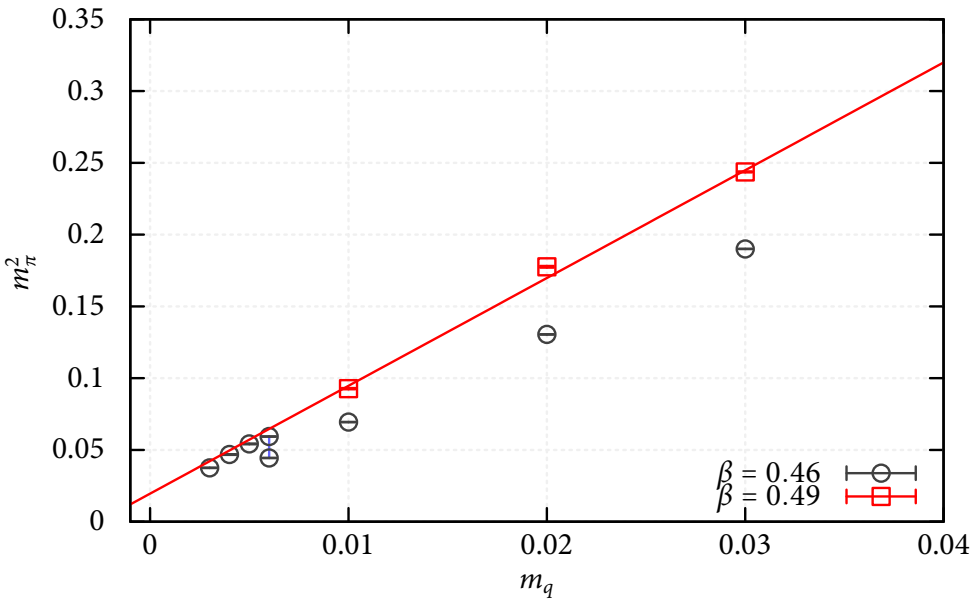

Figure 6.11: Values of m_π^2 versus input quark mass m_q, at $\beta = 0.46$ and $\beta = 0.49$. The bulk transition can be seen at $m_q = 0.006$. A linear fit through three points at $\beta = 0.49$ is shown.

A good confirmation of spontaneous chiral symmetry breaking again comes from the linearity of $m_\pi^2 \propto m_q$, shown in figure 6.11. To improve clarity, only a linear fit through the three points at $\beta = 0.49$ is shown. Nevertheless, it can be seen, clearly from these points at $\beta = 0.46$, that the system obtains good linearity of $m_\pi^2 \propto m_q$ not only in the strong coupling side $m_q \gtrsim 0.01$ of the bulk transition, but also in the weak coupling side $m_q \lesssim 0.005$ of the bulk transition. This behavior is distinct from the usual finite temperature transition (*cf.* figure 5.4), through which chiral symmetry restores.

The masses of ρ and a_1 from the weak coupling side of the bulk transition can be compared with the results discussed previously. The values measured from the weak

m_q	Size	f_π	m_π	m_{π_2}	m_ρ
0.003	$24^3\times32$	0.06782(74)	0.19462(42)	0.323[25]	0.4458(41)
	$32^3\times32$	0.06661(54)	0.19370(33)	0.335[17]	0.4338(34)
0.004	$24^3\times32$	0.08192(71)	0.21633(53)	0.423(14)	0.5016(62)
0.005	$16^3\times32$	0.0947(12)	0.23519(91)	0.546(48)	$0.589(10)_4$
	$24^3\times32$	0.0983(16)	0.23278(53)	0.482(21)	0.6193(97)
0.006 ordered	$24^3\times32$	0.1191(14)	0.24368(28)	0.630(30)	0.756(12)
0.006 disordered	$24^3\times32$	0.2080(28)	0.21068(14)	1.047(93)	$1.151[13]_0$

Table 6.4: Meson masses at the bulk transition and the weak coupling side of the transition with twelve flavors.

m_q	Size	m_σ	m_{b_1}	m_{ρ_2}	m_{a_1}
0.003	$24^3\times32$	0.3429(37)	0.586(38)	0.4374(53)	0.566(18)
	$32^3\times32$	0.3418(25)	0.703[66]	0.4346(43)	0.585(11)
0.004	$24^3\times32$	0.3945(43)	0.749(72)	0.5203(80)	0.638(27)
0.005	$16^3\times32$	0.436(15)	$0.77[12]_4$	0.600(26)	0.96(10)
	$24^3\times32$	0.4811(99)	0.72(17)	0.626(14)	0.847(83)
0.006 ordered	$24^3\times32$	0.565(16)	1.33(34)	0.758[19]	0.995[94]
0.006 disordered	$24^3\times32$	0.882(97)	$2.36[58]_0$	1.244[66]	1.61[51]

Table 6.5: Continuation of table 6.4.

coupling side of the bulk transition at $\beta = 0.46$ once again confirms our previous findings 4.26, that there is no degeneracy in the masses of ρ and a_1. Linear fits are performed in figure 6.12.

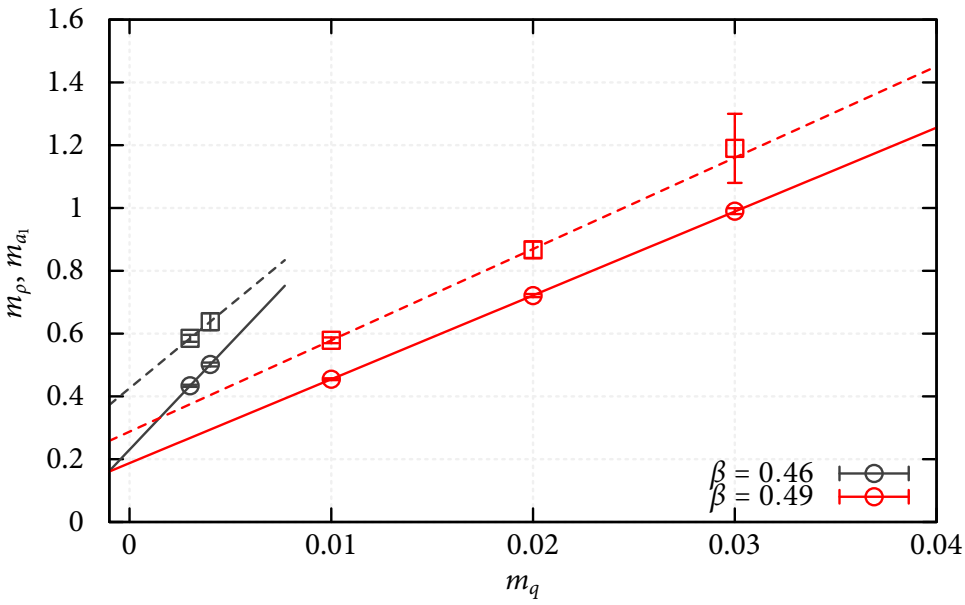

Figure 6.12: Masses of ρ and a_1 measured at the weak coupling side of the bulk transition at $\beta = 0.46$ and $\beta = 0.49$. No degeneracy is observed from both ensembles.

Part III

Conclusions

Chapter 7

Conclusions from the Lattice Simulations

Since the acceptance of Yang-Mills theory as a description of nature, the running coupling constant of non-abelian gauge theories has been a very exciting topic. The spontaneously broken chiral symmetry and the existence of light pions is the most interesting low energy behavior of QCD and is not amenable to analytic calculations. Although the prediction of infrared conformal behavior and walking coupling constants has existed for years, it remains hard for theorists to quantify the behavior of asymptotically free non-abelian gauge theories with many flavors of fermions at low energies. It has became particularly problematic to model builders, who want to exploit this interesting behavior of non-abelian gauge theories, especially for technicolor models. In QCD, theorists have guidance from experimental results, to help in computing the low energy behavior of the system from first principles, either by using lattice techniques or other methods. However, one loses this advantage when tackling theories different from QCD. This thesis is trying to understand the low energy phases of theories that are related to QCD through the replacement of the common quarks with eight or twelve degenerate quark flavors. With normal QCD in the standard model as a reference, the evidence collected in this

thesis for both eight and twelve flavors is consistent with a theory with spontaneously broken chiral symmetry.

All the evidence presented here suggests that systems consisting of eight and twelve flavors of fundamental fermions in an SU(3) gauge theory have the same qualitative properties. Both systems have a zero-temperature, lattice artifact bulk transition with naive staggered fermions and the Wilson plaquette gauge action. Both systems show a cross-over region with the DBW2 gauge action for an input fermion mass range $m_q \gtrsim 0.008$, when simulated on the lattice at zero temperature. This cross-over region separates the strongly coupled and the weakly coupled lattice theories. With twelve flavors, this cross-over region changes to a first order bulk transition at small quark masses $m_q \lesssim 0.008$ with the DBW2 gauge action. There could also be a bulk transition for eight flavors, at very small quark masses, but we have no numerical evidence for that to date. The hadronic observables measured on the configurations with DBW2 gauge action suggest that the lattice scale changes by about a factor of four for eight flavors across this cross over region, while for twelve flavors the scale changes about a factor of ten.

As a consequence of the rapid cross-over and the bulk transition, in the weakly coupled region of twelve flavors, hadronic scales such as $\langle\bar{\psi}\psi\rangle$ and σ almost vanish in the chiral limit with linear extrapolations. Nonetheless, the quark mass dependence of pions for both eight and twelve flavors at zero temperature show clear Goldstone behavior, $m_\pi^2 \propto m_q$, which disappears at finite temperatures. Therefore, from the lattice simulations performed and studied in this thesis work, the conclusion is that the chiral symmetry in the SU(3) gauge theories with eight or twelve fundamental fermions is spontaneously broken.

The behavior of the Goldstone pion is striking in that the dimensional coefficient B

(from $m_\pi^2 = 2Bm_q$) is barely changed in lattice units for different numbers of fermion flavors and different values of the lattice coupling constant. The value of B in lattice units also increases around 10% from the strong coupling to the weak coupling across the cross-over region, while all other hadronic scales decreases rapidly. Currently we do not have any understanding of the physics behind this behavior.

In our data, there is mild finite volume effect with eight flavors, indicating our volumes are sufficiently large. Studies with multiple volumes with eight flavors show that the finite volume effect is comparable to the statistical uncertainties. With twelve flavors in the weakly coupled region, the finite volume effect is more severe at $\beta = 0.50$, because the hadronic scales are smaller compared to the system with eight flavors. However, our simulations of multiple volumes for $\beta = 0.49$ shows that the results from this coupling is reliable.

The staggered fermion flavor (taste) symmetry breaking for the pions is quite interesting with eight and twelve flavors. It does not follow the common behavior observed by other QCD calculations with 2 or 2+1 flavors. Such behavior is also observed in [75]. We also note that staggered fermion chiral perturbation theory suggests that the mass splittings for the various pions will depend on the number of flavors [76]. We are not aware of other studies on the dependence of the flavor symmetry breaking on number of fermion flavors. In addition to the explicit N_f dependence suggested by chiral perturbation theory, it is also possible that the low energy constants associated with the flavor symmetry breaking depends on the number of fermions. More studies on this matter would certainly be very interesting.

It is important to point out that flavor symmetry breaking exists for the finite lattice spacings used in these simulations. However, the input number of fermion flavors

are correct in the lattice simulations, although they are not all equivalent to each other. One can estimate the differences between these quarks by examining the mass differences in the spectra of non-local pions, as depicted in figure 4.38. Given the condition of spontaneously broken chiral symmetry, $m_\pi^2 = 2Bm_q$, the broken flavor symmetry can be conceptually represented by the differences in quark masses. For the system with twelve flavors at $\beta = 0.49$, the differences in quark masses is about a factor of two at $m_q = 0.02$. When running toward low energies, although quarks with larger masses decouple before quarks with smaller masses, the mass difference shown here in twelve-flavor system is not large and likely does not alter the running of coupling significantly. This situation would be worse for zero input quark masses, where Schrodinger functional methods (discussed in the next chapter 8) have been used and an infrared fixed point was claimed to be found.

We have confirmd that the bulk transition seen in earlier work is a lattice artifact transition, since it goes away (or at least moves to much smaller quark masses) when we change from the Wilson to DBW2 gauge action. In the input quark mass range used in these simulations, only a cross over is observed. This is likely due to the smoothing of the gauge fields that is done by the DBW2 gauge action, for a fixed physical scale. Thus, the size of the lattice spacing dependent higher dimensional operators, which do not contribute in the continuum, is reduced in the DBW2 gauge action. Nevertheless, such a bulk transition could still exist for much smaller quark masses with the DBW2 gauge action, as seen in the simulations with twelve flavors. The DBW2 gauge action might only reduce the size of the mass dependent lattice artifact operators that are irrelevant in the continuum.

We find compelling evidence of the existence of finite temperature, thermal transi-

tions with both eight and twelve flavors. For eight flavors, a first order finite temperature transition is observed at $\beta = 0.54$. This transition restores the chiral symmetry as the temperature raises. With twelve flavors, establishing the order of the finite temperature transition is too difficult for current computers. As the zero-temperature value of $\langle\bar{\psi}\psi\rangle$ is really small at the chiral limit, the fluctuations in the finite temperature simulations would cover any trace of this first order transition, unless prohibitively large spatial lattice volumes and small quark masses are used. However, we can study the finite temperature phase transition with other variables. At high temperatures, we do see a screening mass for the pion and the emergence of non-zero Wilson loops in the temporal direction with twelve flavors. This is the same behavior as with eight flavors. Compared to the hadronic values at zero temperature, the finite temperature hadronic values strongly suggests a finite temperature phase transition has taken place with 12 flavors, as it is the case with eight flavors. This implies that the zero temperature phase can not be conformal for either eight or twelve flavors.

Chapter 8

Comparison with Other Recent Lattice Studies

There are several groups studying the same many flavor QCD systems simulated here concurrent with this thesis work. The consensus on eight-flavor QCD is that the vacuum indeed spontaneously breaks chiral symmetry. However, there are conflicting reports on systems with twelve degenerate fermion flavors.

The results of this thesis work directly contradict earlier studies with Schrodinger functional methods [77, 78], which claim the existence of an infrared fixed point with twelve flavors, or even with ten flavors [79]. This is certainly very puzzling and needs continuing effort of the community to clear it up. However, it is possible that certain lattice operators might be the culprit. The bulk transition seen here for twelve flavors for small input quark masses can be very strong when the quark mass approaches zero, which indicates certain lattice operators, which are irrelevant in the continuum, do become relevant and significant on the lattice with strong coupling. These operators may then alter the running of the coupling constant, as the continuum limit is approached,

until one is very close to $a = 0$. This is one mechanism through which a nearby, lattice-artifact phase transition could alter the running of the coupling constant, as measured by the Schrodinger functional. The non-linearity in quark mass, for fixed coupling, we see in the hadronic observables is partially caused by the bulk transition or cross over. Schrodinger functional studies with zero quark mass, which are not sensitive to lattice artifact transitions, could be markedly influenced by them. It would be worthwhile to find a way to quantify the effect of such lattice operators.

With a similar hadronic scale but a different action, another lattice group [80, 75, 81, 82] has also studied a few hadronic observables and has come to the same conclusion as this thesis, that the hadronic observables on the lattice with twelve flavors show the behavior of chiral symmetry breaking. However, another group [83, 84, 85, 86] claims the opposite. The author of this thesis would like to express his understanding of the situation in the following.

1. The "backward flow" shown in [83, 86] represented by the ratio of m_π/m_ρ is misleading and inconclusive. In this thesis, a similar behavior is discussed in 4.8 explained with m_π/f_π in figure 4.40. For large quark masses, the line of constant physics depicted by the ratio of m_π/f_π would go "backwards" not only in the weak coupling region with twelve flavors but also with eight flavors (see figure 4.39. Only when one goes to really small quark masses, can one observes the true behavior, which is already shown for eight flavors, but would require much lighter masses for twelve flavors.

2. Two discontinuity observed in [84] is certainly interesting. However, further studies with hadronic observables are needed to justify the true physics of the transition.

There are other studies on this matter. One uses Monte Carlo renormalization group technique [87], and the other uses Twisted Polyakov loop scheme [88]. However, the numerical complications in their studies have not been fully resolved and the conclusions are unclear.

Recently, a second analysis [89] on the reported data [82] has been posted. To the contrary of the original authors of [82], the authors of the new analysis [89] came to the conclusion that the theory with twelve flavors is consistent with the conformal prescription. However, how to explain the finite temperature behavior of the system is unclear. More work must to be done to understand the full implication of an infrared conformal theory on the lattice, and to fully digest the conflicts between the results of this thesis and their claim.

There is an interesting study [90] of GMOR-like relation in infrared conformal gauge theories, recently. Whether the data in this thesis can be described by this GMOR-like relation is under investigation.

Chapter 9

Outlook

The main conclusion of this thesis is that the behavior of theories with eight or twelve fermion flavors in the fundamental representation of an SU(3) gauge group is consistent with spontaneously broken chiral symmetry. However, the complete exclusion of an infrared conformal phase is not possible. The phenomenology of walking or infrared conformal theory with nonzero fermion masses is currently still in its infancy. More analytic and lattice calculations are needed to explore the nature of such kind of theory near or in the infrared conformal phase [91, 90].

On the lattice, it is important to make sure the systematic errors associated with finite size effect or effects from lattice artifact bulk transition are under control. One needs to go to smaller quark masses and larger lattice volumes than have been used recently. A deeper understanding of the zero-temperature bulk transition is needed to quantify the effect of the bulk transition on lattice simulations.

The behavior of the system with spontaneously broken chiral symmetry should be quite different than the system with infrared conformal symmetry. However, with current simulations, both interpretation might be applied with certain numerical uncer-

tainty. In the case of the ensemble generated and analyzed in [82], a different interpretation [89] has been proposed. Apart from the lack of understanding of finite temperature behavior with an existing infrared fixed point, to differentiate these two proposed scenarios, one needs much more statistics and a better understanding of both the theory with spontaneously broken chiral symmetry and the theory with infrared conformal symmetry.

Another task would be to establish a well-behaved scaling relation on the lattice, and to ascertain that the lattice simulations are close to the continuum limit. Although the continuum limit is known to exist at $\beta \to \infty$ for theories with confinement, the existence of an infrared fixed point could change the way lattice simulations approaches to the continuum. This is important and needs to be addressed carefully.

Part IV

Bibliography

Bibliography

[1] M. Cheng *et al.*, *Flavor symmetry breaking and scaling for improved staggered actions in quenched QCD*, Eur. Phys. J. **C51** (2007) 875–881 [arXiv:hep-lat/0612030].

[2] **MILC** Collaboration, K. Orginos and D. Toussaint, *Testing improved actions for dynamical Kogut-Susskind quarks*, Phys. Rev. **D59** (1999) 014501 [arXiv:hep-lat/9805009].

[3] **MILC** Collaboration, K. Orginos, D. Toussaint and R. L. Sugar, *Variants of fattening and flavor symmetry restoration*, Phys. Rev. **D60** (1999) 054503 [arXiv:hep-lat/9903032].

[4] C.-N. Yang and R. L. Mills, *Conservation of Isotopic Spin and Isotopic Gauge Invariance*, Phys.Rev. **96** (1954) 191–195.

[5] S. L. Adler, *Axial vector vertex in spinor electrodynamics*, Phys.Rev. **177** (1969) 2426–2438.

[6] J. Bell and R. Jackiw, *A PCAC puzzle: $\pi^0 \to \gamma\gamma$ in the σ-model*, Nuovo Cim. **A60** (1969) 47–61.

[7] M. Gell-Mann, R. Oakes and B. Renner, *Behavior of current divergences under SU(3) x SU(3)*, Phys.Rev. **175** (1968) 2195–2199.

[8] H. Leutwyler, *On the foundations of chiral perturbation theory*, Ann. Phys. **235** (1994) 165–203 [arXiv:hep-ph/9311274].

[9] J. Gasser and H. Leutwyler, *Chiral Perturbation Theory to One Loop*, Ann. Phys. **158** (1984) 142.

[10] J. Gasser and H. Leutwyler, *Chiral Perturbation Theory: Expansions in the Mass of the Strange Quark*, Nucl. Phys. **B250** (1985) 465.

[11] J. Gasser and H. Leutwyler, *Light Quarks at Low Temperatures*, Phys. Lett. **B184** (1987) 83.

[12] D. Gross and F. Wilczek, *Asymptotically Free Gauge Theories. 1*, Phys.Rev. **D8** (1973) 3633–3652.

[13] D. Gross and F. Wilczek, *Ultraviolet Behavior of Nonabelian Gauge Theories*, Phys.Rev.Lett. **30** (1973) 1343–1346.

[14] H. Politzer, *Asymptotic Freedom: An Approach to Strong Interactions*, Phys.Rept. **14** (1974) 129–180.

[15] H. Politzer, *Reliable Perturbative Results for Strong Interactions?*, Phys.Rev.Lett. **30** (1973) 1346–1349.

[16] W. E. Caswell, *Asymptotic Behavior of Nonabelian Gauge Theories to Two Loop Order*, Phys. Rev. Lett. **33** (1974) 244.

[17] T. Banks and A. Zaks, *On the Phase Structure of Vector-Like Gauge Theories with Massless Fermions*, Nucl. Phys. **B196** (1982) 189.

[18] P. Higgs, *Prehistory of the Higgs boson*, Comptes Rendus Physique **8** (2007) 970–972.

[19] S. Weinberg, *Implications of Dynamical Symmetry Breaking*, Phys.Rev. **D13** (1976) 974–996.

[20] L. Susskind, *Dynamics of Spontaneous Symmetry Breaking in the Weinberg-Salam Theory*, Phys.Rev. **D20** (1979) 2619–2625.

[21] S. Weinberg, *Implications of Dynamical Symmetry Breaking: An Addendum*, Phys.Rev. **D19** (1979) 1277–1280. (For original paper see Phys.Rev.D13:974-996,1976).

[22] K. D. Lane, *An Introduction to technicolor*, `arXiv:hep-ph/9401324 [hep-ph]`.

[23] R. Chivukula, *Lectures on technicolor and compositeness*, `arXiv:hep-ph/0011264 [hep-ph]`.

[24] E. Eichten and K. D. Lane, *Dynamical Breaking of Weak Interaction Symmetries*, Phys.Lett. **B90** (1980) 125–130.

[25] S. Dimopoulos and L. Susskind, *Mass Without Scalars*, Nucl.Phys. **B155** (1979) 237–252.

[26] T. W. Appelquist, D. Karabali and L. Wijewardhana, *Chiral Hierarchies and the Flavor Changing Neutral Current Problem in Technicolor*, Phys.Rev.Lett. **57** (1986) 957.

[27] T. Appelquist and L. Wijewardhana, *Chiral Hierarchies from Slowly Running Couplings in Technicolor Theories*, Phys.Rev. **D36** (1987) 568.

[28] M. A. Luty and T. Okui, *Conformal technicolor*, JHEP **0609** (2006) 070 [arXiv:hep-ph/0409274 [hep-ph]].

[29] J. Smit, *Introduction to quantum fields on a lattice: 'a robust mate'*, vol. 15. Cambridge University Press, 2002.

[30] H. Rothe, *Lattice gauge theories: an introduction*. World Scientific lecture notes in physics. World Scientific, 2005.

[31] T. DeGrand and C. DeTar, *Lattice methods for quantum chromodynamics*. World Scientific Publishing Co. Pte. Ltd., 2006.

[32] C. Gattringer and C. B. Lang, *Quantum chromodynamics on the lattice: an introductory presentation*. Springer–Verlag, 2009.

[33] J. B. Kogut and L. Susskind, *Hamiltonian Formulation of Wilson's Lattice Gauge Theories*, Phys.Rev. **D11** (1975) 395.

[34] L. Susskind, *Lattice Fermions*, Phys.Rev. **D16** (1977) 3031–3039.

[35] H. Kluberg-Stern, A. Morel, O. Napoly and B. Petersson, *Flavors of Lagrangian Susskind Fermions*, Nucl.Phys. **B220** (1983) 447.

[36] K. Wilson, *New phenomena in subnuclear physics*, by A. Zichichi (1977).

[37] D. B. Kaplan, *A Method for simulating chiral fermions on the lattice*, Phys.Lett. **B288** (1992) 342–347 [arXiv:hep-lat/9206013 [hep-lat]].

[38] Y. Shamir, *Chiral fermions from lattice boundaries*, Nucl.Phys. **B406** (1993) 90–106 [arXiv:hep-lat/9303005 [hep-lat]].

[39] H. Neuberger, *Exactly massless quarks on the lattice*, Phys.Lett. **B417** (1998) 141–144 [arXiv:hep-lat/9707022 [hep-lat]].

[40] K. G. Wilson, *Confinement of Quarks*, Phys.Rev. **D10** (1974) 2445–2459.

[41] T. Takaishi, *Heavy quark potential and effective actions on blocked configurations*, Phys.Rev. **D54** (1996) 1050–1053.

[42] **QCD-TARO Collaboration** Collaboration, P. de Forcrand *et al.*, *Renormalization group flow of SU(3) lattice gauge theory: Numerical studies in a two coupling space*, Nucl.Phys. **B577** (2000) 263–278 [arXiv:hep-lat/9911033 [hep-lat]].

[43] Y. Aoki, T. Blum, N. Christ, C. Dawson, K. Hashimoto *et al.*, *Lattice QCD with two dynamical flavors of domain wall fermions*, Phys.Rev. **D72** (2005) 114505 [arXiv:hep-lat/0411006 [hep-lat]].

[44] A. Kennedy, *Algorithms for dynamical fermions*, arXiv:hep-lat/0607038 [hep-lat].

[45] S. Duane, A. Kennedy, B. Pendleton and D. Roweth, *Hybrid Monte Carlo*, Phys.Lett. **B195** (1987) 216–222.

[46] D. Weingarten and D. Petcher, *Monte Carlo Integration for Lattice Gauge Theories with Fermions*, Phys.Lett. **B99** (1981) 333.

[47] R. Scalettar, D. Scalapino and R. Sugar, *NEW ALGORITHM FOR THE NUMERICAL SIMULATION OF FERMIONS*, Phys.Rev. **B34** (1986) 7911–7917.

[48] S. A. Gottlieb, W. Liu, D. Toussaint, R. Renken and R. Sugar, *Hybrid Molecular Dynamics Algorithms for the Numerical Simulation of Quantum Chromodynamics*, Phys.Rev. **D35** (1987) 2531–2542.

[49] N. Metropolis, A. Rosenbluth, M. Rosenbluth, A. Teller, E. Teller *et al.*, *Equation of state calculations by fast computing machines*, The journal of chemical physics **21** (1953), no. 6 1087.

[50] J. Sexton and D. Weingarten, *Hamiltonian evolution for the hybrid Monte Carlo algorithm*, Nucl.Phys. **B380** (1992) 665–678.

[51] I. P. Omelyan, I. M. Mryglod and R. Folk, *Symplectic analytically integrable decomposition algorithms: classification, derivation, and application to molecular dynamics, quantum and celestial mechanics simulations*, Computer Physics Communications **151** (2003), no. 3 272 – 314.

[52] A. Kennedy, M. Clark and P. Silva, *Force Gradient Integrators*, PoS **LAT2009** (2009) 021 [arXiv:0910.2950 [hep-lat]].

[53] H. Yin and R. D. Mawhinney, "Force gradient integrator." in preparation, 2011.

[54] M. Hestenes and E. Stiefel, *Methods of conjugate gradients for solving linear systems*, Journal of Research of the National Bureau of Standards **49** (1952), no. 6.

[55] A. D. Kennedy, I. Horvath and S. Sint, *A new exact method for dynamical fermion computations with non-local actions*, Nucl. Phys. Proc. Suppl. **73** (1999) 834–836 [arXiv:hep-lat/9809092].

[56] M. A. Clark and A. D. Kennedy, *The RHMC algorithm for 2 flavors of dynamical staggered fermions*, Nucl. Phys. Proc. Suppl. **129** (2004) 850–852 [arXiv:hep-lat/0309084].

[57] M. A. Clark, A. D. Kennedy and Z. Sroczynski, *Exact 2+1 flavour RHMC simulations*, Nucl. Phys. Proc. Suppl. **140** (2005) 835–837 [arXiv:hep-lat/0409133].

[58] B. Jegerlehner, *Krylov space solvers for shifted linear systems*, arXiv:hep-lat/9612014.

[59] M. A. Clark and A. D. Kennedy, *Accelerating dynamical fermion computations using the rational hybrid Monte Carlo (RHMC) algorithm with multiple pseudofermion fields*, Phys. Rev. Lett. **98** (2007) 051601 [arXiv:hep-lat/0608015].

[60] M. Hasenbusch and K. Jansen, *Speeding up lattice QCD simulations with clover-improved Wilson fermions*, Nucl. Phys. **B659** (2003) 299–320 [arXiv:hep-lat/0211042].

[61] C. Urbach, K. Jansen, A. Shindler and U. Wenger, *HMC algorithm with multiple time scale integration and mass preconditioning*, Comput. Phys. Commun. **174** (2006) 87–98 [arXiv:hep-lat/0506011].

[62] M. F. Golterman, *STAGGERED MESONS*, Nucl.Phys. **B273** (1986) 663.

[63] G. Kilcup and S. R. Sharpe, *A TOOL KIT FOR STAGGERED FERMIONS*, Nucl.Phys. **B283** (1987) 493.

[64] C. W. Bernard, T. Burch, K. Orginos, D. Toussaint, T. A. DeGrand *et al.*, *The Static quark potential in three flavor QCD*, Phys.Rev. **D62** (2000) 034503 [arXiv:hep-lat/0002028 [hep-lat]].

[65] M. Li, *The static quark potential for dynamical domain wall fermion simulations*, PoS **LAT2006** (2006) 183 [arXiv:hep-lat/0610106].

[66] R. Sommer, *A New way to set the energy scale in lattice gauge theories and its applications to the static force and alpha-s in SU(2) Yang-Mills theory*, Nucl. Phys. **B411** (1994) 839–854 [arXiv:hep-lat/9310022].

[67] C.-Z. Sui, *Flavor dependence of quantum chromodynamics*, . UMI-99-98219.

[68] X.-Y. Jin and R. D. Mawhinney, *Lattice QCD with Eight Degenerate Quark Flavors*, PoS **LATTICE2008** (2008) 059 [arXiv:0812.0413 [hep-lat]].

[69] X.-Y. Jin and R. D. Mawhinney, *Lattice QCD with 8 and 12 degenerate quark flavors*, PoS **LAT2009** (2009) 049 [arXiv:0910.3216 [hep-lat]].

[70] X.-Y. Jin and R. D. Mawhinney, *Evidence for a First Order, Finite Temperature Phase Transition in 8 Flavor QCD*, PoS **LATTICE2010** (2010) 055 [arXiv:1011.1511 [hep-lat]].

[71] **RBC Collaboration, UKQCD Collaboration** Collaboration, Y. Aoki *et al.*, *Continuum Limit Physics from 2+1 Flavor Domain Wall QCD*, Phys.Rev. **D83** (2011) 074508 [arXiv:1011.0892 [hep-lat]].

[72] R. D. Mawhinney, *Review of unquenched results*, Nucl. Phys. Proc. Suppl. **83** (2000) 57–66 [arXiv:hep-lat/0001032].

[73] N. Ishizuka, M. Fukugita, H. Mino, M. Okawa and A. Ukawa, *Operator dependence of hadron masses for Kogut-Susskind quarks on the lattice*, Nucl. Phys. **B411** (1994) 875–902.

[74] F. R. Brown *et al.*, *Lattice QCD with eight light quark flavors*, Phys. Rev. **D46** (1992) 5655–5670 [arXiv:hep-lat/9206001].

[75] Z. Fodor, K. Holland, J. Kuti, D. Nogradi and C. Schroeder, *Nearly conformal gauge theories on the lattice*, Int.J.Mod.Phys. **A25** (2010) 5162–5174.

[76] S. R. Sharpe and R. S. Van de Water, *Unphysical operators in partially quenched QCD*, Phys.Rev. **D69** (2004) 054027 [arXiv:hep-lat/0310012 [hep-lat]].

[77] T. Appelquist, G. T. Fleming and E. T. Neil, *Lattice Study of the Conformal Window in QCD-like Theories*, Phys. Rev. Lett. **100** (2008) 171607 [arXiv:0712.0609 [hep-ph]].

[78] T. Appelquist, G. T. Fleming and E. T. Neil, *Lattice Study of Conformal Behavior in SU(3) Yang-Mills Theories*, Phys.Rev. **D79** (2009) 076010 [arXiv:0901.3766 [hep-ph]].

[79] M. Hayakawa, K.-I. Ishikawa, Y. Osaki, S. Takeda, S. Uno *et al.*, *Running coupling constant of ten-flavor QCD with the Schródinger functional method*, Phys.Rev. **D83** (2011) 074509 [arXiv:1011.2577 [hep-lat]].

[80] Z. Fodor, K. Holland, J. Kuti, D. Nogradi and C. Schroeder, *Nearly conformal gauge theories in finite volume*, Phys.Lett. **B681** (2009) 353–361 [arXiv:0907.4562 [hep-lat]].

[81] Z. Fodor, K. Holland, J. Kuti, D. Nogradi and C. Schroeder, *Chiral symmetry breaking in fundamental and sextet fermion representations of SU(3) color*, arXiv:1103.5998 [hep-lat].

[82] Z. Fodor, K. Holland, J. Kuti, D. Nogradi and C. Schroeder, *Twelve massless flavors and three colors below the conformal window*, arXiv:1104.3124 [hep-lat].

[83] A. Deuzeman, M. Lombardo and E. Pallante, *Evidence for a conformal phase in SU(N) gauge theories*, Phys.Rev. **D82** (2010) 074503 [arXiv:0904.4662 [hep-ph]].

[84] A. Deuzeman, E. Pallante and M. P. Lombardo, *The Bulk transition of many-flavour QCD and the search for a UVFP at strong coupling*, PoS **LATTICE2010** (2010) 067 [arXiv:1012.5971 [hep-lat]].

[85] A. Deuzeman, M. Lombardo and E. Pallante, *Chiral symmetry of QCD with twelve light flavors*, arXiv:1012.6023 [hep-lat].

[86] A. Deuzeman, E. Pallante and M. Lombardo, *Phases of QCD from small to large N(f): (Some) lattice results*, Int.J.Mod.Phys. **A25** (2010) 5175–5182.

[87] A. Hasenfratz, *Conformal or Walking? Monte Carlo renormalization group studies of SU(3) gauge models with fundamental fermions*, Phys.Rev. **D82** (2010) 014506 [arXiv:1004.1004 [hep-lat]].

[88] E. Itou, T. Aoyama, M. Kurachi, C.-J. Lin, H. Matsufuru *et al.*, *Search for the IR fixed point in the Twisted Polyakov Loop scheme (II)*, PoS **LATTICE2010** (2010) 054 [arXiv:1011.0516 [hep-lat]].

[89] T. Appelquist, G. T. Fleming, M. Lin, E. T. Neil and D. A. Schaich, *Lattice Simulations and Infrared Conformality*, arXiv:1106.2148 [hep-lat].

[90] A. Patella, *GMOR-like relation in IR-conformal gauge theories*, arXiv:1106.3494 [hep-th].

[91] L. Del Debbio and R. Zwicky, *Scaling relations for the entire spectrum in mass-deformed conformal gauge theories*, Phys.Lett. **B700** (2011) 217–220 [arXiv:1009.2894 [hep-ph]].

[92] B. Efron, *The jackknife, the bootstrap and other resampling plans*. CBMS-NSF regional conference series in applied mathematics. Society for Industrial and Applied Mathematics, 1994.

Part V

Appendices

Appendix A

Jackknife and Super-Jackknife

For data directly measured on the lattice, such as a propagator, one first averages them in groups of consecutive configurations, commonly called blocking. This is done to remove correlations. Let's name the set of data after blocking $\{x_i \,|\, i = 1, \cdots, n\}$, and x_i is a set of blocked data that is the average of the original data measured on the small groups of consecutive lattice configurations. Considering an observable defined on the data directly measured on the lattice with a function form of $\mathcal{O} = f(x)$, the estimation of the expected value of the observable is

$$\mathcal{O} = f\left(\frac{1}{n}\sum_i x_i\right). \tag{A.1}$$

The function f can be anything, even a complicated fitting procedure.

A.1 Jackknife

Jackknife method is used to estimate the error of the observable. Define jackknife blocks as follows,

$$x_i^j = \frac{1}{n-1}\left(\sum_k x_k - x_i\right) . \tag{A.2}$$

Define the jackknife average as

$$\mathcal{O}^j = \frac{1}{n}\sum_i f(x_i^j) . \tag{A.3}$$

The jackknife estimation of the error is given by

$$(\sigma^j)^2 = \frac{n-1}{n}\sum_i \left(f(x_i^j, y_i^j) - \mathcal{O}^j\right)^2 . \tag{A.4}$$

Introduce the **Quenouille's bias estimate** [92].

$$\text{BIAS}\left(\mathcal{O}\right) \equiv \mathcal{O} - \tilde{\mathcal{O}} = \left(n-1\right)\left(\mathcal{O}^j - \mathcal{O}\right) , \tag{A.5}$$

where $\tilde{\mathcal{O}}$ is the bias-corrected jackknife estimate of the expected value of the observable. Usually in the lattice calculations, and in this thesis work, the bias is one or two order of magnitude smaller than the estimated error, so $\mathcal{O}$ can be simply quoted as the result and neglect the bias.

A.2 Super-Jackknife

Super-jackknife is used for sets of data from two or more different ensembles. Considering two sets of data from two different ensembles, $\{x_i \,|\, i = 1, \cdots, n_x\}$ and $\{y_i \,|\, i = 1, \cdots, n_y\}$.

The super-jackknife blocks for x are defined as

$$x_1^j x_2^j \cdots x_{n_x}^j \underbrace{x \cdots x}_{n_y} . \tag{A.6}$$

The super-Jackknife blocks for y are defined as

$$\underbrace{y \cdots y}_{n_x} y_1^j y_2^j \cdots y_{n_y}^j \tag{A.7}$$

Thus, there are $n_x + n_y$ jackknife blocks totally. One then use this exactly as in the case of one set of data. Define the super-Jackknife average,

$$\mathcal{O}^j = \frac{1}{n_x + n_y} \left(\sum_i f(x_i^j, y) + \sum_i f(x, y_i^j) \right) \tag{A.8}$$

The standard error from super-jackknife can be written as

$$(\sigma^j)^2 = \frac{n_x + n_y - 1}{n_x + n_y} \left(\sum_i \left(f(x_i^j, y) - \mathcal{O}^j \right)^2 + \sum_i \left(f(x, y_i^j) - \mathcal{O}^j \right)^2 \right) \tag{A.9}$$

There is an ambiguity in x and y used in construct the super-jackknife blocks. When x or y is already an estimated value, which means $x \neq x^j \equiv \frac{1}{n} \sum_i x_i^j$, one may either use x or x^j or even the bias corrected estimator in the super-jackknife blocks. However, in practice, these different choices barely make any difference. In this thesis work, the value obtained by equation (A.1) is used.